ABSTRACT

Title of Dissertation:	MORPHOLOGICAL CHARACTERIZATION OF QUASI-CIRCULAR FEATURES ACROSS THE SOLAR SYSTEM
	Karla Abigail Nunez, Doctor of Philosophy, 2025
Dissertation directed by:	Professor, Laurent G. J. Montési, and Department of Geology

The interior dynamics and geologic activity of a planetary body are linked. Due to instrumentation limitations, probing or studying the interior of planetary bodies directly is difficult. I argue that by studying surface features whose formation mechanism is linked to the material exchange between the interior and crust, I can gain information on the evolution and dynamics of the planetary body. For this dissertation, I have chosen to study microfeatures on Europa, coronae on Venus, and calderas on Earth.

New methods were developed to determine the orientation and circularity of surface features across three planetary bodies. Three circular statistical tests were conducted to test the distribution of the orientation data for the quasi-circular features. A new definition of misorientation based on spherical geometry was defined for the Venus and Earth studies.

On Europa, the orientation of microfeatures is not uniformly distributed and does not depend on latitude. Microfeatures are found to have formed episodically and under various stresses. Chaos and hybrids have a more extended formation period than pits and domes. These findings support formation mechanisms dependent on a diapir or liquid water body interacting with crustal horizontal stresses.

A new digital map of 525 coronae was created for Venus. Orientation results show that coronae have a non-uniform orientation distribution. Their orientation is not dependent on size, formation location, or circularity. Comparing the orientation of coronae to implied stress orientations shows that coronae are likely to be elongated in the direction of maximum horizontal compressional stress. These results align with coronae formation models that show a preferential injection of melt in the direction of maximum horizontal compressional stress or a rising plume that pools along a step in lithospheric thickness.

I compared the orientation of calderas on Earth to direct stress measurements. These findings show that calderas are more likely to be elongated perpendicular to the direction of maximum horizontal compressional stress. These results suggest that local stresses and preexisting structures influence calderas' orientation. I advocate for caldera formation models based on the deformation of magma chambers or the preferential injection of magma along preexisting fault structures.

MORPHOLOGICAL CHARACTERIZATION OF QUASI-CIRCULAR FEATURES ACROSS THE SOLAR SYSTEM

by

Karla Abigail Nunez

Dissertation submitted to the Faculty of the Graduate School of the
University of Maryland, College Park, in partial fulfillment
of the requirements for the degree of
Doctor of Philosophy
2025

Advisory Committee:
Professor Laurent G. J. Montési, Chair
Assistant Professor Megan E. Newcombe
Professor Vedran Lekic
Dr. Emily Martin
Professor Efrain Rodriguez (Dean's Representative)

© Copyright by
Karla Abigail Nunez
2025

Dedication

To my fellow DACA recipients and undocumented immigrants. I fought so hard to break the ceiling

Acknowledgements

Before starting this program, I was told by one person that this would be the hardest thing I'd ever do. Dr. Jeffery Dunham, you weren't wrong, and I thank you for your honesty all those years ago. I thank my lab group, James Bader, Joe Schools, Zachary Zega, Sourabh Shubham, Edward Williams, Megan Perry, and Megan Ryan, for making space for me to rant, cry, and play board games. I thank my various teammates (Kyle Kim, Jacob Giles, the economics and geography departments) in intramural volleyball and soccer; those games were the highlights of some of my toughest weeks. I want to thank the wonderful community I made while living in Pilot House: Andrew Piper, Tessa Piper, Jacob Lusk, Dakota Dutko, Anastasia Zagoruichyk, Igor Marques Van Der Put, and Tanya Tytko. Y'all have forever changed the way I think of trivia. I also thank the groups Geolatinas and SACNAS for reminding me daily that I belong in academia and that my Latinidad is a strength, not a hindrance.

I would not be the scientist I am today without the mentors I gained along my academic journey. Thank you, Dr. Eilat Glikman, Dr. Emily Martin, Dr. Lynnae Quick, and Dr. Laurent Montesi. Thank you for your wisdom and patience.

I thank my two families: The Nunezs and the Feldmans. I thank my parents, Digna and Carlos, for their sacrifices and love. You have shaped me, and I hope I have made you proud.

Lastly, I thank the two most important people in my life: my husband, Isaac Feldman, and my dog, Dr. Kharisma Md, Ph.D. Thank you for your love.

Table of Contents

Dedication ii
Acknowledgements iii
Table of Contents iv
List of Tables vi
List of Figures vii
List of Abbreviations ix
Chapter 1. Introduction: Planetary Interior Dynamics Across our Solar System 1
1.1 Introduction 1
1.2 Europa 2
1.3 Venus 6
1.4 Earth 10
Chapter 2. Orientation of Microfeatures on Europa 13
2.1 Abstract 13
2.2 Introduction 14
2.3 Methods 19
2.3.1 Microfeature database 19
2.3.2 Microfeature orientation 22
2.4 Circular statistics 25
2.4.1 Mean Direction 25
2.4.2 Circular variance and uncertainty 26
2.4.3 Pearson $\chi 2$ test 27
2.4.4 Rayleigh Test 28
2.4.5 Modified Kuiper Test 28
2.5 Results 29
2.5.1 Size and elongation 36
2.5.2 Microfeature orientation 38
2.5.3 Distribution of microfeature type 38
2.5.4 Statistical Test by Region 43
2.5.5 Statistical Results by Feature Type 45
2.5.6 Chaos 46
2.5.7 Pits 47
2.5.8 Domes 48
2.5.9 Hybrids 52
2.5.10 Spots 53
2.5.11 Craters 54
2.5.12 The effect of nearly circular features 55
2.5.13 Orientation by Latitude 59
2.6 Discussion 61
2.6.1 Origin of elongation 61
2.6.2 Existence of preferred orientations 64
2.6.3 Formation episodes 65
2.7 Conclusions 68
Chapter 3. Coronae Elongation in Relation to Chasmata on Venus 70
3.1 Abstract 70

3.2 Introduction 71
3.3 Methods 75
3.3.1 Mapping Coronae and Rifts 75
3.3.2 Misorientation 79
3.3.3 Calculating Circular Weighted Averages 81
3.4 Results 87
3.4.1 Corona Elongation and Orientation 87
3.4.2 Rift Orientations 95
3.4.3 Misorientation Between Rifts and Coronae 99
3.5 Discussion 108
3.6 Conclusion 113
Chapter 4. Calderas As Markers for Determining Magma Chamber Geometry 116
4.1 Abstract 116
4.2 Intro 116
4.3 Methods 118
4.3.1 Calderas and Stress Measurements 118
4.3.2 Circular Statistics 120
4.4 Results 122
4.4.1 Caldera Orientation and Circularity 122
4.4.2 Misorientation 130
4.5 Discussion 132
4.5.1 Middle American Trench 134
4.5.2 Chile-Peru Trench 136
4.5.3 Sunda Subduction Zone 138
4.6 Conclusion 140
Chapter 5. Conclusion & Future Work 142
5.1 Conclusions 142
5.1.1 Europa 142
5.1.2 Venus 142
5.1.3 Earth 143
5.2 Future Work 144
5.2.1 Expansion to Venus Research 144
5.2.2 Expansion to Earth Research 145
Bibliography 147

List of Tables

Table 2-1: Orientation statistics for all mapped microfeatures 32
Table 3-1: Mapping scale for various corona diameters 76
Table 3-2: Summary of the morphological characteristics of all 523 mapped coronae. 93
Table 4-1: Characteristics of the 57 mapped calderas, ordered by decreasing circularity 125

List of Figures

Figure 1-1: Hypothetical cross-section of Europa. 2
Figure 1-2: Different types of microchaos on Europa. 4
Figure 1-3: Formation model of microchaos on Europa..... 5
Figure 1-4: Magellan Radar image of Aine Corona 7
Figure 1-5: 3D models of a diapir rising through the mantle and initiating subduction as it interacts with the lithosphere..... 8
Figure 1-6: Billy Mitchell is a 2 km wide caldera located in Papua New Guinea..... 10
Figure 1-7: Four different styles of subsidence that cause the formation of Calderas 11
Figure 2-1: Example of microfeatures on Europa 14
Figure 2-2: Outlines of the four regions mapped by Noviello et al., (2019a, b) and the names of the mosaics on which these maps are based..... 19
Figure 2-3: Breakdown of the minimum bounding geometry tool in ArcGIS 22
Figure 2-4: Location of all mapped microfeatures, color-coded according to orientation 31
Figure 2-5: Probability Density Function of microfeature area and circularity 36
Figure 2-6: Rose diagrams illustrate the orientation of all microfeatures in each of the four regions mapped by Noviello et al. (2019a) 40
Figure 2-7: Rose diagram of microfeature orientation in the NLH separated by microfeature category 49
Figure 2-8: Rose diagram of microfeature orientation in the NTH separated by microfeature category 50
Figure 2-9: Rose diagram of microfeature orientation in the SLH separated by microfeature category. 51
Figure 2-10: Rose diagram of microfeature orientation in the STH separated by microfeature category 52
Figure 2-11: Rose Diagrams of microfeatures with elongation values less than 0.6. 55
Figure 2-12: Histograms of the orientation of features in (a) NTH, (b) STH, (c) NLH, and (d) SLH..... 59
Figure 2-13: Potential origins of microfeature elongation..... 63
Figure 3-1: Unnamed coronae south of Epona Coronae in Alta Regio 75
Figure 3-2: Calculation of the misorientation on a sphere. 81
Figure 3-3: Fisher-based weighing functions presented against distance on Venus for various values of the concentration parameter κ 84
Figure 3-4: Global map of coronae located between 90°N and 90°S on Venus 86
Figure 3-5: Morphological characteristics of coronae 88
Figure 3-6: Rose diagrams comparing the orientation distributions of all mapped coronae and coronae with below-average circularity 91
Figure 3-7: Chasmata lineament orientation..... 94
Figure 3-8: Map of rift misorientation 98
Figure 3-9: Rose diagrams showing misorientation for each chasmata lineament and the average misorientation for each rift 106
Figure 3-10: Weighted average corona circularity and weighted average corona distance versus rift misorientation 107

Figure 3-11: Radar mosaic of Ozza Mons and the rifts in its vicinity 110
Figure 4-1: Mapping of Billy Mitchell caldera in Papua New Guinea 118
Figure 4-2: Caldera and stress orientations 122
Figure 4-3: Distribution of circularity and orientation of the 57 mapped calderas . 129
Figure 4-4: Misorientation between calderas and stress measurements 130
Figure 4-5: Relationship between distance-weighted average misorientation and distance-weighted average distance between calderas and the stress measurements 131
Figure 4-6: Fault map and stress measurements of El Salvador 134
Figure 4-7: Calderas and faults in the central portion of the Nazca-South American subduction zone 136
Figure 4-8: Fault map and stress measurements in Sumatra with the outlines of Toba Caldera (North) and Maninjau Caldera (South) 138

List of Abbreviations

NLH- Northern Leading Hemisphere
NTH- Northern Trailing Hemisphere
SLH- Southern Leading Hemisphere
STH- Southern Trailing Hemisphere
MBG- Minimum Boudning Geometry
BAT- Beta- Alta- Themis
IAU- International Astronomical Union
PPA- Pacific and North American Plates
AFS- African and Somalian Plates
AE- African and Eurasian Plates
AP- Australian and Pacific Plate
CC- Cocos and Caribbean Plates
NS- Nazca and South American Plate
JNA- Juan De Fuca and North American Plates
CCNA- Coco and North American Plates
EPH- Eurasian and Philippine Plates
AUE- Australian and Eurasian Plates

Chapter 1. Introduction: Planetary Interior Dynamics Across our Solar System

1.1 Introduction

This dissertation examines the morphology of various surface features on Europa, Venus, and Earth to understand the dynamic interaction between a planetary body's interior and surface. These three planetary bodies have a wide range of environments and geologic histories. However, they all exhibit surface features whose formation mechanism can be linked to the activity within their interior. Whether through direct mantle plume-lithosphere interactions or material intrusion into the lithosphere via chambers, sills, or dikes, these processes underscore the importance of interior dynamics in shaping planetary surfaces. These features give us insight into rocky planets and icy moons' thermal evolution, internal structure, and geologic potential. Comparing these three planetary bodies deepens our understanding of how internal processes drive surface change throughout the solar system and may inform our search for habitable environments.

1.2 Europa

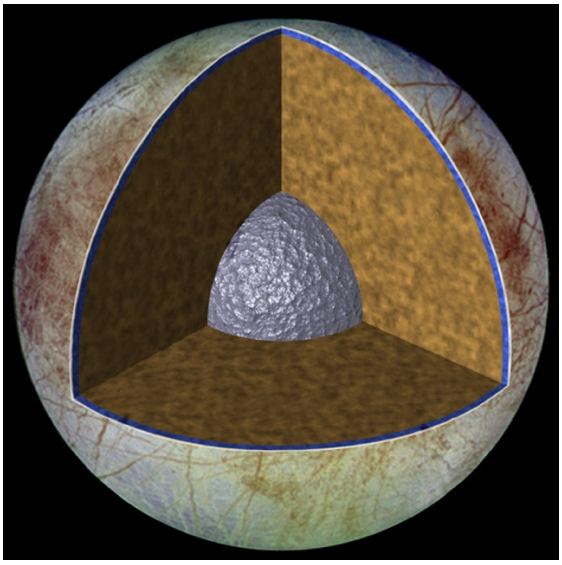


Figure 1-1: Hypothetical cross-section of Europa. Europa has a radius of 1,561 km and is thought to have a global subsurface ocean. Source: NASA/JPL

One of the defining characteristics of Europa, Jupiter's fourth-largest moon, is its liquid subsurface ocean (Figure 1.1). Magnetic field and gravity observations provided evidence of a nearly 150 km wide subsurface liquid H_2O ocean below an ice shell crust (Carr et al., 1998; Khurana et al., 1998; Kivelson et al., 2000). It has been shown that tidal heating due to Europa's eccentric orbit is enough to maintain its liquid layer (Cassen et al., 1980; Ojakangas & Stevenson, 1989; Ross & Schubert, 1987). Voyager and Galileo images also revealed a planetary surface lacking craters. Crater density models conclude that the age of Europa's surface is approximately ~56 My (Pappalardo et al., 1999). Recent studies have also provided evidence for active plumes in the southern hemisphere of Europa (Jia et al., 2018; Roth et al., 2014). These studies point to a geologically active planetary body that can exchange material from its interior to its young surface.

Current instrumentation limitations prevent us from directly studying Europa's subsurface ocean. One of Europa's richest datasets is the Galileo, Voyager 1, and Voyager 2 image mosaics. These mosaics reveal a surface whose features are thought to be formed by the subsurface ocean and ice shell interaction. Chaos and Microchaos, in particular, are the most likely candidates for formation through convective upwellings (Pappalardo et al., 1998). Chaos are large regions of resurfacing thought to have formed by melt-through from below (Collins et al., 2000; Greenberg et al., 1999). These features are categorized by hummocky textures and large rafts that can preserve the preexisting surface textures. Because these features cover such a large area and high-resolution imaging of the surface of Europa is limited, it is challenging to develop a database large enough to complete statistical analysis on these features. Microchaos, on the other hand, are much smaller but more prevalent in regions with higher resolution imaging than Chaos.

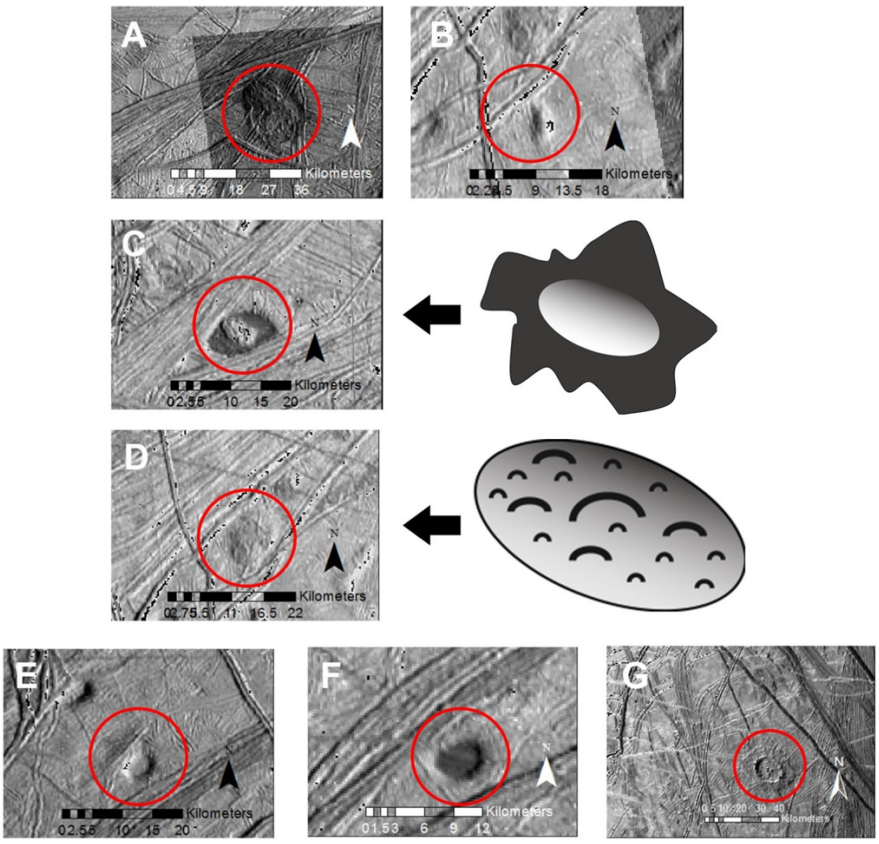


Figure 1-2: Different types of Microchaos on Europa: (a) chaos, (b) dome, (c-d) hybrids, (e) pit, (f) spot. (g) is an example of how craters look on Europa. Domes (b), pits (e), and spots (f) on average do not disrupt the preexisting surface, while chaos (a) and hybrids (c-d) do. Source: Noviello et al. (2019).

Microchaos can be domes, pits, spots, and small patches of chaos, Figure 2. Domes and pits are local topographic highs or lows, respectively. Domes and pits tend not to disrupt the local surface texture, but there are instances where a dome may have a crack. Spots are defined as low-albedo circular patches that retain the preexisting surface. The small patches of chaos within the Microchaos category resemble larger chaos features without the blocks of preexisting material. Despite the

morphological differences between these features, they are considered a part of the same population and may have evolved from one another (Culha & Manga, 2016).

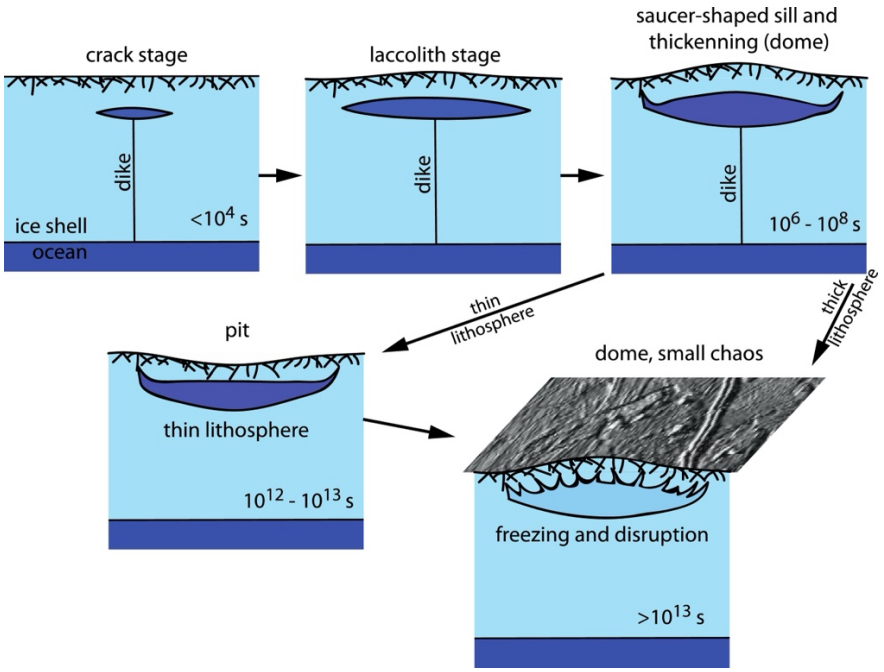


Figure 1-3: Formation model of microchaos on Europa. This model states that a sill is fed by a dike connected to the ocean. Domes can develop at the surface as the sill thickens and forms a saucer shape. Depending on the thickness of the ice shell, pits and small chaos can be formed at differing rates. Source: Manga & Michaut (2017)

There are six popular models for the formation of microchaos: melt-through (Carr et al., 1998; Goodman et al., 2004; Greeley et al., 1998; O'Brien et al., 2002; Thomson & Delaney, 2001), diapirism (Figueredo et al., 2002; Han & Showman, 2011; Mével & Mercier, 2007; Rathbun et al., 1998), brine mobilization by diapirism (Collins et al., 2000; Head & Pappalardo, 1999), brine mobilization driven by partial melt through (Pappalardo & Barr, 2004), sill formation (Figure 1.3) (Crawford & Stevenson, 1988; Manga & Michaut, 2017; Manga & Wang, 2007), and

cryovolcanism (Fagents, 2003; Quick et al., 2017, 2022; Steinbrügge et al., 2020). Most of these models involve the movement of subsurface material, which could result from the rise of a thermal diapir. This diapir can feed required sills or completely melt through the surface to create microfeatures. Han & Showman (2011) have shown that tidal dissipation can generate thermal convection in Europa's ice shell. This would enable the exchange of interior material to the surface. Further analysis of the formation of microchaos allows for a better understanding of the interior dynamics of Europa.

The Europa portion of this dissertation gathers new quantitative morphological measurements of microchaos. Our new database contains the orientation and elongation of nearly 1,000 microchaos. We use the orientation values of microchaos to understand their potential formation mechanism. Specifically, we investigate the role of global and regional stress on their formation and determine whether microchaos formation is episodic or continuous.

1.3 Venus

Venus has no plate tectonics, yet its surface age is similar to Earth's. A key mystery behind the age of Venus' surface is the style and extent of the resurfacing. Two main models are proposed for the resurfacing of Venus: a global catastrophic resurfacing event (Strom et al., 1994) or a directional history, where geologic activity on Venus can be broken into different epochs (Guest & Stofan, 1999; Ivanov & Head, 2013). Regardless of the resurfacing on Venus, tectonism and volcanism have played a significant role. Recent studies have even shown that Venus has ongoing volcanic activity (Herrick & Hensley, 2023). Because Venus lacks plate tectonics, mantle

plumes are required to create the volcanism and tectonism we see on the surface (Phillips & Hansen, 1998; Reese et al., 1999; Smrekar et al., 2018). Therefore, studying features on Venus that have evidence for volcanism and tectonism, like coronae, provides insight into the interior dynamics and evolution of Venus.

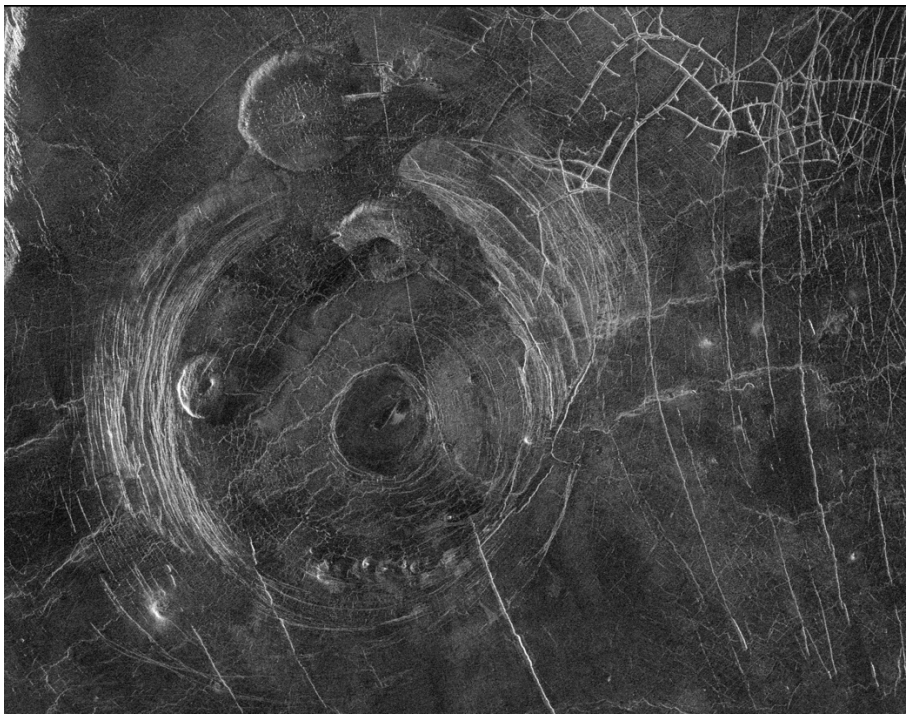


Figure 1-4: Magellan Radar image of Aine Corona. A corona's distinctive annuli can be seen in the southwestern portion of the image. This image is approximately 300 km across and is centered on 59°S and 164°E Source: NASA/JPL.

Coronae are ovoid-shaped features that range from 200 km to 1000 km in diameter. These features are defined by their large annuli of fractures, Figure 1.4. Their annuli can span 360° or be incomplete. There are five common coronae morphologies: concentric, concentric-double ring, radial-concentric, asymmetric, and multiple (Pronin & Stofan, 1990; Stofan et al., 1992). These five classes of coronae

are determined by the shape of the annulus, level of volcanism, and tectonic style. Coronae also have a wide range of topographic signatures. There are examples of coronae having domes, plateaus, depressions, rims, troughs, and no topographic signature (Smrekar & Stofan, 1997). These features are formed globally on Venus but have been found to occur predominantly in clusters and near Chasmata, large extensional rift systems (Squyres et al., 1993; Stefanick & Jurdy, 1996; Stofan et al., 1992).

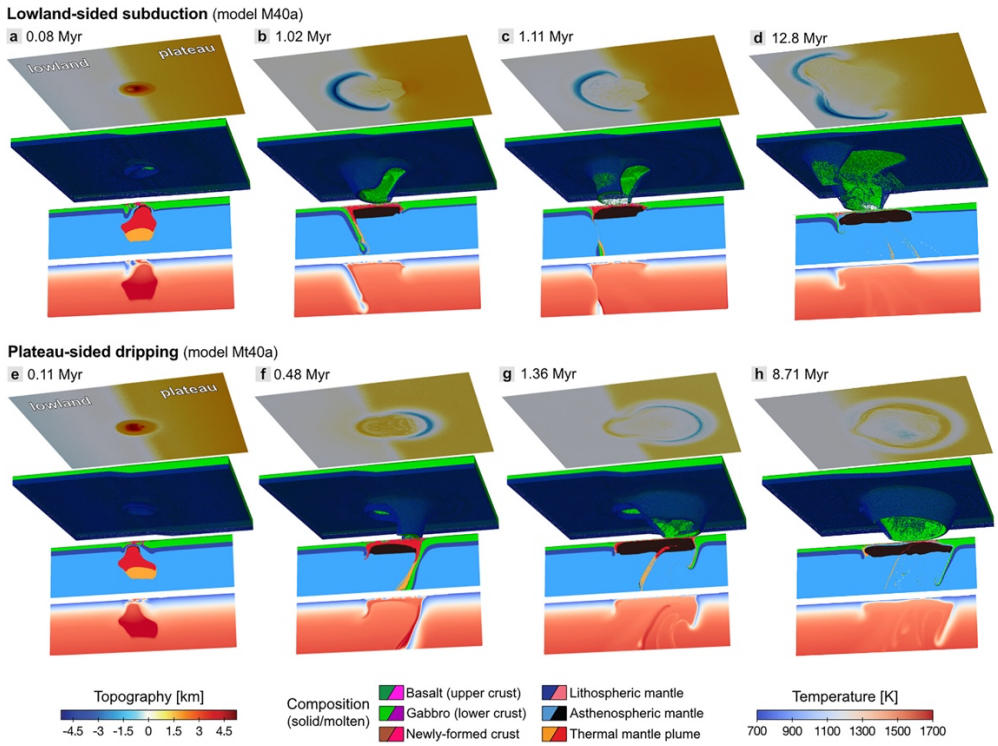


Figure 1-5: 3D models of a diapir rising through the mantle and initiating subduction as it interacts with the lithosphere (a-d). These models focused on creating topographically asymmetric coronae. Their model relies on a difference in lithospheric thickness to create the topography observed. Source: Gülcher et al. (2023)

Studies have proposed an evolutionary formation scheme to explain the extensive morphological range of coronae. There are three dominant models for coronae formation: 1) rising mantle plume/diapir, 2) sinking mantle diapir, and 3) gravitation relaxation. In Gülcher et al. (2023), topographic signatures of coronae are replicated by modeling a diapir that reaches the lithosphere and triggers subduction of the lower lithosphere (Figure 1.5). Other models rely on diapirs to make the initial stage of a corona, but gravitation relaxation is the dominant process in which the morphology of the corona varies over time (Stofan et al., 1991). Volcanism is also considered an essential process for some coronae (Magee Roberts & Head, 1993). Coronae on Venus, therefore, should be treated as a record of Venus' mantle plume activity. By studying their morphology and relationship to other features of Venus, we can develop a more extensive understanding of Venus' geological activity.

The chapter on Venus presents an expanded and digitized version of the Stofan et al. (1992b) coronae database. We add new morphological measurements to this dataset, like the orientation and elongation of coronae. We then compare the coronae's orientation to the chasmata lineaments' strike to test whether regional or global stresses influence the coronae's shape.

1.4 Earth



Figure 1-6: Billy Mitchell is a 2 km wide caldera located in Papua New Guinea. Two large eruptions have occurred at this caldera about 900 and 370 years ago. Source: Wally Johnson, 1989.

Volcanoes have historically posed a significant threat to humans on Earth. An important aspect of volcanoes is their magma chambers. Magma chambers are critical in understanding how Volcanoes erupt (explosive or effusive) and how often. Studying magma chambers is difficult because they can be located 5 to 10 km beneath the surface (Annen et al., 2006). Seismological (Lees, 2007), gravity (Gottsmann et al., 2003), and magnetic (Fluegel et al., 2022) studies have been conducted to determine the location and activity of magma chambers. These studies can be limited by scale, so global analysis of magma chambers can be time-intensive and costly. We argue that surface features that can be used to study the morphologies and emplacement of magma chambers indirectly are calderas.

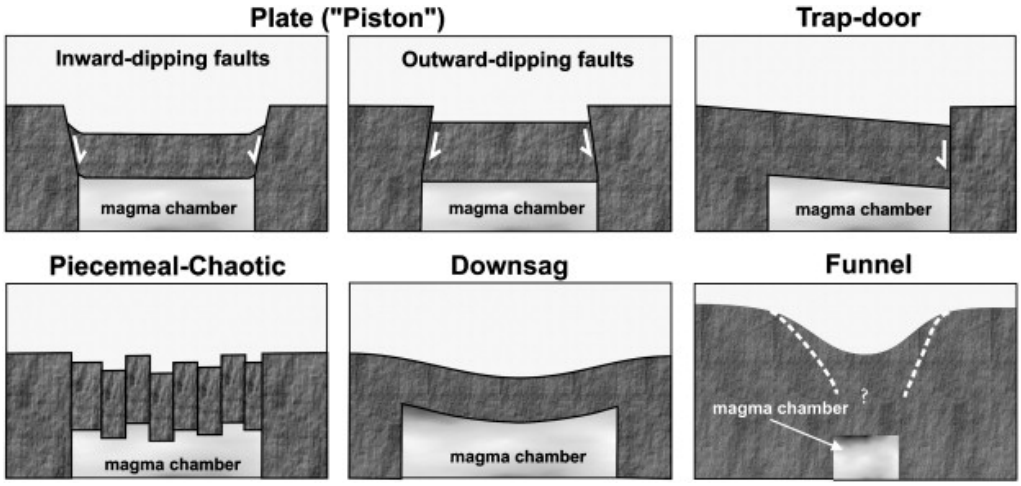


Figure 1-7: Four different styles of subsidence that cause the formation of Calderas. Source: Geyer & Martí (2008)

Calderas are features formed by the removal of magma from magma chambers—the eruptive activity results in the collapse or subsidence of caldera material into the magma chamber (Cole et al., 2005). By studying the morphology of calderas and their floors, five different forms of subsidence have been defined: plate, piecemeal, trapdoor, down sag, and funnel (Figure 1.7) (Lipman, 1997). Each of these styles of subsidence provides insight into the shape and depth of a magma chamber. Various studies have shown that the magma chamber's morphology determines the caldera's morphology (Branney & Acocella, 2015; Geshi et al., 2023; Gudmundsson, 2008; Kusumoto & Takemura, 2005). Therefore, studying Calderas allows us to gain insights into the emplacement and morphologies of magma chambers.

Our research on Earth uses calderas to investigate the role of lithospheric stresses on the shape of calderas and indirectly the shape of magma chambers. We mapped calderas identified by the Global Volcanism Program & Venzke (2024) data. We predominantly mapped calderas with well-defined rims as seen in Figure 1.6. In

MATLAB, we calculated the orientation and elongation for each caldera. This method ensured that we calculated these quantitative morphological measurements independently of map projection. Unlike Europa and Venus, Earth contains direct stress measurements. We utilized the Heidbach et al. (2018) world stress map to compare caldera orientations to different stress regimes.

Chapter 2. Orientation of Microfeatures on Europa

2.1 Abstract

Microfeatures, including pits, spots, domes, hybrids, and microchaos, are among the most abundant features on the surface of Europa. Therefore, better understanding them will deepen our knowledge of geologic activity and the geodynamics of Europa. Here, we systematically determine the elongation and orientation of a dataset of nearly 1,000 previously mapped microfeatures in four regions of Europa. We demonstrate that microfeatures are systematically elongated and that this elongation is likely the result of interactions between a horizontal stress field and a diapir or liquid water body beneath the microfeature. Circular statistics tests show that microfeatures are often associated with a regionally consistent preferred orientation, which is particularly pronounced for pits and domes, while being more variable for hybrids and domes. These observations are consistent with a formation model in which pits and domes evolve into hybrids and chaos. Additionally, microfeature formation appears to be episodic and regionally restricted. Stress apparently changed between episodes of microfeature formation; however, the lack of detailed stratigraphy renders it premature to use microfeature orientation as a probe into the past stress states of Europa's shell

2.2 Introduction

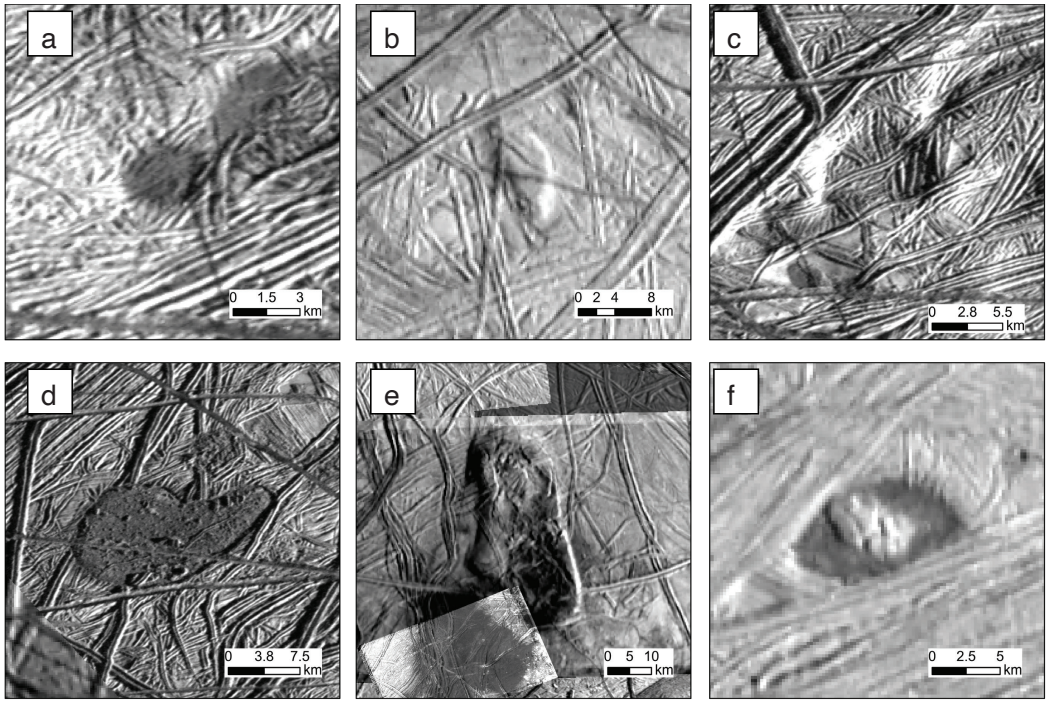


Figure 2-1: Example of microfeatures on Europa. Microfeatures exhibit various morphologies (Pappalardo et al., 1998), including spots (A), domes (B), and pits (C). The example in D is described as a microchaos due to its hummocky and knobby texture. E and F have both been previously classified as uplifts with cracks (Greenberg et al., 2003) or chaos (Figueredo & Greeley, 2004). All the features in this figure are located in the trailing hemisphere of Europa

The images of Europa returned by the Voyager and Galileo probes reveal a surface with a complex geologic history (Lucchita & Soderblom, 1982; Greeley et al., 2000; Doggett et al., 2009; Leonard et al., 2024). Much work has been conducted to understand the formation and significance of linear features, such as bands and ridges, that riddle Europa's surface (e.g., Prockter & Patterson, 2009). However, the surface

is also scattered with relatively small circular to elliptical features that exhibit morphologies suggesting an endogenic origin (Greeley et al., 1998). A better understanding of these features, which we refer to as "microfeatures," has the potential to reveal new aspects of Europa's icy crust and its evolution.

Previous studies have discussed the variation in microfeature relief, morphology, and global distribution origins (Riley et al., 2000; Greenberg et al., 2003; Culha & Manga, 2016; Noviello et al., 2019a). Many concluded that microchaos are a manifestation of warm ice diapir (Rathbun et al., 1998; Pappalardo et al., 1998; Pappalardo & Barr, 2004), cryomagmatic intrusions (Michaut & Manga, 2014; Manga & Michaut, 2017), or cryovolcanic flows (Fagents, 2003; Miyamoto et al., 2005; Quick et al., 2017). Here, we seek to understand whether the development of microfeatures is influenced by stress, which could provide further constraints on their origin. To do this, we measure the elongation and orientation of the large dataset of microfeatures mapped by Noviello et al. (2019a, b) on high-resolution regional mosaics and investigate systematic relations between orientation and location or microfeature category.

Microfeatures have diameters ranging from approximately 10 to 20 km (Greenberg et al., 2003). Their morphology is extremely varied, and there is no settled nomenclature for these geological objects. The terms "lenticulae," "PSDs," and "microchaos" have been used at various points to describe them but only apply to a subset. Therefore, we choose to use the more general term "microfeatures."

Microfeatures categories encompass domes, pits, spots, and small chaos (Figure 2.1). Domes exhibit a positive topography inferred from shadow patterns

(Figure 2.1B), while pits are features characterized by a perceived negative topography (Figure 2.1C). Spots are enclosed features with a lower albedo than the surrounding terrain but no discernible relief (Figure 2.1A). Together, these features contribute to the mottled appearance of some geological units (Lucchita & Soderblom, 1982). They are referred to as "PSDs" for Pits, Spots, and Domes, but this term overlooks the possible link between these features and larger "Chaos" terrain (Greenberg et al., 2003). The term "uplifts" is sometimes used instead of domes to emphasize the lack of surface disruption. However, this term implies an endogenic origin, either as a diapir (Rathbun et al., 1998; Michaut & Manga, 2014) or an intrusion. An alternative cryovolcanic origin has been proposed for these features, involving intrusive or extrusive cryomagmatic origins (Fagents, 2003; Quick et al., 2017), so we favor the usage of the purely descriptive term "dome."

Some microfeatures exhibit a clearly disrupted surface (Figures 1D-F) akin to chaos, though on a smaller scale, and have thus been referred to as "microchaos" (Pappalardo et al., 1998; Leonard et al., 2024). Two types of chaos textures, knobby chaos and hummocky chaos, have been previously identified at large scale (Greeley et al., 2000). Knobby chaos features irregularly shaped knobs disrupting its interior, while hummocky chaos contains plates of the previous terrain embedded in a hummocky matrix. In contrast to hummocky chaos, knobby chaos is generally smoother and does not have many plates of the pre-existing terrain. This distinction is not frequently recognized in smaller chaotic features. Here, we will use the terms pits, spots, and domes to describe microfeatures that do not disrupt the surface, and use chaos and hybrid otherwise.

The term “lenticulae” has been used as an umbrella term for domes, spots, pits, and small-chaos features (Greeley et al., 1998; Spaun et al., 1999; Pappalardo, 2000; Pappalardo & Head, 2001). However, this term, which is not currently listed in the Gazetteer of Planetary Nomenclature (USGS Astrogeology Science Center, n.d.), was originally defined to describe low-albedo spots visible in low-resolution images without resolvable topographic relief (Greenberg, 2015). As a result, lenticulae should only be used as a reference to spots (Greenberg et al., 2003). For simplicity, we will not use this term here. Note that none of the terms mentioned here is an official descriptor term, according to the IAU’s Working Group for Planetary System Nomenclature (USGS Astrogeology Science Center n.d.).

Previous studies have mapped and discussed microfeature morphologies (Collins & Nimmo, 2009; Culha & Manga, 2016; Figueredo et al., 2002; Figueredo & Greeley, 2000; Greeley et al., 1998, 2000; Greenberg et al., 1999, 2003; Leonard et al., 2018; Noviello et al., 2019a; Pappalardo et al., 1998; Riley et al., 2000; Singer et al., 2021; Spaun et al., 1999). Greenberg et al. (2003) document two types of pit and uplift size distributions exhibiting antipodal symmetry. They identified similar pit and uplift sizes in the northern leading and southern trailing hemispheres. In contrast, Singer et al. (2021) conclude that a peak in size distribution for all features occurred at 5-6 km^2, regardless of location on Europa. The differences in these results may be attributed to improved imaging and varied feature classifications.

Stratigraphic maps show that microfeatures are among the youngest features on Europa (Doggett et al., 2009; Figueredo & Greeley, 2004; Prockter et al., 1999). These maps have also indicated that microfeatures may have formed in different

episodes (Figueredo & Greeley, 2004). Mével & Mercier (2007) showed that Thera Macula, a large dome situated in the trailing hemisphere of Europa, developed in three stages: a doming stage, a collapse and extrusion stage, and a relaxation stage. Parro et al. (2016) reached a similar conclusion when studying the Argadnel Regio region. Their stratigraphic map records two discrete chaos formation episodes that resulted in two morphologically distinct chaos groups

Culha & Manga (2016) analyzed the orientation of 580 microfeatures in the leading and trailing anti-Jovian and sub-Jovian quadrants. They determined the orientation of these features by employing the least-squares method to fit ellipses to the microfeatures. The pits they identified exhibited a preferred northwest-southeast elongation, whereas the chaos and domes showed no preferred orientation. This analysis was performed not regionally but by considering all features collectively. In this study, we build upon their work by utilizing the microfeature map from Noviello et al. (2019b), which contains microfeatures imaged during the E17 and E15 flybys of the Galileo mission. The Noviello et al. (2019b) map includes approximately twice as many microfeatures as those considered by Culha & Manga (2016). We add information on elongation and orientation to the data associated with each microfeature. With this enriched dataset, we aim to deepen our understanding of the morphological characteristics, potential evolution, and stress influences on microfeatures on Europa

2.3 Methods

2.3.1 Microfeature database

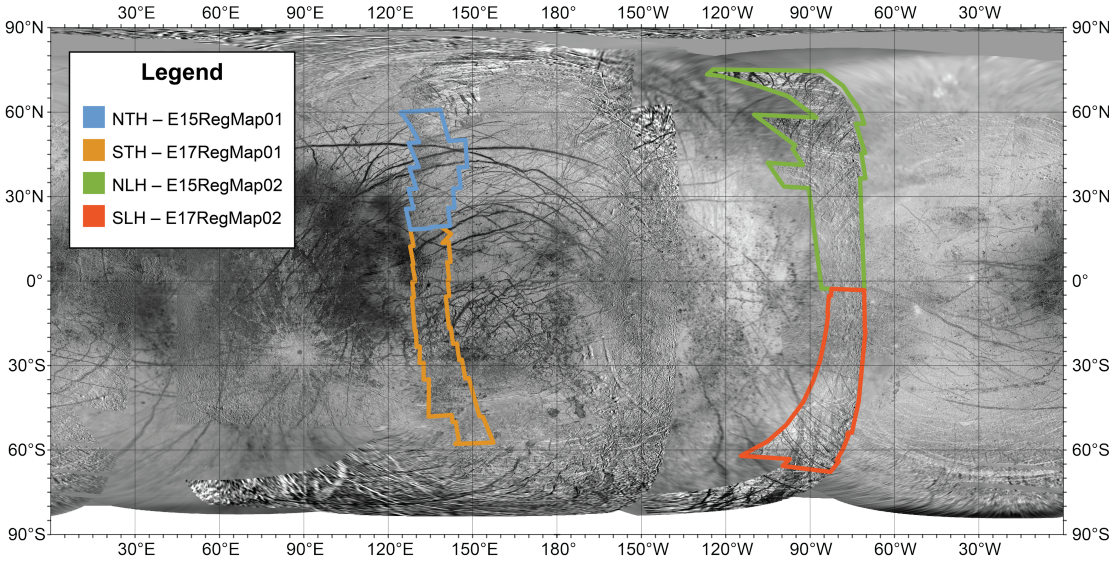


Figure 2-2: Outlines of the four regions mapped by Noviello et al., (2019a, b) and the names of the mosaics on which these maps are based. E15RegMap01 (blue) and E17RegMap01 (orange) are located predominantly in the Northern and Southern trailing hemisphere, respectively, while E15RegMap02 (green) and E17RegMap02 (red) are located predominantly in the Northern and Southern leading hemisphere, respectively. These colors are used consistently in this paper to indicate the different mapped regions.

Noviello et al. (2019b) created the most extensive and systematic map of microfeatures to date. They provided shapefiles for 918 microfeatures in four different regions of Europa (Figure 2.2) covered by the E15RegMap01, E15RegMap02, E17RegMap01, and E17RegMap02 Galileo mosaics. Two of these regions are located in the trailing hemisphere, while the other two are in the leading hemisphere of Europa. In each hemisphere, the E15 and E17 orbits primarily cover

the northern and southern hemispheres, respectively. Thus, we refer to the mapped regions as Northern Trailing Hemisphere (NTH- E15RegMap01), Southern Trailing Hemisphere (STH- E17RegMap01), Northern Leading Hemisphere (NLH- E15RegMap02), and Southern Leading Hemisphere (SLH- E17RegMap02). Note that the maps are not perfectly bounded by the equator (Figure 2.2), so the terms "northern" and "southern" are used for convenience only.

The Noviello et al. (2019b) dataset contains the outlines of 1,035 features, expanding on the 691 microfeatures discussed in Noviello et al. (2019a) to a total of 275, 314, 112, and 217 microfeatures of all types in the NLH, NTH, SLH, and STH map areas, respectively. This dataset also encompasses 21 craters and 94 unclassified features. The shapefiles are linked to sinusoidal map projections with different central meridians for each region: 283.0°, 137.0°, 279.5°, and 143.7° in the NLH, NTH, SLH, and STH map areas, respectively

Noviello et al. (2019b) indicate the feature type, central latitude, central longitude, orientation, semi-major length, semi-minor length, and elongation of each mapped feature. Elongation was defined as the semi-major length divided by the semi-minor length of the microfeature. The feature types include dome, pit, spot, chaos, crater, hybrid I, and hybrid II, based on the definitions summarized here:

1. Chaos: An enclosed feature characterized by a clear disruption of the surface, lacking clear evidence (shadows) of topographic change across the feature. These features were not subdivided into platy and hummocky chaos (Figure 2.1D).

2. Dome: An enclosed feature with a shadow gradient, where the brightest sections face the sun, indicating positive relief. No distinctions were made between uplifts (Greenberg et al., 2003) and domes (Figure 2.1B).
3. Pit: An enclosed feature with a shadow gradient, whose darkest section faces the sun, indicating negative relief (Figure 2.1C).
4. Spot: An enclosed feature with a consistently dark albedo (Figure 2.1A.
5. Hybrid I: A positive topographic feature within a dark halo. It appears to be a combination of a dome and a spot (Figure 2.1F).
6. Hybrid II: A positive topographic feature with a fully disrupted surface. These features have been previously classified as chaos (Figueredo and Greeley, 2004) or uplifts (Greenberg et al., 2003) (Figure 2.1E).
7. Crater: A circular feature with negative topography and a well-defined rim.

The Noviello et al. (2019b) dataset indicates the microfeature types for a total of 981 microfeatures, although it does not differentiate between Hybrid I and Hybrid II. Here, we use all of the microfeatures in that database, including one that is larger than 100 km^2.

2.3.2 Microfeature orientation

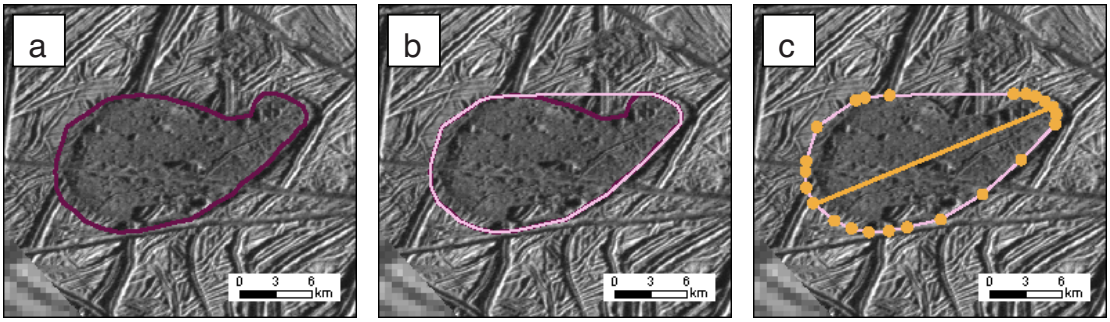


Figure 2-3: Breakdown of the minimum bounding geometry tool in ArcGIS. (a) Shows the imported Noviello et al., (2019b) microfeature shapefile. The minimum bounding geometry tool takes the vertices of the shape file (b) and creates a new polygon with the smallest perimeter that can contain all of the vertices (c).

We systematically collected morphometric information for each microfeature in the Noviello et al. (2019b) database. Some of it, like microfeature area, duplicated information in the database, but we nevertheless recalculated it here to be consistent with the method we used to collect new information, such as microfeature orientation.

The geometrical characteristics of each microchaos were calculated using ArcGIS Pro. First, we imported the microfeature shapefiles and the Europa Voyager-Galileo SSI Global Mosaic into ArcGIS Pro. The global mosaic is used solely for reference. We chose not to use the more recent Bland et al. (2021) mosaic since we were not conducting additional mapping that would necessitate the highest possible resolution (Noviello & Rhoden, 2021). However, the Europa Voyager-Galileo SSI Global Mosaic was set to a simple cylindrical projection, which differs from the projection of the microfeature shapefiles. This inconsistency must be carefully addressed managed.

The area of each microfeature was calculated using the area tool in ArcGIS Pro. This calculation was performed in the projection associated with the original microfeature database, which, being sinusoidal, preserves area. We calculated the aspect ratio and orientation of the feature using the Minimum Bounding Geometry (MBG) tool in ArcGIS Pro. This tool analyzes a set of points, lines, or polygons and generates a new polygon shapefile that includes an attribute table with orientation, minimum width, and maximum length values. The MBG can be defined in several ways, including the rectangle with the minimum area, the rectangle with the minimum width, or the circle that encloses the polygon. We chose to define the MBG as the convex hull (Figure 2.3) because it is the polygon with the shortest perimeter that fully encloses a set of points or a polygon. The orientation of the MBG is defined as the angle between the line connecting the two MBG vertices separated by the longest distance and north. Orientation values calculated using this method range from 0 to 180 degrees. For comparison, Culha & Manga (2016) use the orientation of the semi-major axis of the ellipse that best fits their mapped microfeature outline. Our method better represents the sometimes significant roughness of the microfeature outline (Figure 2.3). Finally, we calculated the circularity of each microfeature by dividing the minimum width by the maximum length of the MBG. Circularity ranges from 0 for a thin line to 1 for a circle. Note that circularity is the inverse of elongation reported by Noviello et al. (2019a). We prefer to discuss circularity because this quantity is bounded by 0 and 1, unlike elongation, which can reach infinity.

Properly running the ArcGIS MBG tool requires that all microfeature shapefiles use the same projection. To achieve this, we combined all the microfeature

shapefiles into a single shapefile using the ArcGIS Join tool. At this stage, we selected a Mercator projection, which is conformal. If we had retained the original sinusoidal projections, microfeatures that do not lie along the central meridian would have become warped, resulting in inaccurate MBG orientation. We verified the orientations calculated in ArcGIS by comparing them with projection-independent estimates obtained using bespoke MATLAB code. In this alternative method, we first imported the Noviello et al. (2019b) shapefiles into MATLAB using the mapping toolbox. Each microfeature is outlined by a sequence of vertices defined by X and Y coordinates, averaging 12 vertices per microfeature. We converted these coordinates into latitude and longitude using the inverse projection function in MATLAB. Then, we calculated the geodesic distances separating each pair of vertices, identified the vertices separated by the 90^{th} percentile of the longest distances, and calculated the azimuths of the lines connecting these vertex pairs, averaging them to obtain the orientation for each microfeature. This method is projection-independent and considers the original microfeature outline without defining a MBG. The orientations calculated using the ArcGIS MBG function in a Mercator projection and our bespoke MATLAB code differ by only 0.1 degrees on average. As expected, repeating this test with a simple cylindrical projection or a sinusoidal projection led to greater orientation differences. Both approaches offer complementary advantages: the MATLAB- based method provides an estimate of uncertainty but depends on the number of vertices in the shapefile, while the ArcGIS method is less sensitive to slight variations in the shape outline, facilitating the integration of its results with

other measurements collected on each microfeature. Here, we only discuss results obtained from ArcGIS orientation determinations.

2.4 Circular statistics

Orientation constitutes non-directed axial data. We use circular statistics methods (Fisher, 1993; Mardia & Jupp, 1999) to analyze this data and reveal regional variations or links with microfeature types. We report the mean direction and circular variance for each dataset. These values, however, do not provide any information about the type of distribution the dataset may have. It will become of interest to investigate whether a dataset is uniformly distributed. We use three approaches for testing uniformity: the Pearson χ^2, the Rayleigh Test, and the Modified Kuiper Test. These methods have been implemented in Mathematica functions available at Nuñez & Montesi (2025). Here, we summarize the methods used in this study.

2.4.1 Mean Direction

The average direction of a set of directional data is the orientation of the resultant vector $\vec{R}$, which is the sum of all the unit vectors aligned with each directional measurement. As the azimuth θ of our axial data is non-directed, there is a 180°-ambiguity in the dataset. Unlike directed data, θ ranges only from 0° to 180°, and adding 180° to a measurement is an equally valid description of the data. This ambiguity is well-recognized in the field of circular statistics. It has been shown that it is appropriate to double the orientation value before constructing the resultant vector (Fisher, 1993; Mardia & Jupp, 1999). In other words, we average the quantity 2θ, which ranges from 0° to 360°, and halve the result to obtain $\bar{\theta}$.

In practice, the components of $\vec{R}$ are given by the averages of the x- and y-components of the unit vectors oriented in each 2θ direction:

$$\vec{R} = \begin{bmatrix} \bar{C} \\ \bar{S} \end{bmatrix} \tag{2.1}$$

$$\bar{C} = \frac{1}{n}\sum_{j=1}^{n} \cos 2\theta_j \,, \qquad \bar{S} = \frac{1}{n}\sum_{j=1}^{n} \sin 2\theta_j \tag{2.2}$$

where n is the total number of data points. The orientation of $\vec{R}$ is given by the arctangent of $\bar{S}/\bar{C}$, so that

$$\bar{\theta} = \begin{cases} \dfrac{1}{2}\operatorname{atan}\dfrac{\bar{S}}{\bar{C}} & \text{if } \bar{C} \geq 0 \\ \dfrac{1}{2}\operatorname{atan}\dfrac{\bar{S}}{\bar{C}} + 90° & \text{if } \bar{C} < 0 \end{cases} \tag{2.3}$$

2.4.2 Circular variance and uncertainty

The variance of a circular dataset is not expressed as an uncertainty of the mean direction. Instead, the circular variance, V, is linked to the length of the resultant vector, $\bar{R} = \sqrt{\bar{C}^2 + \bar{S}^2}$, as

$$V = 1 - \bar{R} \tag{2.4}$$

The circular variance ranges from 0 to 1, where values closer to 0 signify a tighter distribution around the mean, while 1 corresponds to a broader distribution. Mardia (1972) proposed defining the circular standard deviation as $\sqrt{-2\ln \bar{R}}$, but this quantity still does not correspond to an uncertainty in the mean direction.

Here, we visualize uncertainty in mean orientation by calculating the standard deviation of the difference between each sample and the mean orientation, restricted to ±90°. Unlike the circular variance V, this construction is not a rigorous uncertainty

estimate and is used solely for visualization. It serves as a good measure of the data's spread only if the distribution is closely centered around its mean; that is, if V is close to 0.

2.4.3 Pearson χ^2 test

This test relies on the assumption that if a distribution is uniform, then the frequency of samples should be the same in every bin of an orientation histogram (McKillup and Dyar, 2010). Therefore, this test is based on comparing the observed frequency of a given bin to what is expected of a uniform distribution. To conduct this test, we bin an orientation sample and record f_i, the frequency of each bin. The expected frequency, e_i, is calculated by multiplying the number of measurements in the dataset by the fraction of the possible values covered by bin i. In our case, we choose to use 12 uniformly spaced bins, each covering 15° of the range of possible θ values. The χ^2 is then calculated as

$$\chi^2 = \sum_{i=1}^{n_b} \frac{(f_i - e_i)^2}{e_i} \tag{2.5}$$

where n_b is the number of bins.

The possibility that a given dataset is uniformly distributed is evaluated by comparing χ^2 to a critical value that expresses the probability that the observed distribution is not a randomly sampled uniform distribution. This probability is given by a chi-square distribution with ν degrees of freedom. With 12 bins, and $\nu = 11$, and we consider that the distribution passes the test if we can reject the null hypothesis that the distribution is uniform with a confidence of 95% (p=0.05), that is,

if χ^2 exceeds 19.675 (Appendix A1 of McKillup & Dyar, 2010). The Pearson χ^2 test is consistent against all alternatives to uniformity.

2.4.4 Rayleigh Test

If a distribution is uniformly distributed, the resultant vector should have a very small length, ideally 0. Random sampling prevents this perfect case from being realized. Therefore, the Rayleigh test compares the resultant vector's length $\bar{R}$, to a scoring statistic S^* (Mardia & Jupp, 1999) that also follows a chi-square distribution. The classical scoring statistic, valid to order n^{-1} is

$$S^* = 2n\bar{R}^2 \tag{2.6}$$

However, for small datasets, it is better to use the modified S_m^*, valid to order n^{-2} (Cordeiro & Ferrari, 1991):

$$S_m^* = \left(1 - \frac{1}{2n}\right) 2n\,\bar{R}^2 + \frac{n\bar{R}^4}{2} \tag{2.7}$$

The relevant number of degrees of freedom in this test is $\nu = 2$. Therefore, an orientation dataset will be considered non-uniform if we can reject the null hypothesis of uniformity with 95% confidence (p=0.05), that is, if S_m^* is greater than 5.991. The Rayleigh test is consistent against all alternatives to uniformity.

2.4.5 Modified Kuiper Test

The modified Kuiper test mirrors statistical tests developed for non-circular data sets, specifically the Kolmogorov-Smirnov test. The Kolmogorov-Smirnov test measures the deviation between the empirical and hypothesized cumulative distribution functions. The test statistic associated with this test is based on the maximum difference between these distribution functions. Kuiper (1960) adapted the

Kolmogorov-Smirnov test for circular data. Before performing any calculations, the orientation values are ranked from smallest to largest and scaled by the largest possible value, 180°.

$$U_i = \frac{\theta_i}{180}, \qquad i = 1,2,3,4 \ldots . n \tag{2.8}$$

For each angle, the difference with a uniform distribution is given by

$$D_i = U_i - \frac{i}{n} \tag{2.9}$$

The deviation V_n is based on the maximum and minimum deviation values

$$V_n = \max_{1 \le i \le n}(D_i) - \min_{1 \le i \le n}(D_i) + \frac{1}{n} \tag{2.10}$$

V_n is then used for calculating the modified Kuiper test statistic, V_n^*:

$$V_n{}^* = V_n\left(n^{\frac{1}{2}} + 0.155 + 0.24\, n^{-\frac{1}{2}}\right) \tag{2.11}$$

This test statistic is compared to distribution given by Kuiper (1960), $Q = 1 - \sum_1^\infty 2\left(4j^2 V_n^{*2} - 1\right) \exp -2j^2 V_n^{*2}$ and, approximated by Stephens (1970) as $Q^* = 1 - \left(8V_n^{*2} - 2\right) \exp -2V_n^{*2}$. An orientation dataset will be considered non-uniform if we can reject the null hypothesis of uniformity with $Q = 95\%$ (p=0.05), that is, if V_n^* exceeds 1.747. Note that this test is not reliable for sample sizes smaller than 8. Like the Rayleigh and the Pearson χ^2 test, the Kuiper test is consistent against all alternatives to uniformity.

2.5 Results

The orientation of each mapped microfeature is illustrated in Figure 2.4. In this figure, each microfeature is represented by a point that is color-coded according

to orientation, with a size that reflects the area of the microfeature. At first glance, there is no systematic pattern in the distribution of microfeature area and size, except perhaps in the SLH (E17RegMap02 region), where the microfeatures appear smaller than those in other map areas and seem predominantly oriented in a direction close to N-S.

The statistical analyses described in the previous section aim to enhance understanding of these results, particularly by highlighting relationships between microfeatures of different types. The outcomes of these analyses are compiled in Table 1, which presents the mean surface area, circularity, and orientation of microfeature sets separated by region, along with the results of the test statistics outlined earlier. In each region, we analyze samples composed of a single microfeature type as well as all microfeatures regardless of classification. Since the size distributions often appear log-normal, we report the average of $\log_{10} A$, where A is the microfeature area in km^2. This is equivalent to calculating the geometric mean of the measured areas, $\bar{A} = (\prod_{i=1}^{n} A_i)^{1/n}$. Next, we outline the characteristics of microfeatures, test whether their orientation is uniformly distributed in each mapped region, compare the characteristics of each microfeature type, and examine how orientation may differ by latitude. We also consider whether the most elongated microfeatures dominate our results. Table 2 summarizes the inferred orientation distribution for each combination of map area and microfeature type, along with the significance of the various statistical tests performed on each dataset. Probability density functions for microfeature area and circularity are illustrated in Figure 2.5.

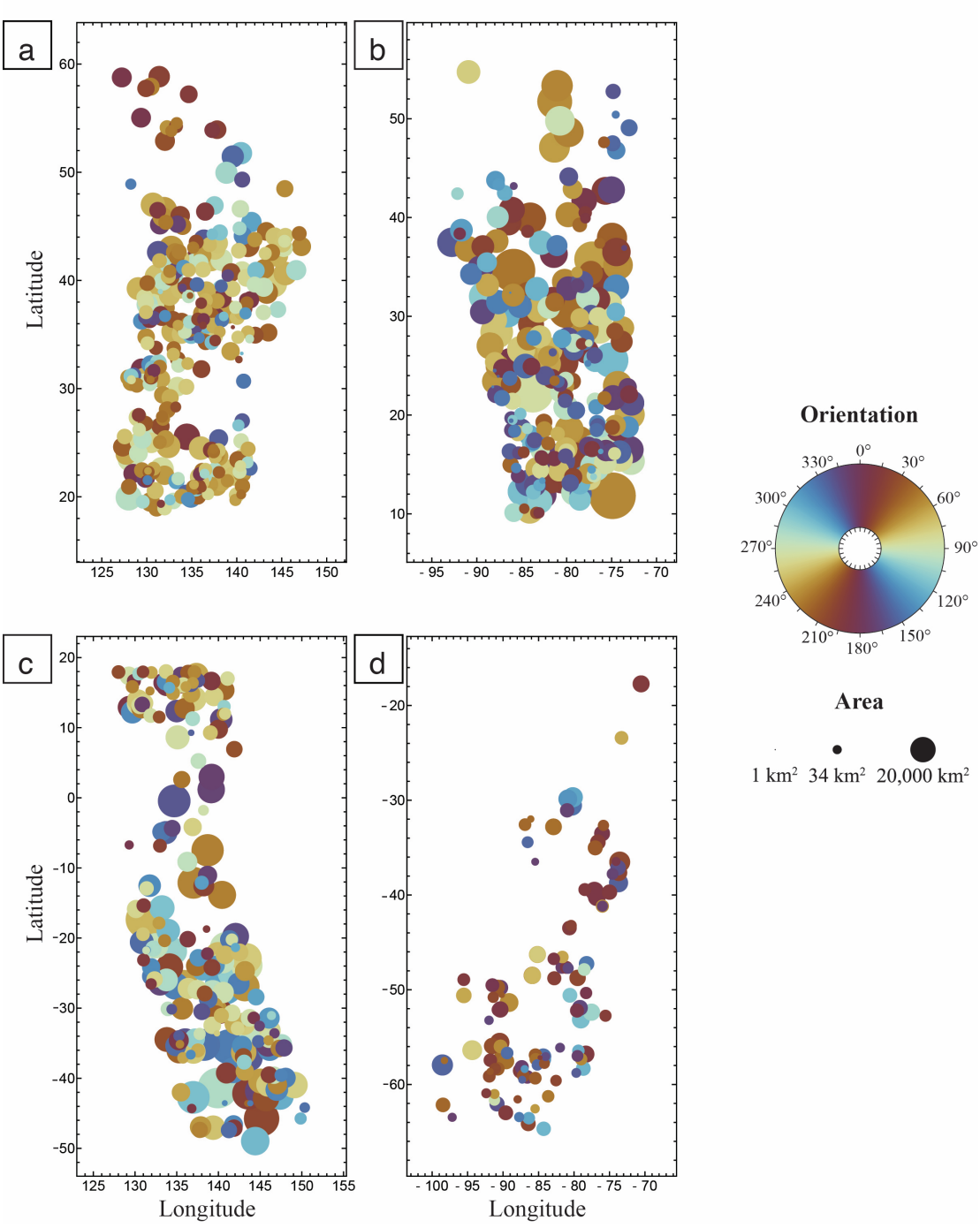


Figure 2-4: Location of all mapped microfeatures, color-coded according to orientation. The point size is scaled to the square root of microfeature surface area.

Table 2-1: Orientation statistics for all mapped microfeatures

Region	Type	Number	Average log10(Area)	Average circularity	Average orientation	Circular variance	Pearson test χ^2	Rayleigh test S_m^*	Modified Kuiper Test V_n^*
Northern Leading E15RegMap02	Pit	10	0.82	0.681	140 ± 17°	0.152	26.0	15.30	0.729
	Spot	1	0.96	0.837	027°	0	11.0	1.50	1.000
	Dome	30	1.01	0.630	169 ± 34°	0.479	26.8	16.67	0.411
	Hybrid	25	1.52	0.641	170 ± 32°	0.422	40.8	17.10	0.498
	Chaos	209	2.11	0.639	034 ± 48°	0.897	13.9	4.0	0.113
	All	275	1.88	0.640	001 ± 47°	0.862	23.2	10.96	0.126
	Craters	7	1.32	0.868	084 ± 40°	0.629	5.0	2.30	0.362
Northern Trailing E15RegMap01	Pit	120	1.39	0.673	051 ± 37°	0.548	59.0	49.46	0.329
	Spot	24	1.20	0.687	093± 37°	0.589	10.0	8.47	0.351
	Dome	34	1.26	0.654	009 ± 42°	0.652	2.9	9.10	0.319
	Hybrid	39	1.59	0.673	062 ± 38°	0.616	30.2	11.91	0.283
	Chaos	97	1.81	0.650	069 ±34°	0.452	82.5	58.62	0.405
	All	314	1.52	0.665	060 ± 39°	0.621	114.8	90.43	0.249
Southern	Pit	67	1.16	0.666	016 ± 31°	0.430	42.4	44.02	0.391
	Spot	1	0.82	0.500	004°	0	11.0	1.50	1.000

	Dome	21	1.22	0.758	022 ± 32°	0.418	23.0	14.61	0.461
	Hybrid	10	1.50	0.684	164 ± 45°	0.753	6.8	1.67	0.307
	Chaos	13	1.59	0.691	169 ± 33°	0.471	11.9	7.60	0.473
	All	112	1.25	0.686	013 ± 34°	0.469	61.6	457.41	0.342
	Craters	13	1.15	0.919	054 ± 43°	0.613	17.5	4.27	0.464
Southern Trailing E17RegMap01	Pit	21	1.20	0.697	045 ± 45°	0.744	8.1	3.19	0.267
	Spot	4	0.92	0.601	092 ± 39°	0.493	14.0	2.35	0.626
	Dome	33	1.18	0.717	180 ± 40°	0.677	11.0	7.31	0.294
	Hybrid	25	1.51	0.645	016 ± 47°	0.86	13.9	1.46	0.254
	Chaos	134	2.06	0.652	077 ± 48°	0.821	33.3	9.02	0.202
	All	217	1.76	0.664	060 ± 50°	0.907	42.4	4.22	0.135
	Craters	1	1.4	0.905	065°	0	11.0	1.50	1.000

Table 2-2: Summary statistics and type of orientation distribution inferred for each combination of mapping area and microfeature types. The first line reports the p values returned by the Pearson χ^2 test, the Rayleigh test, and the Modified Kuiper test, in that order. Samples with $n \leq 8$, too small for statistical analysis, are indicated with —.

	Northern Leading	Northern Trailing	Southern Leading	Southern Trailing
Pit	0.006/0.000/0.000 $n = 10, V = 0.152$ Unimodal, $\theta = 140°$	0.000/0.000/0.000 $n = 120, V = 0.548$ Unimodal, $\theta = 51°$	0.000/0.000/0.000 $n = 67, V = 0.430$ Unimodal, $\theta = 16°$	0.700/0.203/0.421 $n = 21, V = 0.744$ Uniform
Spot	0.443/0.472/0.277 $n = 1, V = 0$ —	0.542/0.017/0.0336 $n = 24, V = 0.589$ Uniform	0.443/0.472/0.277 $n = 1, V = 0$ —	0.233/0.309/0.246 $n = 4, V = 0.493$ —
Dome	0.005/0.000/0.001 $n = 30, V = 0.479$ Unimodal, $\theta = 170°$	0.039/0.016/0.034 $n = 34, V = 0.642$ Unimodal, $\theta = 9°$	0.018/0.001/0.002 $n = 21, V = 0.418$ Unimodal, $\theta = 21°$	0.443/0.026/0.050 $n = 33, V = 0.677$ Uniform
Hybrid	0.000/0.000/0.000 $n = 25, V = 0.422$	0.001/0.003/0.017 $n = 39, V = 0.616$	0.815/0.435/0.766 $n = 10, V = 0.753$	0.240/0.482/0.367 $n = 25, V = 0.860$

	Unimodal, $\theta = 170°$	Unimodal, $\theta = 62°$	Uniform	Uniform
Chaos	0.236/0.086/0.084 $n = 209, V = 0.897$ Uniform	0.000/0.000/0.000 $n = 97, V = 0.452$ Unimodal, $\theta = 69°$	0.369/0.022/0.035 $n = 13, V = 0.471$ Uniform	0.000/0.011/0.001 $n = 134, V = 0.821$ Multimodal, $\theta \approx 80°, 55°$
All	0.017/0.004/0.004 $n = 275, V = 0.862$ Bimodal, $\theta \approx 55°, 160°$	0.000/0.000/0.000 $n = 314, V = 0.621$ Unimodal, $\theta = 60°$	0.000/0.000/0.000 $n = 112, V = 0.496$ Unimodal, $\theta = 13°$	0.005/0.121/0.010 $n = 217, V = 0.907$ Uniform
Crater	0.931/0.316/0.760 $n = 7, V = 0.629$ —	—/—/— $n = 0$, – –	0.095/0.118/0.042 $n = 13, V = 0.613$ Uniform	0.443/0.472/0.277 $n = 1, V = 0$ —

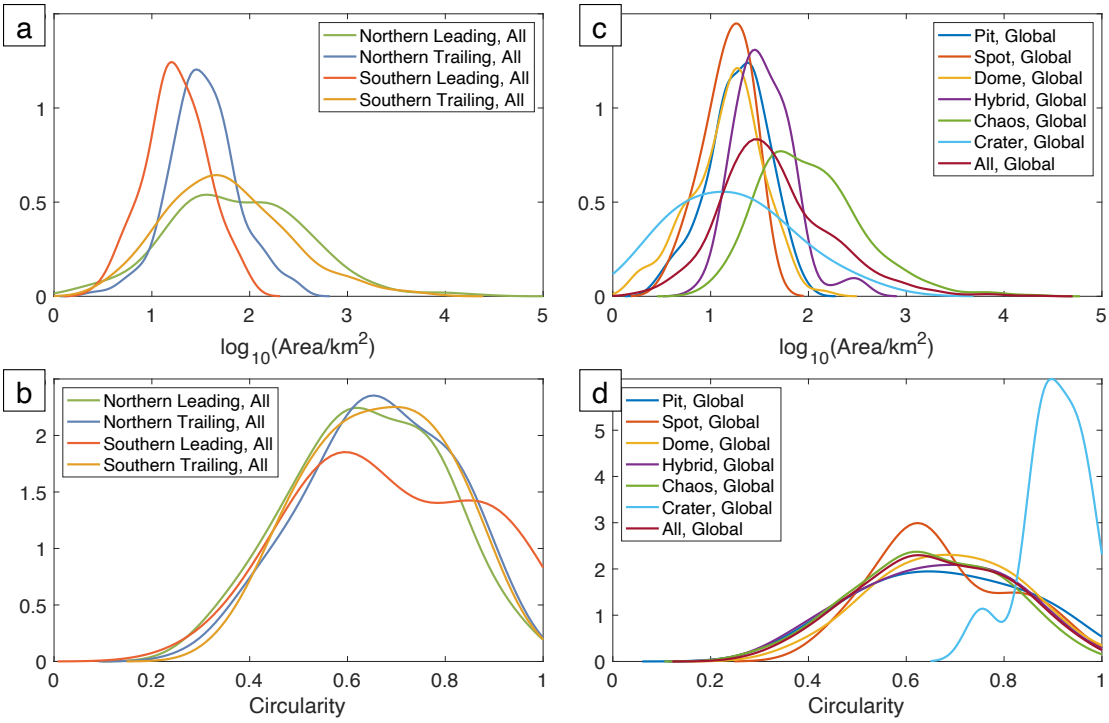


Figure 2-5: Probability Density Function of microfeature area (a, c) and circularity (b, d). The datasets on the left are separated by map area and show a systematic difference in microfeature size (a) but not circularity (b). The datasets on the right are separated by feature type and show systematic differences in size (c) but not in circularity (d), except for the almost perfectly circular mapped craters.

2.5.1 Size and elongation

Microfeature area is well described by a log-normal distribution (Figure 2.5a), except in the NLH. There, the distribution of log(area) has a flat top and may even be bimodal. These microfeatures are also larger than in other mapped regions. In contrast, the smallest microfeatures are found in the SLH. The geometric means of microfeature area differ by a factor of 4 between these regions, from 101.88 km2 in the NLH and 101.25 km2 in the SLH (Table 1). If the size distribution of microfeatures in the NLH is bimodal, one peak is close to the geometric mean area of

microfeature area in the STH, $10^{1.76}$ km^2, even though these areas are antipodal to one another. The second peak in the NLH microfeature area distribution is at ~$10^{2.2}$ km^2, implying that a sub-population of NLH microfeatures has the largest mean area documented in our study. (Table 1).

The size of various types of microfeatures presents systematic differences (Figure 2.5c). When examining all the mapped regions, chaos stands out as the largest microfeature, followed by hybrids, and finally, pits, spots, and domes sharing roughly similar size distributions. This relationship remains valid within individual map areas (Table 1). The size contrast between chaos and the other microfeature categories is greatest in the NLH, where chaos are more than ten times larger on average than pits, spots, and domes (Table 1). Interestingly, the size distribution of chaos, and to some extent hybrids, displays a distinct shoulder at larger sizes (Figure 2.5c), suggesting that there may be two populations. To fully interpret these observations, it is essential to deconvolve the effects of mapped area and microfeature type

Microfeature elongation is consistent across regions and microfeature types. The aspect ratio distribution presents a broad peak around a mean circularity ranging from 0.64 to 0.69. Only in the SLH do we observe a different distribution with the potential for two circularity peaks (Figure 2.5b). The distribution of spot circularity may also exhibit two peaks (Figure 2.5c), but the small number of these features makes it difficult to trust this observation. Note that the frequency of circularity close to 1 is very small (Figures 5b, d). For comparison, craters have a systematically higher elongation of ~0.9 (Figure 2.5d). This indicates that microfeatures are not circular shapes, and elongation is a characteristic of microfeature formation.

2.5.2 Microfeature orientation

The orientations of microfeatures in each mapped region are presented in Figure 2.6 in the form of rose diagrams. Because orientation is a non-directed quantity, the rose diagrams are symmetric around the origin. Rose diagrams for each combination of region and microfeature type are provided in the supporting information

Microfeatures in the NTH and STH regions exhibit similar average orientations of 59.5°. However, the orientation distributions differ between these two regions (Figure 2.6a, b). The circular variance is 0.62 in the NTH and 0.91 in the STH (Table 1), indicating a relatively narrow orientation distribution in the NTH compared to the STH. Microfeatures in the NLH and SLH have average orientations of 1.2° and 13.3°, respectively, with circular variance values of 0.86 and 0.50 (Figure 2.6c, d). The orientation values of microfeatures in the NLH are broadly distributed and may follow a bimodal distribution with peaks at 160° and 50° (Figure 2.6c), suggesting that the nearly north-south average orientation (Table 1) may not be meaningful. Conversely, the microfeature orientation in the SLH presents a strongly unimodal distribution with a mean near 170° (Figure 2.6d), confirming the observation from Figure 2.4d that microfeatures in the SLH are predominantly oriented in a direction close to north-south

2.5.3 Distribution of microfeature type

The 314 microfeatures in the NTH region are classified as 97 chaos, 120 pits, 34 domes, 24 spots, and 39 hybrids. In this region, chaos tends to be the largest feature type, with a geometric mean area of $10^{1.8\pm0.3}$ km^2. Hybrids, Pits, domes, and spots are smaller, with geometric mean areas of $10^{1.6\pm0.3}$, $10^{1.4\pm0.3}$, $10^{1.3\pm0.3}$, and

$10^{1.2\pm0.3}$ km^2, respectively (Table 1). Each feature type presents similar average circularities ranging from 0.65 (domes and chaos) to 0.69 (spots), keeping with the regional trends described above. The orientation distribution of each feature type is well concentrated around its mean, with circular variance values ranging from 0.45 for chaos to 0.64 for domes. Chaos, pits, and domes all seem to exhibit narrow unimodal orientation distributions. In contrast, the orientation distribution of spots in the NTH may be bimodal, with peaks around 70° and 110°. This region is the only one with a significant population of spots.

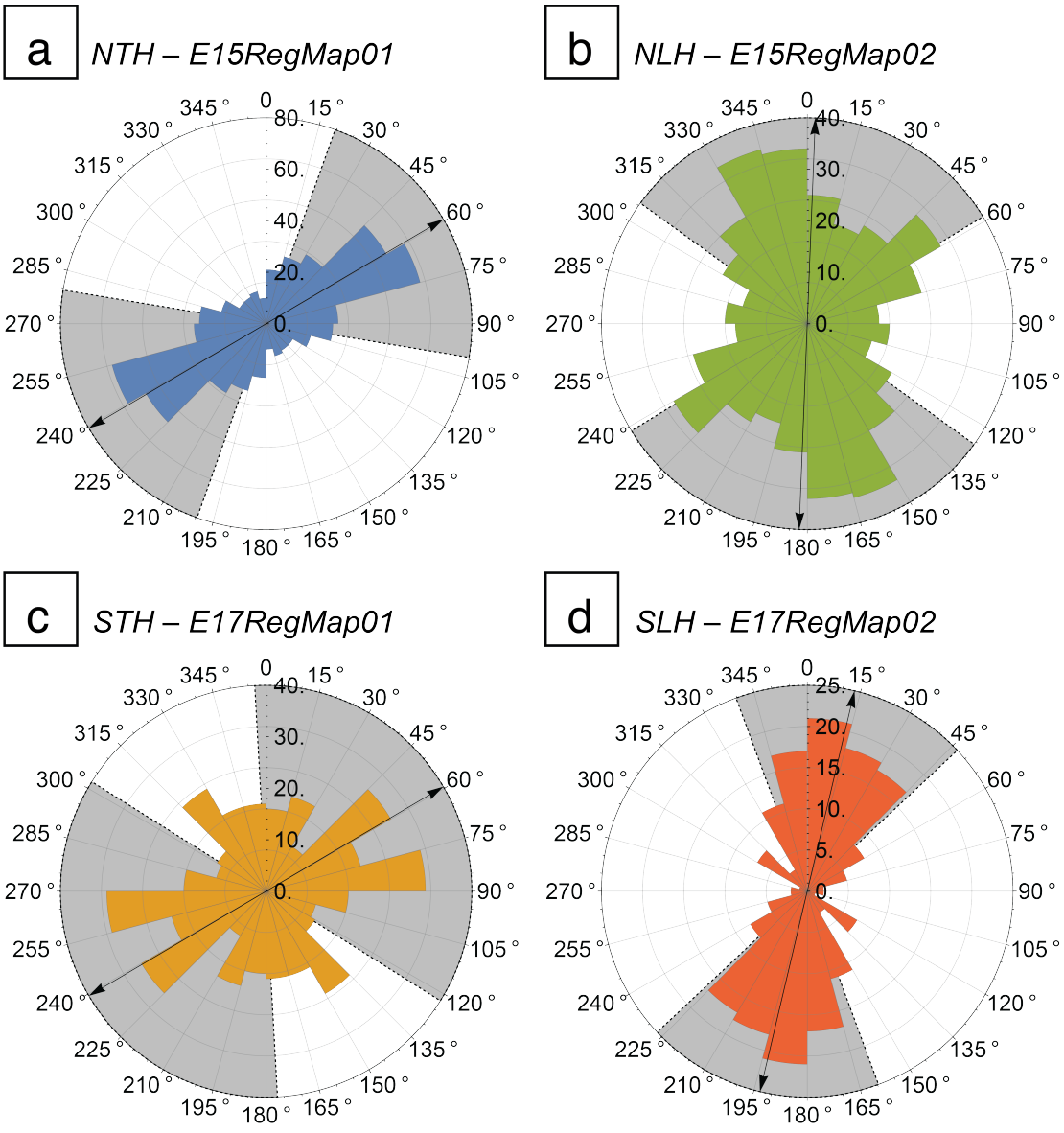


Figure 2-6: Rose diagrams illustrate the orientation of all microfeatures in each of the four regions mapped by Noviello et al. (2019a): (a) Northern Trailing Hemisphere, (b) Southern Trailing Hemisphere, (c) Northern Leading Hemisphere, and (d) Southern Leading Hemisphere. The arrows point in the direction of the mean orientation. The radial scale bar corresponds to microfeature frequency in each bin. The grey area represents the spread of orientations around the mean (see section

2.3.2). Orientation is measured from 0° to 180°, and the rose diagrams are mirrored to emphasize the 180° ambiguity in non-directed axial data such as orientation.

A total of 134 chaos, 21 pits, 33 domes, 4 spots, and 25 hybrids were identified in the STH. In this region, the features with the largest geometric mean area are chaos, with $10^{2.1\pm0.5}$ km^2. Their distribution hints at a second population of even larger chaos with a geometric mean area of about 10^3 km^2. Spots were the smallest, with a geometric mean area of $10^{0.92\pm0.3}$ km^2. Pits and domes present similar geometric mean area values, $10^{1.2\pm0.4}$ km^2, respectively. However, the distribution of pit areas peaks at a higher value and is skewed towards smaller areas, while the opposite is true for the distribution of dome areas. The geometric mean area of hybrids is $10^{1.5\pm 0.3}$ km^2, intermediate between those of pits and chaos. Domes are the least elongated features in this region, with an circularity of 0.72 ± 0.1. The circularity of the other feature types ranges from a low 0.60 for spots to more typical 0.5 for hybrids and chaos and 0.70 for pits. The various microfeature types are oriented toward widely different directions in the STH region: 77°, 45°, 180°, 92°, and 16° for chaos, pits, domes, spots, and hybrids, respectively. The circular variance for these orientation distributions is also large. Hybrids exhibit the highest circular variance at 0.86, but their orientation distribution appears bimodal, with peaks towards 15° and 95°. The orientation distribution of chaos also exhibits a large circular variance, 0.82, but does not appear bimodal. The larger number of chaos in this region compared to hybrids may reveal a larger number of preferred directions if the numerous small peaks in their orientation distribution are significant. The orientation distributions of pits and domes present similar circular variance values at

0.74 and 0.68, respectively. Both orientation distributions appear to be unimodal. Spots have too small of a sample size to discuss orientation distribution trends.

The NLH region contains the largest population of chaos microfeatures, with a total of 209, constituting 76% of all the microfeatures identified in this region. Conversely, it has the fewest number of pits, with only 10. 30 domes, 25 hybrids, and 1 spot were also identified in the NLH. Chaos in this region are also the largest found in this study, with a geometric mean area of $10^{2.11\pm0.6}$ km^2, while the pits are the smallest, with a geometric mean area of $10^{0.82\pm0.24}$ km^2. The circularity of these features is similar to that observed in the regions mentioned above, ranging from 0.64 to 0.68, while the circularity of the only spot in the region is 0.86. Unlike the NTH and STH described above, several microfeature types are oriented in a SE-NW direction. Pits, domes, and hybrids have mean orientations of 140°, 169°, and 170°, respectively. The pits in this region exhibit the most consistent orientation of all microfeature sets, with a circular variance of just 0.15. This could be due to the small number of pits. The orientations of domes and hybrids are also well concentrated around their means, with similar circular variance values of 0.48 and 0.42, respectively. The orientation distributions likewise appear unimodal for both feature types. The average orientation of chaos in this region is 33.2°, with a high circular variance value of 0.90. This feature type presents the broadest orientation distribution among all the different feature classes studied here.

The SLH contains the fewest microfeatures, with only 13 chaos, 67 pits, 21 domes, 1 spot, and 10 hybrids. With nearly 60% of the microfeatures being pits and less than 12% being chaos, the distribution of microstructure types in the SLH

significantly differs from that in other regions. Nevertheless, chaos are, on average, the largest microfeatures, as observed in other regions, followed by hybrids, then domes and pits, and finally spots. Still, the chaos microfeatures in this region have the smallest geometric mean area, $10^{1.58\pm0.3}$ km^2, of the four mapped regions. Microfeatures in the SLH are slightly more circular than those in other regions. Domes display the highest circularity, with a mean of 0.76. Chaos, pits, and hybrids exhibit similar mean circularities ranging from 0.66 to 0.68. The one spot in the region has an circularity of 0.50. Chaos and hybrids are oriented towards similar mean directions of 169° and 163 °, respectively, while domes and pits have similar mean orientations of 22° and 16°, respectively. The orientation distributions of chaos, pits, and domes are strongly concentrated around the mean, with circular variances ranging from 0.42 to 0.47. These distributions appear unimodal, with few measurements markedly different from the average orientation. The orientations of hybrids are more broadly distributed, showing the largest circular variance among all SLH microfeature types at 0.77, and presenting a rather ill-defined unimodal distribution. This is likely due to the small sample size. Spots were excluded from this analysis as only one was identified.

2.5.4 Statistical Test by Region

Statistical tests help build confidence in the interpretations of the previously described orientation distributions. Here, we employ three statistical tests: the Pearson χ^2 test, the Rayleigh test, and the Modified Kuiper Test. These tests are designed to assess whether an orientation distribution is uniform and whether the apparent concentrations of orientation data are the result of noise and limited sampling.

However, the different designs of these tests make them sensitive to different aspects of the sample. In all three cases, we determine the probability p that a distribution is uniform, as described in Section 2. We consider that the assumption of uniformity can be rejected if $p \leq 0.05$. This insight, combined with the circular variance V, helps understand whether a distribution is unimodal or multimodal. A unimodal distribution would pass the tests with small p and V values, while a multimodal distribution would appear broadly distributed but non-uniform. That is, it would have a low p but high V. Uniform distributions have high p and V. Table 2 compiles the p and V values for every combination of microfeature type and region and indicates the implied orientation distribution.

In the NTH region, the Pearson χ^2 of all the microfeatures, regardless of type, is 115, high enough to reject the hypothesis of uniformity with $p = 0$. The Rayleigh and Modified Kuiper tests reach the same conclusion with $S^*_{mod} = 90.4$ and $V^*_n = 0.25$. Given also that the circular variance is 0.621, there is strong evidence that the distribution of microfeatures in the NTH is unimodal, with a significant preferred orientation of 60° (Figure 2.6a).

The microfeature orientation distribution in the STH region has the largest circular variance found in our study, $V = 0.91$. Accordingly, Figure 2.6b exhibits a broad orientation distribution without a well-defined peak. The Pearson χ^2 test and modified Kuiper tests reject the assumption of uniformity with $p < 0.01$. However, the test statistic in the Rayleigh test is $S^*_{mod} = 4.21$, lower than the critical value of 5.991. Therefore, the probability that the orientation distribution is uniform is $p{\sim}0.11$. and cannot be rejected. It is possible that the orientation distribution (Figure

2.6b) is composed of four or five samples with different preferred orientations, which would explain the Pearson χ^2 and Modified Kuiper test results, but we cannot be certain of this explanation. We conclude that there is no reliable evidence against this dataset being uniformly distributed, and the peaks in the orientation distribution are not statistically significant.

The microfeature orientation distribution in the NLH region also has a large circular variance, $V = 0.63$. The Pearson χ^2 value for this dataset is 23.2, large enough to reject uniformity with $p = 0.017$ The Rayleigh test and Modified Kuiper test are even more conclusive, with $p{\sim}0.004\%$ (test statistics $S^*_{mod} = 11.0$ and $V^*_n = 0.126$). Thus, in this region, we can reject the hypothesis that microfeature orientation is uniformly distributed despite the high variance and conclude that the microfeature orientation distribution in the NLH is likely multimodal. Indeed, the distribution exhibits prominent peaks around 55° and 160° (Figure 2.5c).

In the SLH region, the Peason χ^2 is 61.6, the Rayleigh test statistic is $S^*_{mod} = 57.4$ and the Modified Kuiper test statistic is $V^*_n = 0.342$. These values are large enough that all three tests reject the hypothesis of uniformity with $p < 10^{-8}$. This is consistent with the low variance $V = 0.469$ of this sample. The microfeature orientations in the SLH are strongly unimodal, tightly concentrated around a mean orientation of 13° (Figure 2.6d).

2.5.5 Statistical Results by Feature Type

To further understand the microfeature dataset, we will now consider each type of microfeature separately in all four mapped regions. In the cases where microfeature orientation is strongly unimodal (NTH and SLH), it is still possible that

some microfeatures, particularly those that are less common in these regions, may be associated with a different type of distribution. In the other regions, it is important to determine whether the variability in the orientation data could be attributed to the superposition of several samples, each confined to a specific microfeature type and associated with a clearly defined preferred orientation. Figures 7 to 10 present rose diagrams of microfeature orientations separated by category in the NLH, NTH, SLH, and STH. The results of statistical tests are presented in Table 2 and discussed below.

2.5.6 Chaos

Chaos are the largest and most complex microfeatures in each region. They are also the most numerous type of microfeature in the NLH and STH regions. The evidence for a consistent chaos microfeature orientation is strongest in the STH region, where our statistical tests reject the assumption of uniformity with $p < 0.011$. Chaos orientation is nevertheless broadly distributed, with $V = 0.821$. This implies that the STH chaos orientation is multimodal and the mean orientation of the sample is not significant. The peaks in the chaos orientation distribution at 50° and 85° may be significant (Figure 2.10e). These peaks are also observed in the orientation distribution of all STH microfeatures (Figure 2.6b), 60% of which are the chaos just discussed.

The next largest number of chaos is found in the NLH. Their orientation distribution has a high circular variance value of 0.897. This data does not pass either of our three tests, with the higher p value, 0.236%, returned by the Pearson χ^2 test. The other tests give p between 0.08 and 0.09, presenting little evidence against

uniformity (Figure 2.7e). Therefore, we consider that chaos orientation is uniformly distributed in the NLH.

By contrast, chaos in the NTH display a strong preferred orientation (Figure 2.8e). The circular variance is $V = 0.452$ and all three tests reject the hypothesis of uniformity with $p < 10^{-12}$. The fairly large number of chaos microfeatures in this region show a strong preferred orientation towards 69°.

Finally, the orientation of chaos in the SLH (Figure 2.9e)fails the Pearson χ^2 with $p{\sim}0.369$. The other two tests present strong evidence against uniformity, with $p{\sim}0.022$ for the Rayleigh test and $p{\sim}0.035$ for the Modified Kuiper test, and the circular variance is fairly low, at 0.469. These inconsistent results may be ascribed to the small number of chaos in that region, 13. Still, because of the Pearson χ^2 results, we cannot reject the null hypothesis of uniformity in this region.

2.5.7 Pits

Pits are the most abundant microfeature in our dataset after chaos. They represent the most common type of microfeature in the NTH and SLH, but are less frequent in the STH, with only 10 identified in the NLH

The evidence against uniformity of pit orientation in the NTH and SLH is very strong. Their orientation distribution passed all three statistical tests with $p < 10^{-4}$. The small circular variance in these two regions implies that their orientation distribution is strongly unimodal, and the average orientations of 51° and 16° in these regions are significant (Figures 8c and 9c).

The NLH region produces similar statistical results but with a slightly higher p value of 0.006 obtained by the Pearson χ^2 test. The very low variance of 0.152 in

this region confirms that the orientation distribution is unimodal, with a strongly preferred direction of 140° (Figure 2.7c). However, one must remember that only 10 pits are found in this region, hardly more than the 8 necessary to conduct these statistical analyses.

The STH contains about twice as many pits as the NLH, but this is still a small number. Here, however, the statistical tests agree that they cannot reject the hypothesis of uniformity. The lowest p value, obtained by the Railegh test, is still 0.203, and the circular variance is 0.744. Thus, the pits in STH appear uniformly oriented (Figure 2.10c).

2.5.8 Domes

Each region has a similar number of domes, between 21 and 34. In the leading hemisphere, dome orientation data from both the northern and southern regions has low variance of 0.479 and 0.418, respectively, and pass Rayleigh tests and modified Kuiper tests with $p \lesssim 0.002$, suggesting a strongly unimodal orientation distribution. The Pearson χ^2 supports this conclusion, even though its p values are slightly higher, 0.005 in the NLH and 0.018 in the SLH. Still, all analyses support the conclusion that the domes in the NLH and SLH have significant preferred orientations at 170° and 22°, respectively (Figures 7b and 9b).

Statistical tests also consistently reject the null hypothesis of uniformity in the NTH, with $p \leq 0.04$. The circular variance is slightly higher in this region, $V = 0.642$, but not as high as in clearly multimodal cases. Therefore, we consider that the NTH domes are preferentially oriented towards 9°, although there may be a small population of domes in that region oriented towards 110° (Figure 2.8b).

The dome orientation distribution in STH has the largest circular variance with a value of 0.68. The Rayleigh test and Modified Kuiper tests reject the null hypothesis of uniformity with $p = 0.026$ and 0.050, respectively. However, the Pearson χ^2 test fails to reject this hypothesis, with $p = 0.443$. Therefore, we consider that domes are uniformly oriented in the STH (Figure 2.10b).

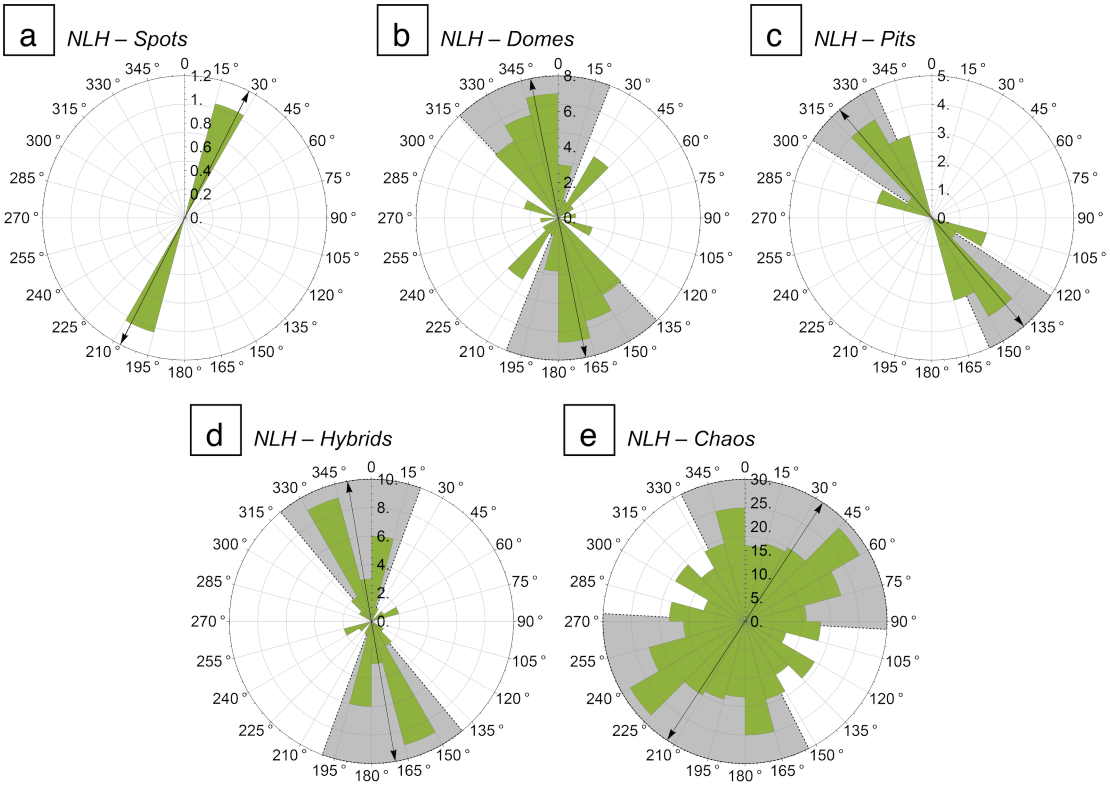


Figure 2-7: Rose diagram of microfeature orientation in the NLH separated by microfeature category. The labels are as in Figure 2-6.

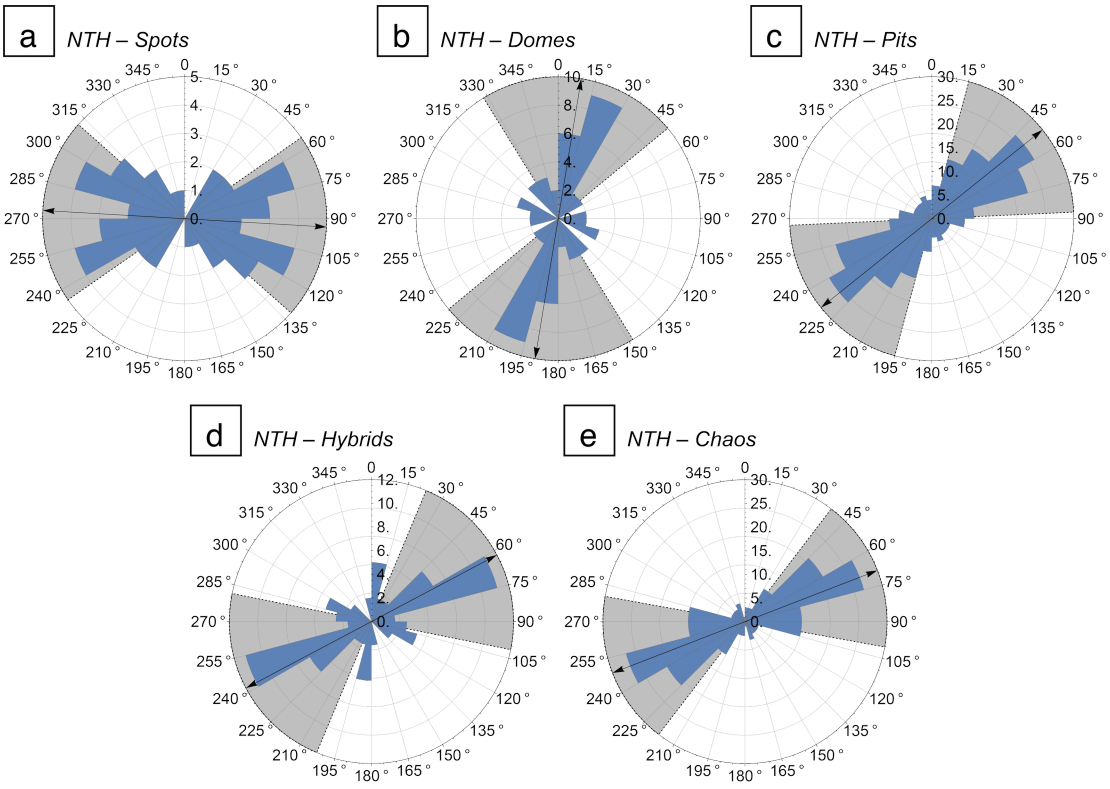


Figure 2-8: Rose diagram of microfeature orientation in the NTH separated by microfeature category. The labels are as in Figure 2.6.

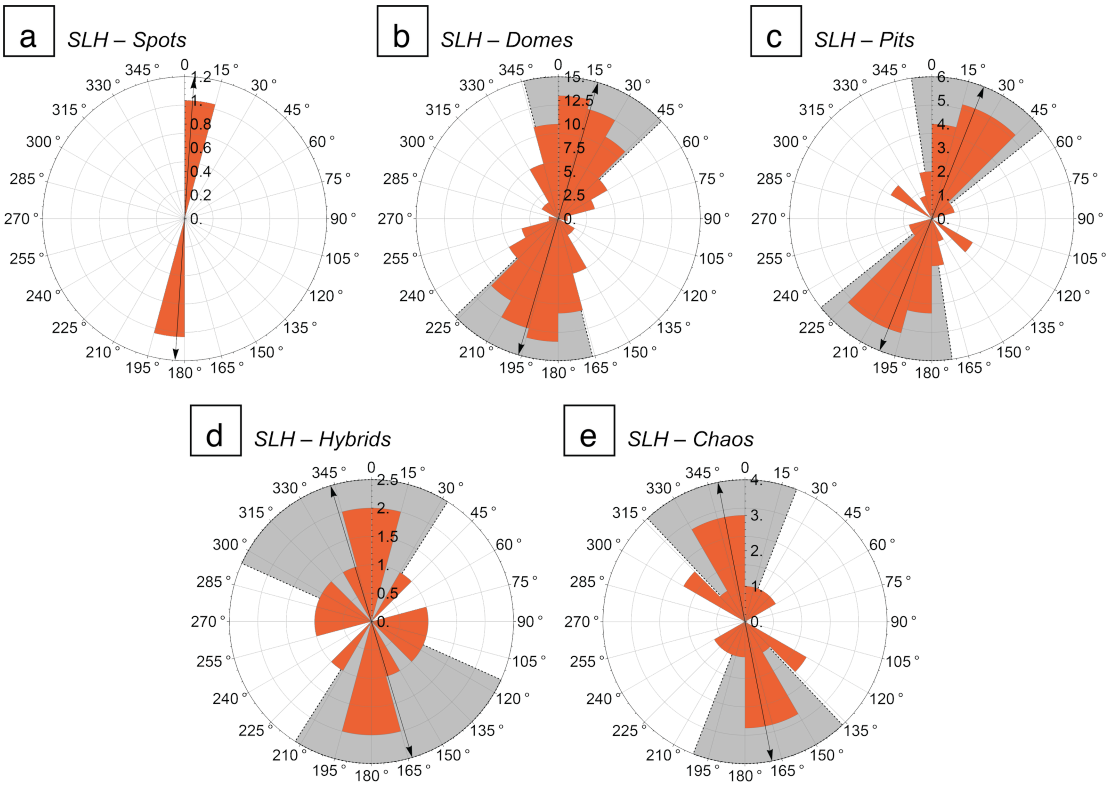


Figure 2-9: Rose diagram of microfeature orientation in the SLH separated by microfeature category. The labels are as in Figure 2.6.

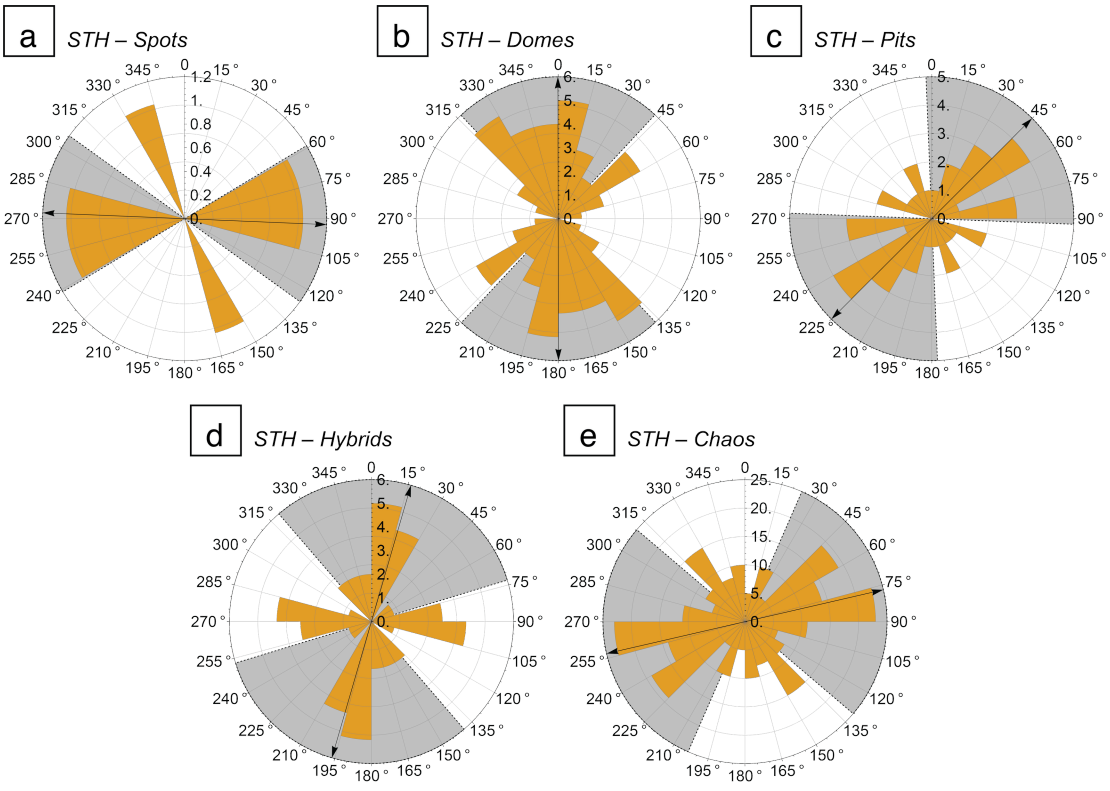


Figure 2-10: Rose diagram of microfeature orientation in the STH separated by microfeature category. The labels are as in Figure 2.6.

2.5.9 Hybrids

The NTH contains the highest number of hybrid microfeatures, 39. Their orientation data passes the Pearson χ^2 and Rayleigh tests with $p < 0.003$ and the Modified Kuiper test with higher lower p value of 0.017. Therefore, all three tests reject the null hypothesis of uniformity. The circular variance in this sample is $V = 0.616$, indicating that there may be a small number of hybrid microfeatures oriented in a different direction than the sample as a whole. However, we cannot identify in a rose diagram what this direction may be. Therefore, we conclude that hybrid microfeatures in the NTH are preferentially oriented towards 62° (Figure 2.8d).

The NLH and the STH have the same number of hybrid microfeatures, 25. However, their orientation distributions are markedly different. The NLH sample is associated with a small circular variance of $V = 0.422$, and all three statistical tests reject the null hypothesis of uniformity with $p > 0.0002$ Therefore, we conclude that hybrid microfeatures in the NLH display a strong preferred orientation towards 170° (Figure 2.7d).

In contrast, the STH sample has a high circular variance of 0.860, and all three statistics tests fail to reject the null hypothesis of uniformity, with the lowest p value, 0.240, returned by the Pearson χ^2 test. A rose diagram of this sample suggests that there may be two preferred orientations in this dataset, almost perpendicular to one another (Figure 2.10d). Our statistical tests, however, do not support this interpretation, possibly because of the relatively small size of this sample. Therefore, we conclude that there is no robust evidence against the STH hybrid microfeatures being uniformly oriented.

Finally, there are only 10 hybrid microfeatures in the SLH, fewer than in other regions. Their circular variance is a high $V = 0.753$, and none of our tests rejects the null hypothesis of uniformity, with the lowest p value, 0.435 provided by the Rayleigh test. We conclude that there is no evidence against hybrid microfeatures in the SLH being uniformly distributed (Figure 2.9d).

2.5.10 Spots

Spots are the rarest type of microfeatures, with only 1 identified in each of the NLH and SLH and 4 in the STH. Statistical analyses can only be conducted in the NTH region, where there are 24 spots. The circular variance of this sample is $V =$

0.59, indicating a relatively tight distribution. The Rayleigh and Modified Kuiper tests reject the null hypothesis of uniformity with $p = 0.017$ and 0.034, respectively. However, the Pearson χ^2 test fails to reject the null hypothesis of uniformity with p larger than 0.542. After examining the rose diagram, it appears that the orientation of NTH spots may be bimodal, with peaks approximately at 70° and 110° (Figure 2.8a). However, the ambiguous statistical test results, possibly related to the small spot population in this region, prevent a confident interpretation of these findings. We must conclude that spots in the NTH are uniformly distributed.

2.5.11 Craters

For comparison, we conducted similar analyses on the craters mapped in these regions. The number of craters in NLH and STH, 7, and 1, are too small for these analyses, and no crater was mapped in NTH. The 13 craters in SLH appear randomly oriented, with only the Modified Kuiper test returning a p value less than 0.005. The higher p values from the Pearson χ^2 and Rayleigh tests, 0.095 and 0.118, respectively, are too high to reject the null hypothesis of uniformity. As may be expected for the consequences of high-energy impact, craters are circular (Figure 2.5) and uniformly oriented.

2.5.12 The effect of nearly circular features

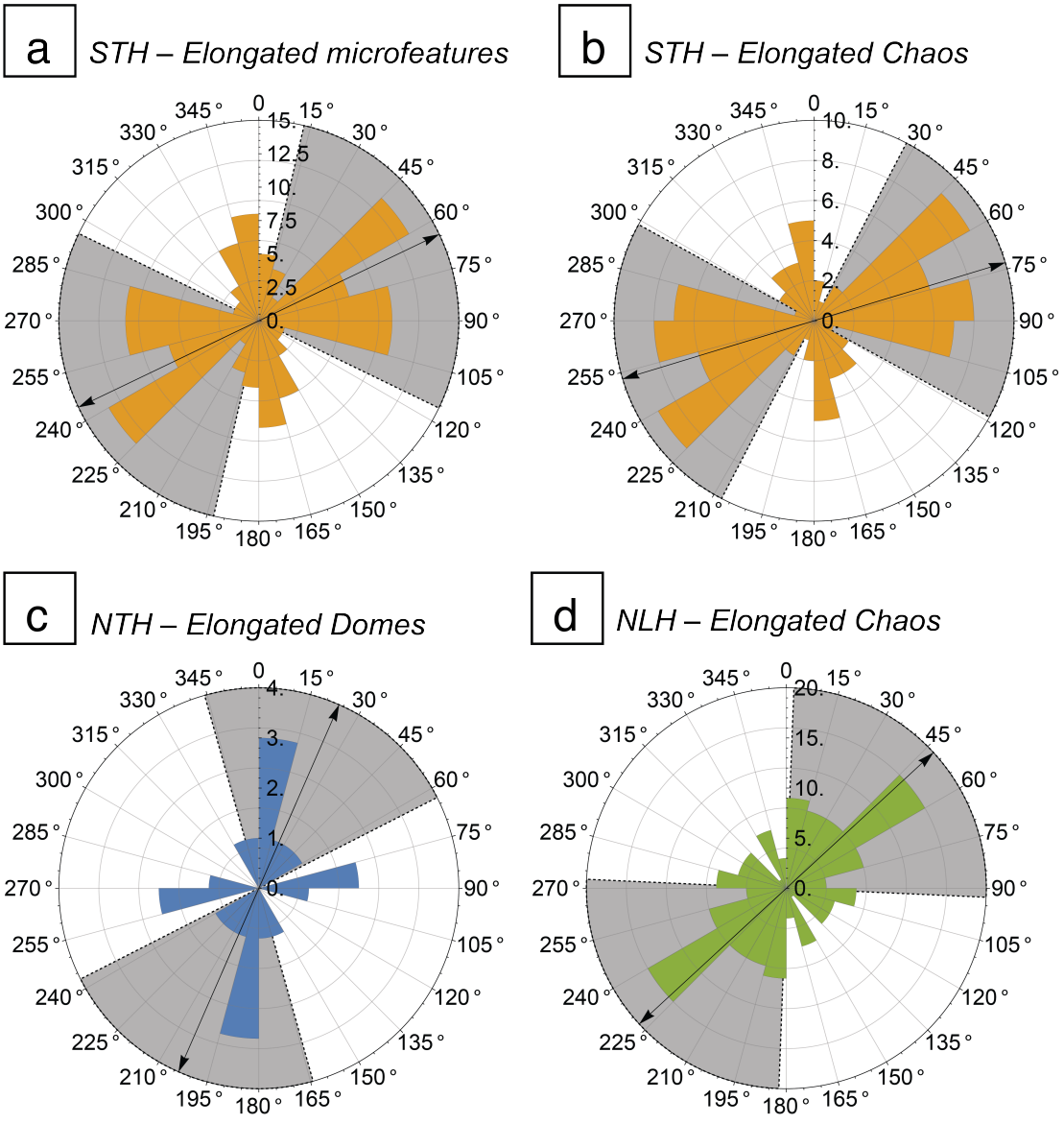


Figure 2-11: Rose Diagrams of microfeatures with elongation values less than 0.6. The rose diagrams show (a) elongated micro features in the southern trailing hemisphere, (b) elongated chaos in the southern trailing hemisphere, (c) elongated domes in the northern trailing hemisphere, and (c) elongated chaos in the northern leading hemisphere.

It should be expected that the orientation of nearly circular microfeatures is more uncertain than that of highly elongated ones. This uncertainty may mask some actual preferred orientation in at least some of the samples presented above. Therefore, it is important to evaluate whether distributions described as uniform retain this character when only highly elongated microfeatures are considered. Conversely, spurious peaks in the orientation direction may vanish or change with smaller samples. To evaluate these possibilities, we repeated all the analyses above considering only microfeatures with a circularity of less than 0.6. This limit was arbitrarily chosen to balance a focus on highly elongated features while retaining samples large enough for statistical analysis. This choice removes about two-thirds of the microfeatures dataset.

In the NTH, there are not enough highly elongated spots to conduct our statistical analyses. The orientation distributions of pits, hybrids, chaos, and all microfeatures remain strongly unimodal, with a change in the mean angle of less than 2° when considering only highly elongated microfeatures. However, the distribution of dome orientations can no longer be differentiated from a uniform distribution, with p values of 0.555, 0.159, and 0.305 for the Pearson χ^2, Rayleigh, and modified Kuiper tests. Their orientation distribution may be bimodal but cannot be differentiated from a uniform distribution with only 11 measurements. The original mean orientation of NTH domes, 9°, is one of the peaks in the orientation distribution of highly elongated domes, Figure 2.11c.

In the STH, the number of highly elongated pits, spots, domes, and hybrid microfeatures is too small to perform statistical analyses. 49 highly elongated chaos

microfeatures are found in this region, Figure 2.11b. Their orientation distribution can be distinguished from a uniform distribution, with the highest p value, 0.012, returned by the Rayleigh test. This result is similar to that obtained using all chaos in the region. The distribution still appears bimodal, and the largest peak in the orientation distribution, at ~55°, appears in both samples. However, the secondary peak is found at ~175°, not ~80°, when considering all STH chaos. Thus, we consider that the ~55° direction is significant but refrain from interpreting the other possible peaks in the distribution. The orientation distribution of all highly elongated microfeatures in the STH map can be distinguished from a uniform distribution, with the highest p value, 0.035, returned by the Rayleigh test, Figure 2.11a. This result contrasts with the conclusion obtained when considering all microfeatures in the STH, regardless of elongation. This apparently uniform distribution may be explained by a multimodal distribution of highly elongated microfeatures, dominantly chaos, with a preferred orientation towards ~55°, a secondary preferred orientation towards ~170°, and a set of less elongated microfeatures whose orientations may be taken from a uniform distribution (Figure 2.8).

In the NLH, the strong preferred orientation of domes and hybrid microfeatures is confirmed when considering only highly elongated microfeatures, with a change in mean orientation of less than 10°. There are not enough highly elongated pits and spots in this region to conduct statistical analyses. Selecting only highly elongated microfeatures changes the orientation distribution of chaos in this region, Figure 2.11d. Instead of a uniform distribution, we find that highly elongated microchaos have a strong preferred orientation towards 47°, with the highest p value,

0.005, returned by the Pearson χ^2 test. The orientation distribution of all NHL chaos shows a peak in that direction but with a background of uniformly oriented, less elongated chaos that dominates the statistical results. A similar orientation was identified as one of the peaks in the orientation distribution of all NLH microfeatures. Therefore, that distribution is composed of a set of highly elongated oriented chaos preferentially orientated towards ~50°, pits, domes, and hybrid microfeatures oriented preferentially towards 140° to 180°, and a set of less elongated chaos with uniform orientation. The orientation distribution of highly elongated microfeatures of all types in the NLH prominently shows these orientations.

The SLH contains only 39 highly elongated microfeatures out of an initial 112 mapped microfeatures. Statistical analyses are possible only if taking all types of microstructure together or considering highly elongated pits, which number 28. Both samples are associated with orientation distributions that can be distinguished from a uniform distribution, with $p < 10^{-5}$in all three tests. The average orientation of these samples differs by less than 6° from those of the equivalent samples regardless of elongation. However, the circular variances change from ~0.4 to ~0.2 when restricting the samples to the most elongated features, increasing confidence in the inferred preferred directions.

2.5.13 Orientation by Latitude

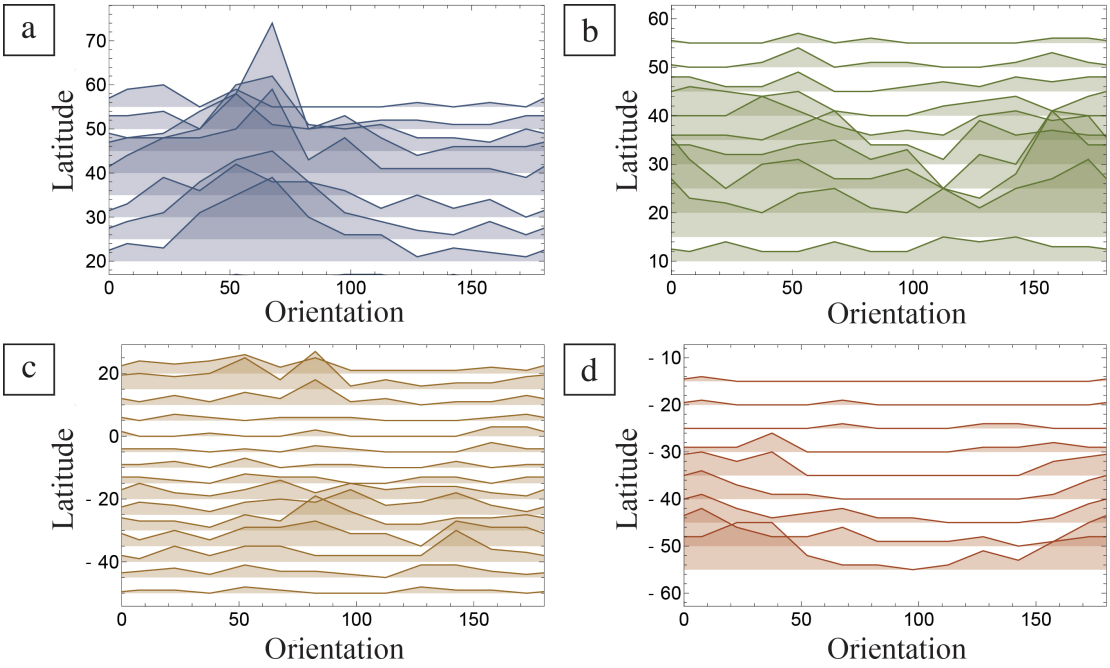


Figure 2-12: Histograms of the orientation of features in (a) NTH, (b) STH, (c) NLH, and (d) SLH. Each histogram represents a 10° latitude bin, whose range overlaps with the histograms above and below by 5°. We choose to overlap the histogram latitude bins to avoid creating artificial breaks in the data.

The mapped regions cover a wide range of latitudes, making it possible that some variation in orientation measurements may be linked to the systematic change in azimuth as latitude along a great circle. To assess this possibility, we present histograms of microfeature orientation in 10° latitude bins in Figure 2.12. In this analysis, we do not differentiate between microfeature types or limit the dataset to highly elongated microfeatures, as this would significantly decrease the number of available measurements

Microfeatures in the NTH region exhibit a strong preferred orientation of 60° (Figure 2.5a). Therefore, it is not surprising to observe that orientation across all latitude bins (Figure 2.12a). The orientation peak broadens as we approach the equator.

The northern end of the STL map overlaps with the southern end of the NTH map. Thus, we see that the preferred 60° orientation peak continues in the STH before vanishing near the equator (Figure 2.12b). A smaller orientation peak near 180° appears near the equator and can be followed to approximately 20°S, with a progressive rotation towards 150°. This cannot correspond to a great circle, as the north-south direction is crossed away from the equator. Microfeature orientation south of 20°S is broadly distributed with several small peaks. The different microfeature subsets identified in the STL based on elongation and orientation may have limited geographical extents.

The orientation distribution in the NLH is broad at all latitudes (Figure 2.12c). The dominant orientations at 55° and 170° are observed north of 20°N and around 30°N, respectively. Identifying these orientations from the latitude-binned dataset would be challenging without the assistance of the statistical analyses conducted earlier.

Microchaos orientation in the SLH exhibits a strong preferred orientation towards 15° (Figure 2.12d). We observed this feature at all latitudes where a relatively large number of microfeatures are present, south of 30°S. The width of the peak is approximately 60°, which explains our initial observation that SLH microfeatures are typically oriented in the N-S direction.

2.6 Discussion

From our study of microfeature morphology, we come to three conclusions: (1) microfeatures have preferred orientations, (2) different types of microfeatures may have different episodes of formation, and (3) orientation distributions may show potential stress rotation as features evolve through different stages of formation. We will address each conclusion in order.

2.6.1 Origin of elongation

Microfeatures are usually described as having circular shapes. While this characterization captures the general appearance of microfeatures, we showed that the circularity of microfeatures is systematically different from 1, suggesting that a degree of elongation is a fundamental characteristic of these geological objects. In this respect, they differ from impact craters (Figure 2.5d). This elongation may arise from strain elongating the microfeature in one direction (Figure 2.13a), stress facilitating elongation of an underlying diapir or cryomagma body to elongate in the direction of the most compressive stress (Figure 2.13b), or preexisting structures in the ice crust, such as a crack at depth (Figure 2.13c) or a valley near the surface (Figure 2.13d), facilitating the emplacement of microfeatures along that structure.

In the first case, elongation would develop after the emplacement of the microfeature. This could be reconciled with the near absence of nearly circular microfeatures only if all microfeatures are emplaced before a global strain episode. The position of microfeatures and large chaos in the most recent chronostratigraphic period of Europa (Leonard et al., 2024) makes this explanation unlikely. The last explanation requires that microfeatures are emplaced as a surface flow, which is difficult to envision for pits and domes. Although it is possible that different kinds of

microfeatures have different origins, elongation at depth during the emplacement of a mush or liquid body of water or the rise of a warm ice diapir seems most compatible with the range of morphologies observed. This suggests that microfeature elongation is linked to a stress field. It could be the stress field at the time of microfeature emplacement (Figure 2.13b) or an earlier stress or deformation episode that damaged the ice crust preferentially in some directions (Figure 2.13c). A cursory examination of Galileo images fails to detect cracks or ridges aligning with microfeatures in the direction of their long axis. Therefore, we favor elongation of the conduit at depth in response to the stress at the time of emplacement (Figure 2.13b). In either case, a regionally consistent microfeature elongation is related to a regionally consistent stress field.

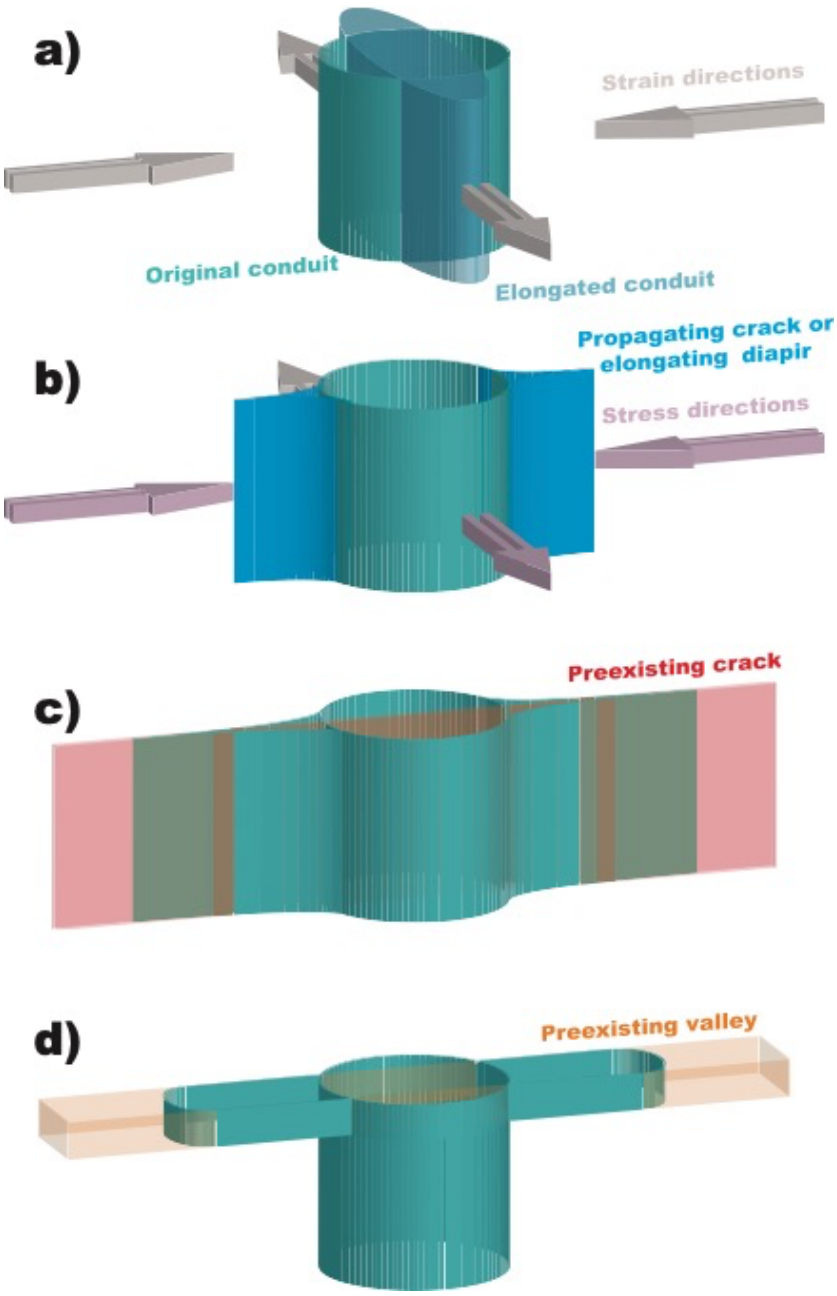


Figure 2-13: Potential origins of microfeature elongation. The microfeature is envisioned as the surface manifestation of a cylindrical, shown in teal, conduit containing either warm ice, liquid water, or a slurry. In (a), the conduit and microfeature become elongated after emplacement due to distributed strain in the ice crust. In (b), the original conduit elongates as it is influenced by the ambient stress

field, either through the propagation of a crack or processes similar to borehole breakouts. In (c), the conduit utilizes preexisting cracks in the ice crust (red), leading the microfeature to follow that elongation. In (d), elongation occurs only at the surface (yellow), where the microfeature extends along a preexisting topographic trough or valley.

2.6.2 Existence of preferred orientations

The statistical tests described above evaluate quantitatively whether an orientation distribution can be confidently interpreted as having one or several preferred orientations. The microfeatures in all the regions except STH exhibit a significant preferred orientation. In STL, the seemingly uniform distribution of microfeature orientation can be understood as a population of uniformly oriented, poorly elongated features and a set of highly elongated features with a preferred orientation. Chaos in the NLH also contains a set of highly elongated features with a preferred orientation and a set of less elongated, uniformly oriented chaos.

All feature types except spots display a significant preferred orientation in at least one of the mapped regions considered here. This result differs from what Culha and Manga (2016) reported. They concluded that only pits had a preferred orientation. However, their analysis would be sensitive to a globally consistent orientation, as they combined features mapped in seven regions spread globally on Europa. The preferred orientations we find vary from one mapped region to another, indicating that preferred orientations are regional rather than global in scale. Additionally, Culha and Manga (2016) used a one-sample t-test, which relies on the assumption that the data is normally distributed and does not apply to circular data. The statistical tests

we selected are designed to handle axial data and test for deviation from a uniform distribution without specifying an alternative distribution. Therefore, our analyses are better suited for detecting preferred orientations.

Previous studies have discussed the orientation of ridges (Geissler et al., 1998; Rhoden et al., 2021; Rhoden & Hurford, 2013), small depressions (Schenk et al., 2008), strike-slip faults (Hoppa, 1999; Rhoden et al., 2011), and cracks (Sarid et al., 2006). Systematic variations in these orientations have been interpreted as evidence for the non-synchronous rotation of Europa's ice shell and true polar wander. In contrast, we find no evidence for a systematic variation of microfeature orientation with latitude, which would be expected if true polar wander altered microfeature orientation. Our orientations also do not follow the stress patterns associated with non-synchronous rotation. Thus, we conclude that neither non-synchronous rotation nor true polar wander is responsible for the preferred orientation of microfeatures. Instead, microfeature orientation may reflect a combination of global and local stresses. Band formation (Howell & Pappalardo, 2018), chaos formation (Schmidt et al., 2011), ice convection (Mitri & Showman, 2005; Allu Peddinti & McNamara, 2019), tectonics (Kalousová et al., 2014), or ocean circulation (Goodman et al., 2004; Kang, 2022; Kvorka & Čadek, 2024) may locally modify the strength of the ice shell so that global stresses from, e.g., ice shell thickening (Manga & Wang, 2007), cease to be isotropic.

2.6.3 Formation episodes

In many regions, the orientation distribution is tightly concentrated around its mean value, indicating strongly that a single population of these microfeatures exists

on that map. This is particularly true for the NTH, where only the spots form a distribution that cannot be confidently differentiated from uniform (Figure 2.8a). Spots in this region may present two orientations, although this cannot be ascertained from our tests: the p values from the Rayleigh and Modified Kuiper tests are 0.014 and 0.038, suggesting variation from uniformity, but that from the Pearson χ^2 test is only 0.530. Similarly, hybrids in the STH have a prominent second orientation peak (Figure 2.10d), but statistical tests cannot reject uniformity. Chaos in that same region have a more clearly multimodal distribution (Figure 2.10e). A simple explanation for a multimodal distribution of orientation is that the mapped region contains two separate populations of the type of microfeature considered, formed under different stress regimes, possibly at different times.

Evidence for several populations is also provided by the orientation distribution of chaos in the NLH (Figure 2.7e). The most elongated of these microfeatures exhibit a preferred orientation, yet all orientations are represented, unlike in clearly unimodal samples. There may be a set of uniformly oriented NLH chaos and a second set with a preferred orientation at 47°. The absence of geographical separation between these populations suggests that they formed at different times, indicating a change in the stress environment between these episodes.

Other studies have proposed that geological features on Europa can be grouped into separate sets, implying formations in discrete episodes rather than continuous activity (Figueredo & Greeley, 2004; Collins et al 2022).

Generally, chaos and hybrids exhibit more uniform orientation distributions than other microfeature categories. In contrast, pits display the tightest distributions,

with the STH being the only region where their distribution cannot be distinguished from uniform. Domes share similar characteristics to pits, with slightly less uniform distributions and, once again, a distribution that cannot be distinguished from uniform in the STH. Spots are not typically abundant enough for statistical analyses. These observations may suggest that the various microfeature types formed over different timescales within a temporally varying stress field. Pits and domes may form over a short time period during which the stress changes little, whereas hybrids and chaos develop over a longer time period and changing stress. This perspective aligns with the evolutionary models of e.g., Collins & Nimmo (2009) and Michaut & Manga (2014), where chaos, being more complex and larger features, require more time to form than the simpler and smaller pits, spots, and domes, and hybrids have an intermediate character.

If individual microfeature sets correspond to relatively short-lived formation episodes and microfeature elongation represents the stress field, microfeatures can reveal how stress changes over time. Formation models may imply a sequence from pits to domes, hybrids, and finally, chaos. In the NLH, this sequence implies a clockwise rotation, where domes and hybrids share similar orientations, approximately 30° clockwise from the orientation of pits (Figure 2.7). Chaos may exhibit a secondary orientation another 10° clockwise from that of domes and hybrids, while the more elongated chaos may have a completely different direction, orthogonal to that of pits. In the NTH, pits, hybrids, and chaos show similar preferred orientations, whereas domes display a different orientation, 30° anticlockwise to that of the other microfeatures (Figure 2.8). In the SLH, the potential formation sequence

implies an ~20° anticlockwise rotation from pits and domes, which exhibit the same orientation, to hybrids and chaos (Figure 2.9). Here, we analyze the peaks of the orientation distribution of hybrids and chaos, noting that their orientation distributions cannot be distinguished from uniform. Sarid et al. (2004) reported a possible anticlockwise rotation in the SLH of at least 720 ° using crack orientation. However, we cannot directly compare our results, as we are unable to determine which feature categories are the oldest. One could argue that pits are the oldest features, formed during a time when the microfeature formation process was limited and unable to advance to the chaos stage, or that they are the youngest features and have not yet had time to evolve into later stages. The lesser amount of rotation observed here may indicate that microfeature formation is more restricted than crack formation. Note that Sarid et al. (2006) found no consistent crack rotation direction in the NLH, in contrast to our results in Figure 2.7. In the STH, preferred directions cannot be confidently identified (Figure 2.10)

2.7 Conclusions

This study presents a systematic determination of microfeature elongation and orientation based on maps of pits, spots, domes, hybrids, and chaos in the Northern Leading Hemisphere, the Northern Trailing Hemisphere, the Southern Leading Hemisphere, and the Southern Trailing Hemisphere of Europa, as provided by Noviello et al. (2019b). The large size of this dataset makes it possible to conduct statistical analyses that, in many cases, validate the presence of significant preferred orientations for certain microfeature types and specific regions. Focusing only on the most elongated microfeatures yields more reliable evaluations of preferred orientation

in cases where there seems to be a background population of uniformly oriented microfeatures. Preferred orientations are found in every region when all microfeature types are combined, though these populations are dominated by one or another microfeature category. Pits are typically the smallest features but also exhibit the most pronounced preferred orientations, followed by domes. The largest microfeatures are chaos, which tend to have more complex orientation distributions. The Southern Trailing Hemisphere has the highest instances of uniformity among feature types. No systematic change in orientation by latitude could be determined documented.

All these characteristics support models where microfeature emplacement is episodic in a temporally variable stress field. We advocate for an evolution model of pits and domes transitioning into hybrids and chaos, suggesting that chaos forms over a longer period when stress is less well defined. These results indicate that local and regional stresses on Europa may have a greater influence on microfeature morphology compared to global stresses. Previous studies of microfeature formation (Fagents, 2003; Head & Pappalardo, 1999; O'Brien et al., 2002; Pappalardo & Barr, 2004; Quick et al., 2017; Rathbun et al., 1998; Showman & Han, 2004; Sparks et al., 2017) do not consider the influence of horizontal stress; however, we demonstrate that elongation is a characteristic feature of microfeatures. Conceptually, our observations are most compatible with the effects of stress on a subsurface diapir or liquid water body.

Chapter 3. Coronae Elongation in Relation to Chasmata on Venus

3.1 Abstract

Coronae were first identified during the Venera 15/16 mission as annuli of tectonic and volcanic features. Since then, new studies have mapped and shown that these features vary morphologically and spatially, with different relationships between annuli of high elevation, low elevation, faults, and volcanic features. Most formation models link corona morphologies with various stages of interaction between a mantle plume and the lithosphere and may involve spontaneous or plume-induced delamination and subduction. Therefore, coronae may be influenced by the state of stress in the lithosphere. Here, we search for evidence of this influence in the shape of coronae. We systematically measure corona elongation over a larger global dataset and find that coronae are typically slightly elongated. Furthermore, the directions of their elongation are not uniformly distributed. It appears that Chasmata lineaments and nearby coronae often share similar elongation directions. We tested this observation by calculating the misorientation of coronae and Chasmata lineaments. We defined misorientation as the difference between the Chasmata orientation and the mean orientation of nearby coronae, determined by a distance-weighted average of the coronae orientations. The frequency distribution of misorientation contains two major peaks: the first around 15° to 30° and the second around -15° to 0°. Lower misorientation values do not seem geographically restricted. High misorientation values primarily appear at Chasmata near the Beta- Alta- Themis

(BAT) region. These relations are consistent with the hypothesis that coronae exploit preexisting faults or lithospheric weak zones associated with the Chasmata rifts. An underlying plume may pool along an elongated step in lithosphere thickness. Alternatively, melt may be preferentially injected in the direction of maximum horizontal compressive stress parallel to the rift axis. The often-discussed proximity of coronae and Chasmata may indicate that coronae formation takes advantage of the lithosphere-scale weakness provided by major rifts. Here, we show that rift-related stress or structures also influence the shape of the corona.

3.2 Introduction

Venus and Earth have similar global characteristics, including mass, size, and density. Despite these similarities, the geology of Venus differs significantly from that of Earth. By studying Venus and contrasting it with Earth, we investigate how planets evolve and remain geologically active without plate tectonics. In particular, coronae are of interest. No analogous structure has been definitively recognized in the terrestrial geological record (Ernst & Desnoyers, 2004) However, they are thought to form through interactions between the lithosphere and mantle plumes (Gülcher et al., 2020; Janes et al., 1992; Smrekar & Stofan, 1997), a process thought to occur on Earth. Therefore, these features provide insight into Venus' internal dynamics and may offer critical clues regarding the differences between these planets. In this study, we will quantify the elongation and orientation of coronae on Venus, an aspect of their morphology that has not been systematically reported before. With this new dataset, we will compare the orientation of rifts to that of coronae to investigate the

influence of regional lithospheric stresses and heterogeneities on the shape of coronae.

The Venera 15 and 16 probes provided the first images of coronae. These features were initially identified in Ishtar and Tethis Regio by their concentric ridges and grooves and were described as having an ovoid shape (Barsukov et al., 1986). Further analysis of these images revealed complex interiors filled with volcanic flows, domes, plateaus, rims, tectonic ridges, and depressions (Pronin & Stofan, 1990). By the 1990s, the Magellan mission offered high-resolution global coverage of Venus, facilitating the expansion of the coronae dataset. The dataset that once contained 21 coronae grew to 362 (Stofan et al., 1992) and later to 515 (Stofan et al., 2001). At the time of writing, neither dataset had been digitized.

These new datasets were the first to measure and quantify global coronae morphologies. Coronae were found to have diameters ranging from 60 to 2000 km, with Artemis Corona being the largest (Glaze et al., 2002; Squyres et al., 1992; Stofan et al., 1992, 2001). Some authors, however, have suggested that Artemis, with its unique size and morphology, should be considered separately from coronae (Brown & Grimm, 1995; Hansen, 2002; Hansen & Olive, 2010). As the range of observed corona morphological characteristics increased, coronae were divided into five distinct classes based on annulus style. This initial result led to the definition of a potential morphological evolution of coronae (Janes et al., 1992).

Later classification efforts defined Type 1 and Type 2 coronae based on the angular span of their fracture annulus. Type 1 coronae have an annulus that spans more than 180° of arc of fracture. In contrast, Type 2 coronae have an annulus that

spans less than 180° of arc of fracture (Stofan et al., 2001). Glaze et al. (2002) would later show that these two types are indistinguishable by size and should be treated as a part of the same population. However, Type 1 and Type 2 coronae differ not only by their annulus but also by their locations in relation to chasmata, which are large extensional features that occur globally on Venus. Chasmata are categorized by a trough and fracture system that can display volcanism (Hamilton & Stofan, 1996; Shalygin et al., 2015; Stofan et al., 1989). Coronae, in general, have a nonrandom spatial distribution (Stofan et al., 1992). Type 1 corona are preferentially located near Chasmata (Squyres et al., 1993; Stefanick & Jurdy, 1996). Type 2 coronae, in contrast, are more likely to be isolated features in the plains regions (Stofan et al., 2001). It has been shown that coronae tend to be in clusters, with the largest clusters found in the Beta-Alta-Themis (BAT) region (Squyres et al., 1993). Although they are spatially close to each other, coronae and chasmata do not appear to have any genetic association (Krassilnikov et al., 2012; Martin et al., 2007), although numerical models of plume-lithosphere interaction have shown that chasmata can affect corona evolution (Piskorz et al., 2014).

Despite various studies on the morphology of coronae, there has not been much focus on their shape, perhaps because theoretical models of plumes often assume an axisymmetric structure. The only previous mention of coronae and their elongation was in Pronin and Stofan (1990b). They showed that coronae in the Venera 15/16 images have a similar orientation to the surrounding tectonic features. They also noted that their sample size, 21 coronae, has an elongation range that spans from 1:1

to 2:1. This type of study was not expanded upon once the global Magellan data became available.

Due to a lack of orientation data and the limitations of geodynamic models, little information is available to explain the shape of coronae. Three-dimensional modeling efforts like those from Gülcher et al. (2020; 2023) have begun investigating the topographic asymmetry of coronae. Gülcher et al. (2023) found that variations in crustal thickness could be responsible for the asymmetry observed in 155 selected coronae. While the study addresses the topographic asymmetry of coronae, it does not provide quantitative measures for their shape in a global context.

In this study, we measure the circularity and orientation of coronae to create a comprehensive digital global dataset of new morphological characteristics of coronae on Venus. We employ various statistical tests to determine the significance of our coronae orientation values. We also map chasma lineaments across Venus and measure their orientations to serve as indicators of the orientation of the regional stresses. The strike of chasmata is assumed to be perpendicular to the maximum extensional horizontal stress direction. Thus, the misorientation between chasmata and corona represents the difference between the orientation of the coronae's long axis and the direction of maximum extensional horizontal stress. This enables us to investigate the mechanisms that may have controlled the shape of coronae. Using our results, we elaborate on three potential mechanisms: caldera formation is sensitive to lithospheric stresses, calderas elongate along preexisting structures, or deformation post-formation. Our results show that calderas are elongated parallel to the maximum

compressional horizontal stress indicating that calderas are elongated by regional stresses or through the preferentially injection of magma along preexisting structures.

3.3 Methods

3.3.1 Mapping Coronae and Rifts

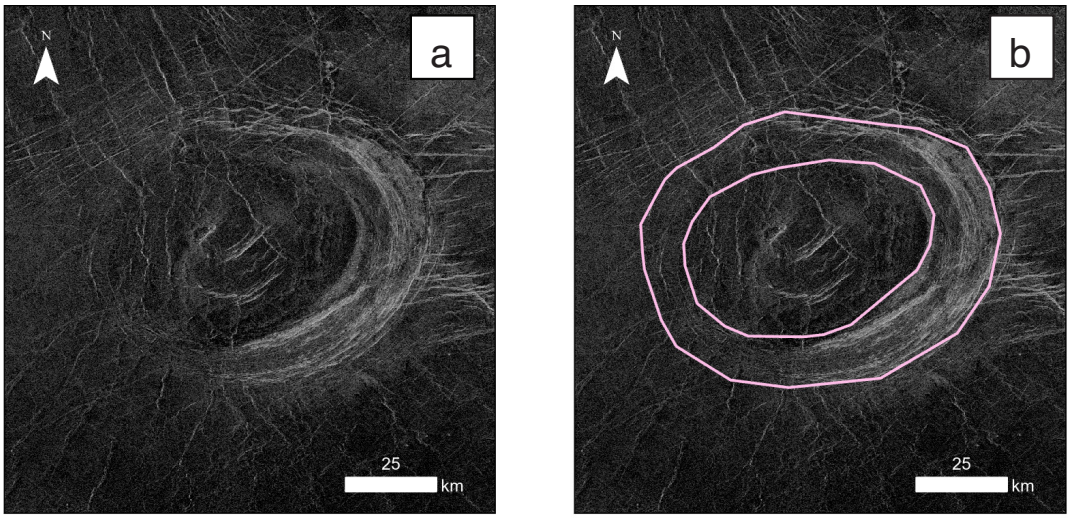


Figure 3-1: Unnamed coronae south of Epona Coronae in Alta Regio a) and mapped outline of the inner and outer boundaries of the corona's annulus. Galileo FMAP Left-Look image centered at 148.8°W and 29.5°S.

We define the elongation of a corona based on the outline of its annulus. As there is no systematic database containing this information, we mapped corona outlines using the Magellan SAR FMAP Left Look Global Mosaic as our basemap. We used two databases as a starting point to identify the locations of coronae: one from Stofan et al. (1992a) and the IAU database (International Astronomical Union Working Group for Planetary System Nomenclature, 2024). The IAU dataset provided a minimum list of 339 confirmed coronae, whereas Stofan et al. (1992a) expands on this list and has become the foundation for other studies analyzing

coronae (Head et al., 1992; Janes et al., 1992; Koch & Manga, 1996; Sabbeth et al., 2024; Schools & Smrekar, 2024; Squyres et al., 1992). Stofan et al. (1992a) provided a list of 362 coronae and coronae-like features. A later study, (Stofan et al., 2001), increased the dataset to 515 coronae.

Table 3-1: Mapping scale for various corona diameters

Diameter[1]	Scale
0 km - 100 km	1:1,942,112
100 km - 200 km	1:2,657,970
200 km - 300 km	1:4,536,059
300 km - 400 km	1:7,087,592
400 km - 500 km	1:9,733,327
500 km - 600 km	1:10,174,122
600 km - 700 km	1:11,953,327
700 km - 800 km	1:12,871,407

Coronae located between 60°N and 60°S were mapped on an equirectangular projection, while those in the north and south polar regions were mapped on polar projections. Subsequent analyses are based on the sets of latitudes and longitudes of the vertices along the outlines, yielding elongation and orientation estimates that are independent of the original map projection. For consistency, we map corona outlines at specific scales. However, the wide variety of corona sizes meant that we relied on

[1] Taken before mapping from the IAU database.

different scales for mapping the outlines. Table 3.1 reports the map scale used for coronae based on their diameter ranges. When possible, we used the diameter reported in the IAU database to select the mapping scale before mapping the annulus. For coronae not found in the IAU dataset, we roughly measured the maximum diameter and chosen an appropriate scale from Table 3.1. This approach ensured that we considered the entire outline of each corona during the mapping process.

All coronae were mapped twice: first to determine the inner boundary of the annulus and then to map its outer outline. We calculated the area, central latitude, and longitude of both the interior and exterior outlines. These values were derived using the Calculate Geometry tool in ArcGIS (see Chapter 2). The minimum bounding geometry tool in ArcGIS generates a new polygon shapefile based on the smallest polygon that can encapsulate all the vectors of the original coronae outline (convex hull). The tool also reports the elongation and orientation of this outline, but we recalculated this quantity with a bespoke Matlab script to better grasp how these quantities are defined. To achieve this, we consider the position vectors that link the center of the planet to points on its surface, $\vec{P}$. Given φ and λ the latitude and longitude of this point:

$$\vec{P} = \begin{bmatrix} \cos\lambda\cos\varphi \\ \sin\lambda\cos\varphi \\ \sin\varphi \end{bmatrix} \tag{3.1}$$

We calculate the geodesic distances between each pair of points along the outline. The pair of points that are the furthest apart from one another defines the corona's long axis, $\overrightarrow{v_L}$. The corona's orientation is defined by the azimuth of this vector, which is the angle between the North direction and v_L. To find the length of

the corona's short axis, we project the position vectors of all the other outline vertices onto the unit vector perpendicular to the long axis, $\overrightarrow{v_\perp} = \frac{\overrightarrow{P_L} \times \overrightarrow{v_L}}{\|\overrightarrow{P_L} \times \overrightarrow{v_L}\|}$, where $\overrightarrow{P_L}$ is the position vector of one end of $\overrightarrow{v_L}$. Note that this projected distance can be positive or negative. Then, the short axis length is given by the difference between the largest and smallest projected distances. Finally, the circularity of the corona is given by the ratio of the short axis length to the long axis length.

According to this algorithm, corona orientation is defined as the angle between the north direction and the long axis v_L of the convex hull surrounding a mapped outline. Since these axes are non-directed, orientation is described as an angle ranging from 0° to 180°. Corona elongation is quantified by the outline's circularity; however, it is important to note that the aspect ratio of a corona is the inverse of circularity. A circularity value of 1 indicates a perfect circle, while a highly elongated outline has a circularity close to 0. We prefer using circularity as, unlike the aspect ratio, it is bounded.

To determine the strike of chasmata, we mapped several lineaments within the chasmata identified in the IAU dataset. Since the IAU dataset represented each chasma as a point, it was impossible to obtain strike values directly from it. To identify which lineaments correspond to a specific chasma, we referenced the quadrangle geologic maps of Venus. We imported each map into ArcGIS and georeferenced them to serve as guides for mapping lineaments along the rift system. We mapped seven to ten lineaments along the length of each chasma. Each lineament represents the local strike of the rift, resulting in seven to ten local strike values per chasma. We define the strike of the rift as the circular average of these values (See

Chapter 2). Due to difficulties in mapping rifts in the polar regions caused by projection limitations and data gaps, we only used the chasmata located between 60°N and 60°S in our analysis. We also excluded rifts that were listed in the IAU dataset but lacked apparent lineaments.

3.3.2 Misorientation

Comparing the orientation of a corona to another object, such as a lineament or a rift, requires defining a misorientation between the two. Since the orientation is defined as the azimuth of a non-directed axis representing the object, misorientation spans 180°. We report it here as an angle between -90° and 90°.

In Cartesian geometry, this can be easily achieved by taking the difference between the orientations of the two objects. However, defining misorientation when objects are defined on a sphere is more challenging. For example, the azimuth of a line following a great circle, also called a heading, changes along the great circle. Reporting the difference between azimuths would lead to non-zero misorientation, even though it stands to reason that the lines pointing along the azimuth in this scenario should be parallel to one another. Their misorientation should be zero even thought their azimuth changes along the great circle.

As a result, we calculate misorientation by drawing parallel small circles based on the same concept as the lines of constant latitude on the globe and determine the deviation of an axis from these lines. To achieve this, we first consider a lineament defined by its two end points at the position vectors $\overrightarrow{p_1}$ and $\overrightarrow{p_2}$. The great circle that follows the lineament represents the intersection between the sphere and a plane passing through the center of the planet with a normal vector

$$\vec{N} = \frac{\overrightarrow{p_1} \times \overrightarrow{p_2}}{\|\overrightarrow{p_1} \times \overrightarrow{p_2}\|} \tag{3.2}$$

We call this plane the rift plane (Figure 3.2a). All the planes parallel to the lineament are also normal to $\vec{N}$, so they never intersect the rift plane. The point to be compared to the reference point is at the position $\vec{P}$. In our application, this will be a corona. A unit vector parallel to the lineament (Figure 3.2b) is given by

$$\vec{R} = \frac{\vec{P} \times \vec{N}}{\|\vec{P} \times \vec{N}\|} \tag{3.3}$$

we project this vector along $\overrightarrow{e_N}$ and $\overrightarrow{e_E}$, unit vectors pointing North and East at $\vec{P}$.

$$\overrightarrow{e_N} = \begin{bmatrix} -\cos\lambda \sin\varphi \\ -\sin\lambda \sin\varphi \\ \cos\varphi \end{bmatrix}, \qquad \overrightarrow{e_E} = \begin{bmatrix} -\sin\lambda \\ \cos\lambda \\ 0 \end{bmatrix} \tag{3.4}$$

and obtain the azimuth of the rift-parallel vector ζ_R thanks to

$$\cos\zeta_R = \vec{R} \cdot \overrightarrow{e_N}, \qquad \sin\zeta_R = \vec{R} \cdot \overrightarrow{e_E} \tag{3.5}$$

The misorientation is then the difference between the corona orientation, ζ_c, and ζ_R, restricted modulo 180° to be between -90° and 90°. A misorientation of 0° indicate perfect alignment between the reference object and the sample considered.

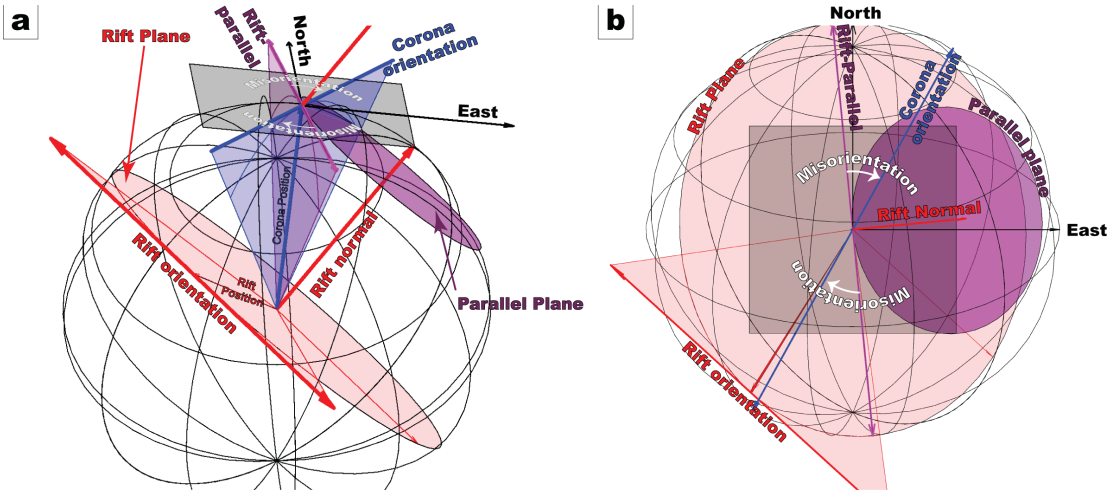


Figure 3-2: Calculation of the misorientation on a sphere. a) The rift plane (pink) contains the vector linking the endpoints of the rift (red triangle, length exaggerated). The purple disk highlights a plane parallel to the rift plane at the corona location (blue vector). Both planes are normal to the rift-normal vector (red arrow). The corona orientation and the rift-parallel orientation at the corona location are represented by the blue and purple triangles. The grey square represents a plane tangential to the sphere at the corona's location, with its edges parallel to the East and North directions. b) View looking down at the corona location. The misorientation (white) is defined as the difference between the azimuth of the corona and that of the rift-parallel axis at the corona location, here 34.6°. The thin black lines on both panels represent parallels and meridians separated by 30°.

3.3.3 Calculating Circular Weighted Averages

We aim to systematically compare the orientation of coronae and chasmata. To achieve this, we calculate the average orientation of coronae that are near a given chasma and subtract this orientation from that of the chasma. The challenge in this calculation lies in defining "close" in a reproducible manner. Instead of choosing an

arbitrary cutoff distance, we prefer to define a continuous weight function that decreases with increasing chasma-corona distance. The same weights can be applied to average other morphometric quantities such as corona area and elongation to indicate the general characteristics of coronae that are "close" to a given chasma.

A Euclidean distance equation is not appropriate for this calculation, as it does not account for the planet's curvature and would yield inaccurate results at large distances. Instead, we define the distance weight based on a Fisher distribution (Fisher et al., 1987), originally used to measure the density of data at a point on a sphere.

$$h(\theta) = C_f e^{\kappa \cos\theta} \tag{3.6}$$

where θ is the angular distance between two points, κ is the concentration factor, and C_f is a normalization factor given by

$$C_f = \frac{\kappa}{4\,\pi \sinh\kappa} \tag{3.7}$$

The weighted average at a point P of quantity f sampled at n points P_i is given by

$$f(P) = \frac{\sum_{i=1}^{n} f_i \times W(P, P_i)}{\sum_{i=1}^{n} W_n(P, P_i)} \tag{3.8}$$

where the weights $W\ (P, P_i)$ are defined as

$$W(P, P_i) = \frac{\kappa}{4\,\pi \sinh\kappa}\ e^{\kappa \cos\theta_i} \tag{3.9}$$

where θ_i is the angle between P and P_i. We calculate $\cos\theta_i$ according to

$$\cos\theta_i = x\,x_i + y\,y_i + z\,z_i \tag{3.10}$$

where, x, y, and z are the components of a unit vector from the center of the planet pointing to the point P (Equation 3.1), and x_i, y_i, and z_i are the equivalent for the point P_i.

The concentration parameter represents the speed of the fall-off as a function of distance from point P. At high κ, only the points closest to P contribute significantly to the average. To express this closeness more intuitively as a critical distance, we proceed by drawing an analogy with the standard deviation of a Gaussian distribution. The value of the distribution one standard deviation away from the peak is $Ae^{-1/2}$, where A is equal to the maximum value of the distribution. By analogy, we define the decay distance of the Fisher distribution as the angle θ_{κ} at which the distribution is a factor $e^{-1/2}$ less than at its maximum:

$$h(\theta_{\kappa}) = C_f \, e^{\kappa \cos\theta_{\mathrm{sd}}} = C_f \, e^{\kappa - \frac{1}{2}}$$

$$\theta_{\kappa} = \cos^{-1}\left(1 - \frac{1}{2\kappa}\right) \tag{3.11}$$

At the surface of Venus, this decay distance is given by

$$D_{\mathrm{Venus}} = R_{\mathrm{Venus}} \, \cos^{-1}\left(1 - \frac{1}{2\kappa}\right) \tag{3.12}$$

where R_{Venus} is the radius of the planet. Following Martin et al. (2007) our κ values are larger than 16, as this corresponds to a physical distance larger than 1500, a hypothesized limit of rift influence. Figure 3.3 illustrates how the weighting function varies with distance on Venus for various values of the concentration parameter.

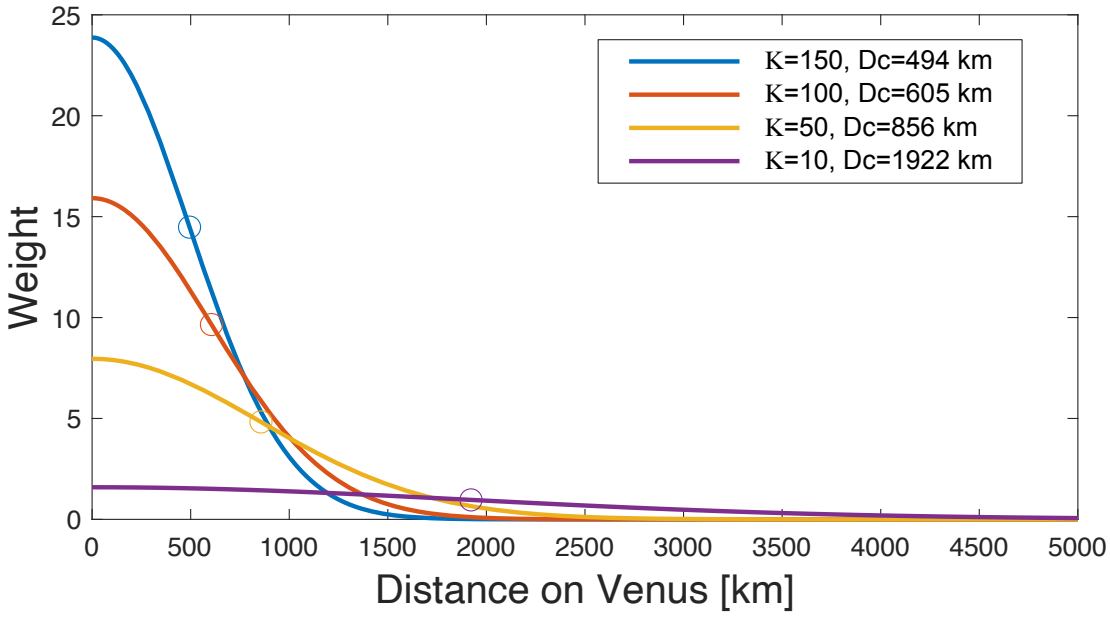


Figure 3-3: Fisher-based weighing functions presented against distance on Venus for various values of the concentration parameter κ. The circles indicate the decay distance, D_c. For reference, the antipode is approximately 19,012 km on Venus.

In circular statistics, average orientations are calculated using the resultant vector, which is the sum of unit vectors pointing in the direction of each orientation data in a sample. For axial (non-directed) data, such as the azimuth examined here, the orientation angle must be multiplied by 2 before the summation to eliminate the 180° ambiguity in the measurement (See Chapter 2). For a sample of n orientation measurements $\{\theta_i\}$, the circular average of the orientation, $\bar{\theta}$, is given by

$$\bar{\theta} = \operatorname{atan}\left(\frac{\bar{s}}{\bar{c}}\right) \tag{3.13}$$

$$\bar{s} = \frac{1}{n}\sum_{i=1}^{n} \sin 2\theta_i\,, \qquad \bar{c} = \frac{1}{n}\sum_{i=1}^{n} \cos 2\theta_i \tag{3.14}$$

The circular variance V characterizes the spread of the data

$$V = 1 - \sqrt{\bar{c}^2 + \bar{s}^2} \tag{3.15}$$

Its values range from 0 to 1, with higher values of V indicating a broader distribution.

Here we generalize this approach by introducing the distance weights defined in Equation 3.8 into Equation 3.13:

$$\bar{s} = \frac{\sum_{i=1}^{n} \sin 2\theta_i \times W_n(P, P_i)}{\sum_{i=1}^{n} W_n(P, P_i)}, \qquad \bar{c} = \frac{\sum_{i=1}^{n} \cos 2\theta_i \times W_n(P, P_i)}{\sum_{i=1}^{n} W_n(P, P_i)} \tag{3.16}$$

Note that the normalization factor $\sum_{i=1}^{n} W_n(P, P_i)$ cancels out in Equation 3.9, which can be written as

$$\bar{\theta} = \frac{1}{2} \operatorname{atan}\left(\frac{\sum_{i=1}^{n} \sin 2\theta_i \times W_n(P, P_i)}{\sum_{i=1}^{n} \cos 2\theta_i \times W_n(P, P_i)}\right) \tag{3.17}$$

The same weights are used to calculate weighted averages for distance, $\overline{D}$ and circularity $\bar{C}$:

$$\overline{D} = \frac{\sum_{i=1}^{n} D_i \times W_n(P, P_i)}{\sum_{i=1}^{n} W_n(P, P_i)} \tag{3.18}$$

$$\bar{C} = \frac{\sum_{i=1}^{n} C_i \times W_n(P, P_i)}{\sum_{i=1}^{n} W_n(P, P_i)} \tag{3.19}$$

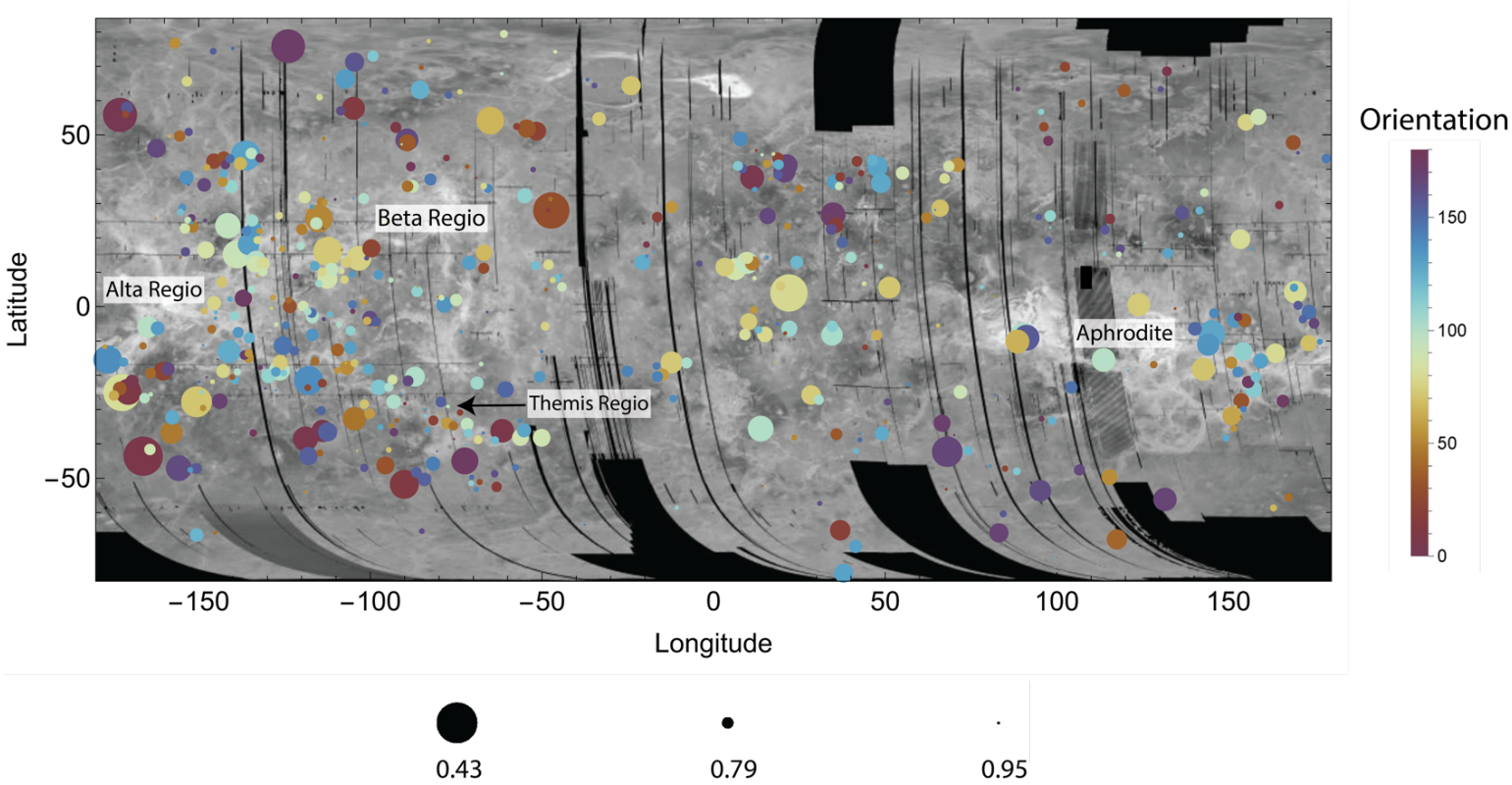


Figure 3-4: Global map of coronae located between 90°N and 90°S on Venus. The size of the points is scaled to the inverse of the circularity so that a larger point represents an elongated corona. Each point's color indicates the orientation of the corona's exterior outline. The color scale is the RomaO color map from Crameri (2023).

3.4 Results

3.4.1 Corona Elongation and Orientation

We mapped a total of 525 coronae. Of the mapped coronae, 12 were in the south polar region (south of 60°S), while 42 were mapped in the north polar region (north of 60°S), and the remaining 471 coronae were in the equatorial region (between 60°S and 60°N latitude; Figure 3.4).

A large concentration of coronae is found in the Beta-Alta-Themis (BAT) region (Stofan et al., 1992). In this region, coronae are both located within and flanking rift systems. In Figure 3.4, most coronae are located along Parga Chasmata and Hecate Chasma, while there appear to be fewer coronae along Devana Chasma. In comparison, coronae in the Aphrodite region are less concentrated. There appear to be a large concentration of coronae in the eastern portion of Aphrodite (150°E, -10°S), compared to the western side (100°E, 0°). Coronae outside major rift systems are also fewer in number and tend to appear in clusters. These smaller clusters are most prominent in the plain region, like the one located at 15°E, 40°N . Figure 3.4 shows very few instances of isolated coronae. These spatial results agree with those found in (Stefanick & Jurdy, 1996; Stofan et al., 1992, 2001), although we have fewer coronae than Stofan et al. (2001).

For completeness, we measured the orientation, circularity, diameter, and area of both the interior and exterior outlines of each corona annulus (Nuñez et al., 2025). Aggregate statistics on each of these quantities are gathered in Table 3.2. Following the procedure in Stofan et al. (1992), we define the corona's diameter as the maximum length found among the two outline types. We did not consider Artemis when calculating area or diameter statistics, as it is a clear outlier compared to the

global corona population, which may have formed via different mechanisms (Brown & Grimm, 1995; Hansen, 2002; Hansen & Olive, 2010).

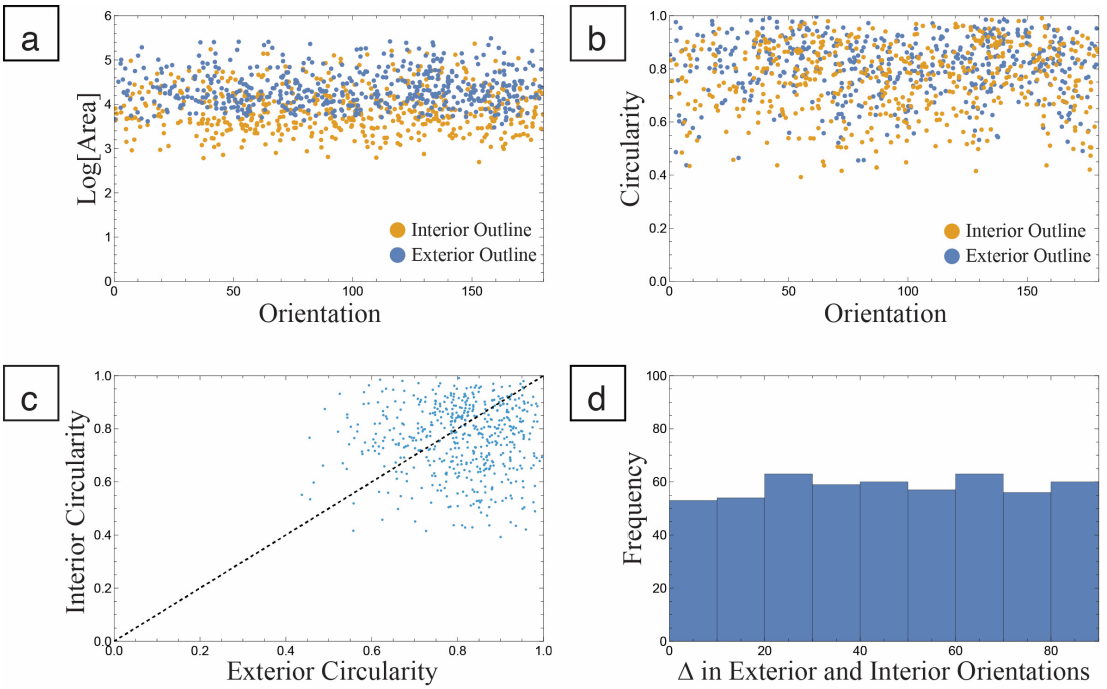


Figure 3-5: Morphological characteristics of coronae. Scatter plots of area (a) and circularity (b) of coronae against their orientations show that these morphological characteristics do not depend on one another. In panels (a) and (b), the orange and blue points represent the interior and exterior outlines, respectively. (c) Exterior vs. Interior circularity. The dashed line follows the 1:1 interior and exterior circularity ratio. We see a large spread of circularity along this line. (d) The difference between the corona's exterior and interior orientations was calculated by taking the difference between the two orientation values and reporting the smallest angle.

Coronae in the north and south polar regions are, on average, larger than those found in the equatorial region. The interior area of each caldera is about half its exterior area (Figure 3.5a). Coronae in the equatorial region seem to exhibit the

thickest annuli. The average circularity of all three regions has a range of 0.72 to 0.81. In all three regions, the interior outlines are, on average, more elongated than the exterior outlines (Table 3.2), but the difference is smaller than the standard deviation of circularity within each region. In all three regions, the coronae predominantly point NW-SE (Table 3.2). The mean orientation values (Equation 3.13) remain consistent across all datasets, except for the mean orientation of the exterior outlines in the North Polar Region, where coronae, on average, are oriented N-S. We calculated the circular variance (Equation 3.15) to examine the spread of the orientation data around the mean. The South Polar Region exhibits the lowest circular variance, though this could be attributed to a smaller sample size. The other regions display a wide distribution around the mean orientation, which diminishes the significance of the globally averaged orientation reported in Table 3.2.

The interior outlines of coronae are slightly more elongated than their exterior outlines (Table 3.2), although the difference is small compared to the standard deviation of circularity. Figure 3.5c presents the correlation between interior and exterior outline circularity. We observe that our data deviates significantly from the 1:1 ratio line, and many coronae have a less elongated (higher circularity) interior outline than exterior outline. Therefore, we conclude that the lower elongation values of the interior outline seen in the global averages are not a representative characteristic of coronae.

In Figure 3.5, the size of the symbols is scaled to the exterior circularity, so that the more elongated coronae appear larger in this figure. We find no pattern in the spatial distribution of the exterior elongation. Across the BAT and Aphrodite, the

numbers of low and high circularity coronae are similar (Figure 3.5). This pattern also holds for coronae outside of these larger rift systems. Highly elongated or circular coronae do not occur preferentially in any geographical region or geological setting.

Globally, the interior and exterior outlines have similar average orientation and circular variance (Table 3.2). However, the differences between the interior and exterior outline orientations appear to be uniformly distributed (Figure 3.5d). Coronae are equally likely to have interior and exterior outlines that are parallel or perpendicular to each other.

Figure 3.5 shows no spatial pattern in the orientation of coronae, as indicated by the color of the symbols in this figure. The orientation distributions of coronae in the BAT and Aphrodite Terra appear indistinguishable from one another. Although the BAT contains more coronae, the range of orientation values is similar to that of Aphrodite Terra. Coronae outside these regions also do not exhibit a preferential orientation. In the plains, there is a mix of coronae orientations. Two clusters of coronae, one north and the other south of Aphrodite Terra, appear to have a tighter range of orientations. The northern cluster (~115°E and 55°N) contains nine coronae with orientations ranging from 35° to 0°. In the southern cluster, orientations range from 120° to 145°. Ultimately, we find no convincing evidence that corona orientation depends systematically on location.

Figure 3.5 allows for a comparison between the orientation and other morphological characteristics of coronae. However, no systematic trends can be discerned in these plots. Figure 3.5a shows that the area of a corona does not depend on its orientation, regardless of outline type. The circularity does not vary

systematically with orientation either (Figure 3.5b). In summary, the orientation of coronae is not dependent on location, area, or circularity.

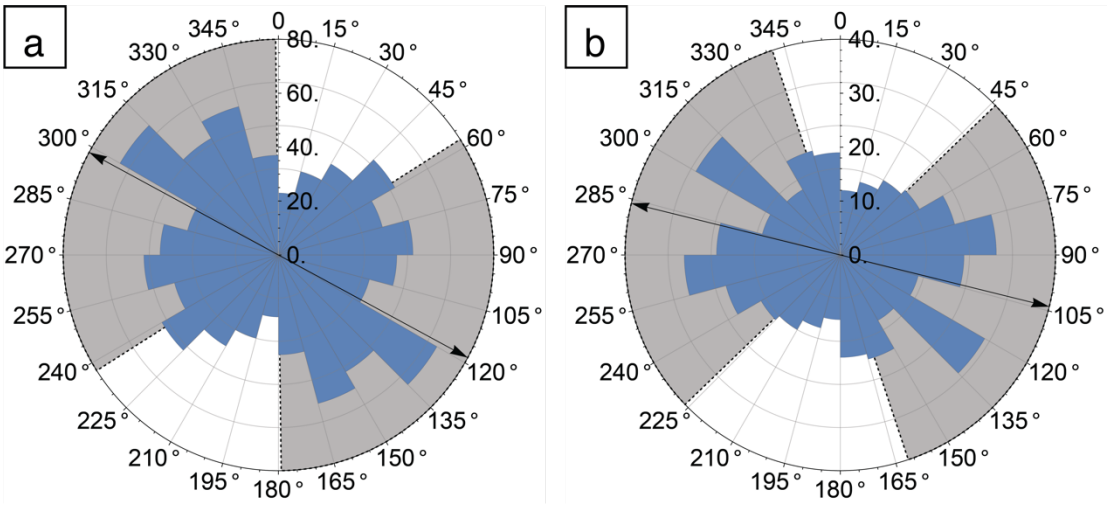


Figure 3-6: Rose diagrams comparing the orientation distributions of (a) all mapped coronae and (b) coronae with below-average circularity. The black double-headed arrows indicate the mean orientation, while the shaded gray region represents the circular standard deviation. Each rose diagram is mirrored to display a 0-360° range.

Corona orientation is broadly distributed (Figure 3.5), but its average remains consistent across different map areas (Table 3.2). The rose diagram indicates that the orientation data is not uniformly distributed (Figure 3.6a). We conducted three statistical tests to verify our visual inspection and evaluate our null hypothesis of uniformity: the chi-squared test for goodness of fit, the Modified Kuiper Test, and the Rayleigh test of uniformity (See Chapter 2). All tests indicated that, at a 99% confidence level, the orientation distribution of global coronae exterior outlines is not uniform. We repeated our tests on the orientation data for the interior outlines; this data passed all tests except the chi-squared test for goodness of fit. This result implies

that the interior outlines of the corona annulus provide little generic information about coronae, in contrast to the exterior outlines. Furthermore, the exterior outline is less likely to have been modified by later stage processes within the corona's interior. Therefore, from now on, we will exclusively use the exterior outline orientations for further orientation analysis.

We considered the possibility that orientation is measured less reliably in coronae that are nearly circular and produce an orientation rose diagram restricted to coronae with a circularity less than the global mean of 0.81 (Figure 2.6b). The filtered dataset, containing 232 coronae, displays a similar orientation distribution to that of the original 525 coronae. These distributions are broad but non-uniform. The elongated coronae dataset features a prominent narrow peak at 120-130° and a broad peak at 75-90°. The large, narrow peak is the same as in the non-filtered dataset. Both the mean orientation and variance decreased for the new dataset, but by only 12° and 0.03, respectively. This difference is not significant. Statistical tests indicate that the orientation distribution of coronae with below-average circularity has a 5% probability of being uniform. While this is higher than found using the entire dataset, the preferred orientation of elongated coronae can be considered significant.

Table 3-2: Summary of the morphological characteristics of all 523 mapped coronae.

		Global	Equator	North Pole	South Pole
Interior	Mean Area	15,680 km^2	13,600 km^2	31,574 km^2	41,681 km^2
	Mean Diameter	140 km	133 km	203km	238km
	Mean Circularity	0.76 ±0.13	0.77±0.13	0.72±0.14	0.76±0.13
	Mean Orientation	101°	99°	127°	122°
	Circular Variance	0.89	0.89	0.94	0.74
Exterior	Mean Area	37,135 km	33,800 km^2	65,020 km^2	70,176 km^2
	Mean Diameter	220	211 km	286 km	308 km
	Mean Circularity	0.81±0.11	0.81 ±0.11	0.79± 0.12	0.80± 0.13
	Mean Orientation	118°	114°	1.37°	146°
	Circular Variance	0.90	0.88	0.86	0.60

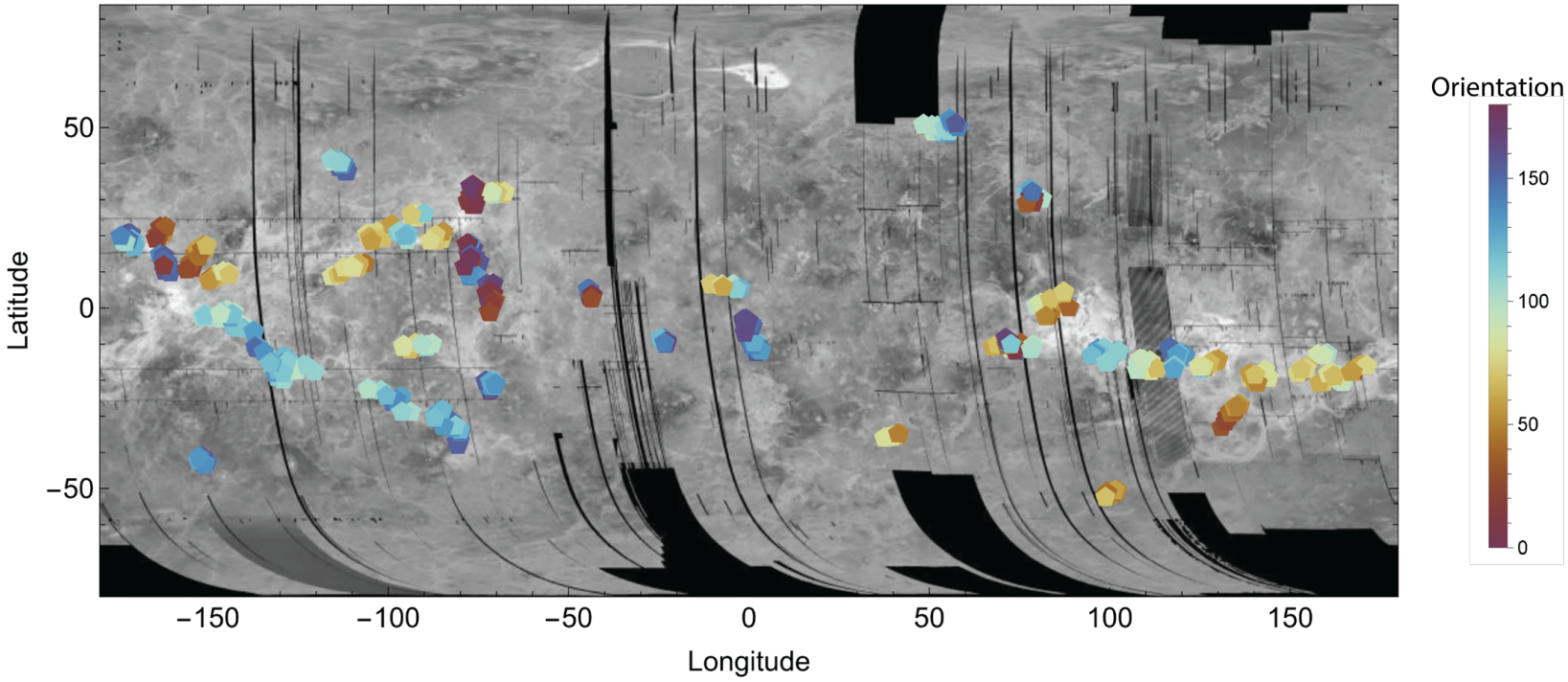


Figure 3-7: Chasmata lineament orientation. The color of the pentagon represent lineament orientation. Chasmata appear to have regionally consistent orientations.

3.4.2 Rift Orientations

We use rifts as indicators of regional stress that may influence corona formation and elongation. A chasma (plural chasmata) is defined as "a deep, elongated, steep-sided depression" (USGS Astrogeology Science Center, n.d.). Most chasmata are interpreted as the result of tectonic extension occurring normal to their long axis (Guseva, 2016; Magee & Head, 1995; McGill et al., 1981; Solomon et al., 1992). The stress field at the origin of rifts on Venus may relate to deep-seated processes such as plumes, in contrast to the plate tectonics origin of rifts on Earth (Adams et al., 2023; Graff et al., 2018; Harris & Bédard, 2015; Kiefer & Peterson, 2003; Kiefer & Swafford, 2006; Regorda et al., 2023). Regardless of the precise origin of the rifts, their tectonics indicate that the maximum horizontal compression axis is parallel to the rift axis. We consider that individual lineaments inside each chasma, which likely represent individual faults or graben, collectively represent the regional stress and strain directions better than the chasma outline itself, which can be complicated by rift kinks and offsets. For example, the strike of Zverine Chasma varies by about 45 degrees from each end.

We mapped a total of 599 chasma lineaments belonging to 39 chasmata in the equatorial region. The mean length of a mapped lineament was approximately 105 km. Only 8% of the mapped chasmata are located away from the BAT and Aphrodite regions. Because we limited our mapping to named rifts, we may not have a representative sample of rifts outside of the BAT and Aphrodite regions.

Figure 3.7 shows that lineaments have a consistent orientation in specific regions, in contrast to the coronae orientation dataset. Each side of the chasmata that outlines the BAT region presents a specific preferred orientation. Between Atla and

Themis Regio, rift lineaments trend NW-SE. In this region, we have mapped five chasmata: Parga Chasma, Chondi Chasma, Dziwica Chasma, Lesavka Chasma, and Kicheda Chasma. Eighty-six lineaments were mapped in this area, most of which are associated with Parga Chasma. The mean orientation of these lineaments is approximately 119° with a circular variance of 0.146. This region also contains more coronae than the other legs of the BAT triangle (Figure 3.4). At the western end of this area, three chasmata appear radially oriented with respect to Ozza Mons. Three chasmata located between Alta and Beta Regio, Hanwi Chasma, Hecate Chasma, and Latona Chasma, have similar orientations, with a mean value of 72.9° and a circular variance of 0.0785. Zverine Chasma is in this region but has lineaments that radiate from Kono Mons, with mean lineament orientations of 66.4° and 114° in the western and eastern halves of Zverine, respectively. Two N-S trending rifts, Devana Chasma and Rona Chasma, characterize the last section of the BAT. Theia Mons is situated in the center of Devana Chasma, but the orientation of the rift lineament is maintained north and south of Theia Mons.

Chasmata located away from the BAT and Aphrodite Terra do not appear to have preferred orientations. These rifts are in regions with lower coronae concentrations than in the BAT (Figure 3.4). We consider ten chasmata separated from the BAT and Aphrodite Terra: Olapa Chasma, Mist Chasma, Heng O Chasma, Gui Ye Chasma, Nang-Byon Chasma, Dewi Ratih Chasma, Artio Chasma, Reitia Chasma, Kottravey Chasma, Kaygus Chasma, Mežas-Mate Chasma, and Mots Chasma. The orientation of the rift lineaments of these ten chasmata is narrowly distributed around a mean of 137° with a circular variance of 0.54. The lineament

orientations in these chasmata are close to the mean corona orientations reported above. Most of these highlighted rifts are isolated from other rifts except for Kaygus Chasma, Mežas-Mate Chasma, and Mots Chasma, which share similar orientations. A few rifts are near montes, as seen in the BAT. Nang-Byon Chasma is north of Var Mons, and Olapa Chasma is northwest of Idunn Mons.

A large portion of Aphrodite Terra features rifts that trend East-West. Among the nine Chasmata that we mapped, Britomartis Chasma is located within Artemis. Its mean orientation is 39.9°, which is lower than the region's mean lineation orientation of 80.9°. The circular variance for this orientation distribution equals 0.5. The area surrounding Aphrodite Terra has fewer coronae and montes than the BAT.

By visual inspection, the rift orientations depend on their location, especially in the BAT and Aphrodite regions. At a global scale, rift lineaments exhibit a mean orientation of 111° and a circular variance of 0.73. These values fall within the calculated ranges for the coronae's interior and exterior outlines. Due to the high variance value, we tested the uniformity of the orientation distribution. We conducted statistical tests for uniformity, all of which indicated that the hypothesis of uniformity is rejected with 99% confidence. Like coronae, rift lineaments on Venus do not exhibit a uniformly distributed orientation.

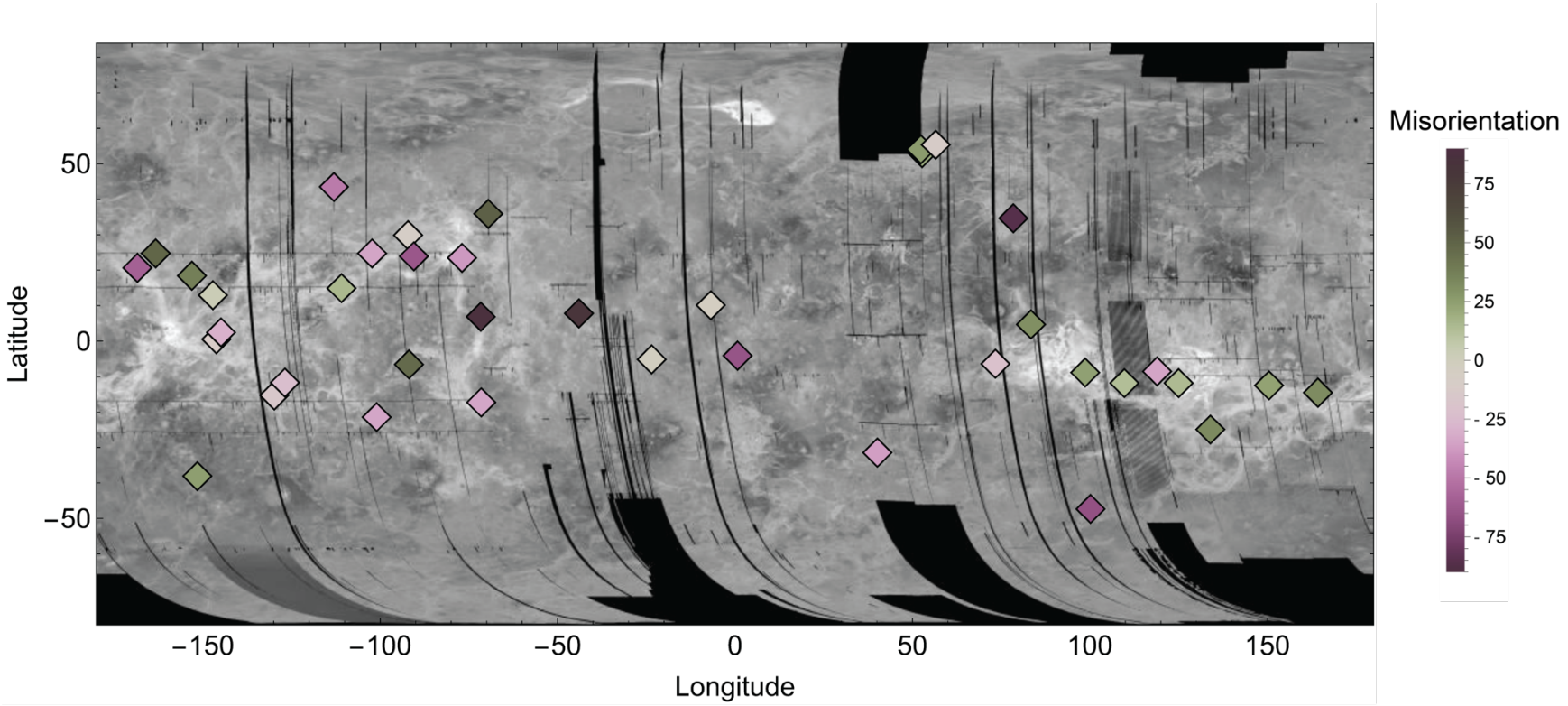


Figure 3-8: Map of rift misorientation. The color of each diamond corresponds to the misorientation, as indicated by the legend on the left. Initial results show that our highlighted regions (BAT, Aphrodite, and the Plains) exhibit a wide range of misorientation values, with the Plains displaying the largest misorientation values.

3.4.3 Misorientation Between Rifts and Coronae

To understand the relationship between the orientation of chasmata and coronae, we first collect the misorientation between each pair of chasma lineament (599 samples) and highly-elongated corona (232 samples) defined in Section 3.3.2, and average all the results that include a common lineament. In other words, we follow the procedure described in Section 3.3.3, with a lineament serving as the evaluation point, P and the coronae as the sampling points P_j. We present results here with a concentration factor $\kappa = 500$ so that the critical smoothing distance is comparable to the radius of our largest coronae. We only consider coronae with below-average circularity, as their orientation is determined more reliably than that of near-circular coronae. This strategy indicates how the global set of coronae is oriented compared to a given lineament. This approach is preferable to reversing lineaments and coronae, as the lineament database is less complete than that of coronae. In particular, it does not include chasmata outside the equatorial region. Finally, we averaged the misorientation of all the lineaments associated with a given chasma. Figure 3.8 and Table 3.3 presents the resulting chasma misorientation.

We mapped a total of nine chasmata in the Aphrodite region: Britomartis Chasma, Dali Chasma, Diana Chasma, Ix Chel Chasma, Jana Chasma, Kokomikeis Chasma, Kuanja Chasma, Ralk-Umgu Chasma, and Vir-ava Chasma. The mean misorientation for these chasmata is 16.1°. The rift with the highest misorientation, -34.6°, is Jana Chasma. The lineaments in Jana Chasma trend NW-SE compared to the more E-W orientation of the lineaments in other chasmata. Britomartis and Kokomikeis also feature high misorientation values of 32.9 ° and 30.8 °, respectively, and have rift lineaments that trend in a different direction, NE-SW, compared to the

regional trend. The rest of the chasmata have lower misorientation values, signifying that coronae in this region are more likely to be parallel to rifts that trend W-E.

Of our 39 mapped rifts, Artio Chasma, Dewi Ratih Chasma, Gui Ye Chasma, Heng-o Chasma, Kaygus Chasma, Kottravey Chasma, Mežas-Mate Chasma, Mist Chasma, Mots Chasma, Nang-Byon Chasma, Olapa Chasma, and Reitia Chasma are situated away from major rift systems. These 12 Chasmata have a misorientation range of -86.5 ° to 82°. The former value is associated with Kottravey Chasma, while the latter belongs to Nang-Byon Chasma. These chasmata are not close to one another: Nang-Byon is centered at approximately 40°W, 3°N, and Kottravey is located at 77°E, 30°N. They do share similar rift lineament orientations. However, Dewi Ratih Chasma, Gui Ye Chasma, Mist Chasma, Mots Chasma, and Olapa Chasma also exhibit rift lineament orientations similar to those above, albeit with lower misorientation values. In the case of these 12 rifts, there is no relationship between the original orientation of the rift lineaments and the calculated misorientation.

The BAT region contained the largest number of mapped rifts, totaling 18 chasmata: Aikhylu Chasma, Ardwinna Chasma, Chondi Chasma, Devana Chasma, Dziwica Chasma, Ganis Chasma, Hanwi Chasma, Hecate Chasma, Latona Chasma, Lesvka Chasma, Parga Chasma, Pinga Chasma, Rabie Chasma, Rona Chasma, Tkashi-Mapa Chasma, Zewana Chasma, Zverine Chasma, and Kicheda Chasma. The mean misorientation for this region is -18.4°. Between Alta and Themis regio, we see consistently low misorientation values, averaging- 22.7 ° (Figure 3.8). Atla regio displays higher misorientation, particularly for rifts near montes, such as Ardwinna

Chasma, Ganis Chasma, and Tkashi-Mapa Chasma. In the northeastern portion of the BAT, we observe low misorientation values, except for Zverine Chasma. The orientation of the lineaments inside this chasma changes by about 45° east and west of Kono Mons. These lineaments also have different orientations compared to the rest of the Chasma in this part of the BAT. Finally, the north-south trending portion of the BAT shows significant misorientation and a wide range of rift lineament orientations. Devana Chasma and Rona Chasma possess rift lineaments oriented N-S, but their misorientations are -38.6° and 86.8°, respectively. Just north of Devana Chasma lies Aikhylu Chasma, a chasma whose lineaments are oriented W-E and have a misorientation value of 52.3°. In the BAT region, coronae tend to be parallel along the NW and NE sections. Therefore, the N-S section of the BAT features a wide range of misorientation values.

The misorientation of individual lineaments is broadly distributed (Figure 3.9a). The mean misorientation and circular variance of rift lineament misorientation are -16° and 0.79, respectively. Moreover, this dataset contains two peaks: a narrow peak at 15 to 30° and a broader peak spanning -15 to -60°. Figure 3.9b shows the distribution of 39 chasma misorientation. This data range is restricted to ±60 °, with a mean misorientation of- 4.1 ° and a circular variance of 0.69. The peaks in lineament orientation distribution may also be present in the chasma orientation distribution, but stand out less.

Table 3-3: Summary of the misorientation calculation between Chasmata and Coronae

Name	Center Latutude	Center Longitude	Number of Lineaments	Average Misorientation (°)	Average Weighted Distance (km)	Average Weighted Circularity
Aikhylu Chasma	31.9	-69.5	10.0	52.3	1170.4	0.75
Ardwinna Chasma	20.7	-163.3	7.0	49.5	944.8	0.80
Artio Chasma	-35.4	40.1	10.0	-36.8	433.5	0.78
Britomartis Chasma	-28.9	134.0	14.0	32.9	1398.2	0.62
Chondi Chasma	-19.3	-129.8	9.0	-15.3	251.0	0.71
Dali Chasma	-18.5	164.3	25.0	32.5	534.7	0.73
Devana Chasma	19.5	-76.9	30.0	-38.6	737.3	0.75
Dewi Ratih Chasma	-8.1	0.7	60.0	-65.3	945.7	0.77
Diana Chasma	-16.5	150.5	18.0	23.6	333.9	0.69

Dziwica Chasma	-15.7	-126.8	13.0	-23.1	379.5	0.69
Ganis Chasma	16.6	-168.4	25.0	-59.2	1665.0	0.79
Gui Ye Chasma	-9.2	-23.5	10.0	-2.5	1046.6	0.79
Hanwi Chasma	10.9	-110.9	11.0	15.1	271.5	0.72
Hecate Chasma	20.7	-102.3	16.0	-34.6	565.5	0.67
Heng-o Chasma	6.1	-6.8	10.0	-4.2	1142.3	0.69
Ix Chel Chasma	-10.4	73.4	30.0	-20.9	1463.4	0.69
Jana Chasma	-12.5	118.9	10.0	-34.6	651.3	0.61
Kaygus Chasma	49.0	52.7	12.0	20.6	868.0	0.76
Kicheda Chasma	-3.5	-146.2	15.0	-11.1	526.5	0.76
Kokomikeis Chasma	0.7	83.4	13.0	30.8	1283.4	0.58

Kottravey Chasma	30.6	78.4	14.0	-86.5	1162.0	0.73
Kuanja Chasma	-12.9	98.7	12.0	24.2	914.0	0.61
Latona Chasma	25.9	-92.1	11.0	-8.6	1017.7	0.77
Lesavka Chasma	-1.5	-144.8	11.0	-29.8	331.2	0.74
Mezas Mate Chasma	50.1	52.4	11.0	26.5	953.3	0.77
Mist Chasma	39.5	-113.0	13.0	-48.6	980.1	0.77
Mots Chasma	51.4	56.6	11.0	-10.6	1214.3	0.77
Nang-byon Chasma	3.8	-44.0	11.0	82.3	984.9	0.80
Olapa Chasma	-42.1	-151.5	15.0	25.2	584.0	0.71
Parga Chasma	-25.4	-101.0	38.0	-34.3	409.3	0.76
Pinga Chasma	-21.3	-71.5	11.0	-34.3	291.2	0.76
Rabie Chasma	-10.6	-91.9	11.0	47.5	1058.6	0.72
Ralk umgu Chasma	-15.8	109.7	11.0	12.7	437.2	0.61

Reitia Chasma	-51.3	100.2	12.0	-66.7	424.7	0.68
Rona Chasma	2.9	-71.6	10.0	86.8	487.1	0.77
Tkashi-mapa Chasma	14.4	-153.1	15.0	37.6	617.3	0.70
Vir-ava Chasma	-15.8	125.0	13.0	14.2	1114.6	0.62
Zewana Chasma	8.9	-147.1	10.0	2.8	506.4	0.78
Žverine Chasma	19.9	-90.5	11.0	-64.4	1012.3	0.69

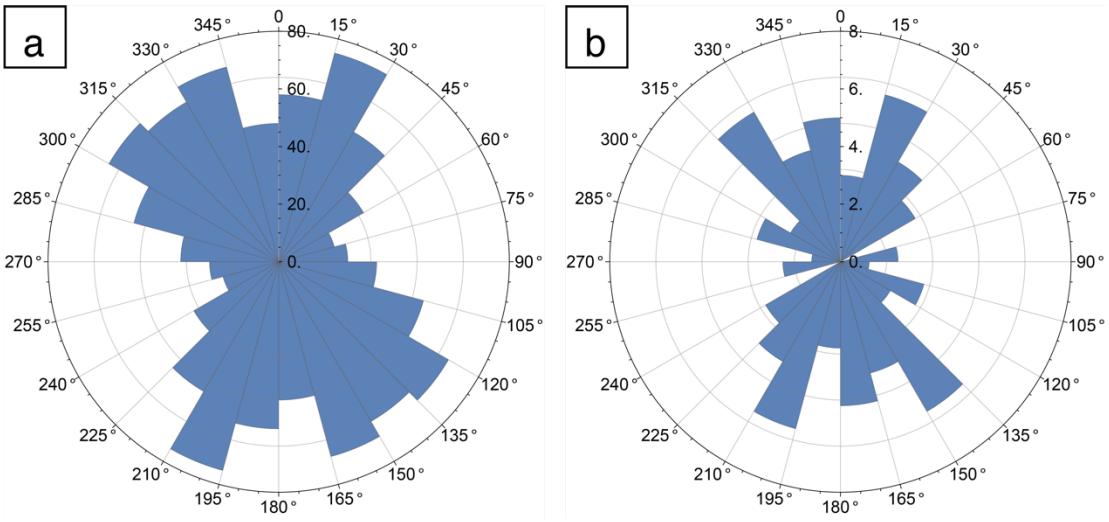


Figure 3-9: Rose diagrams showing misorientation for each chasmata lineament (a) and the average misorientation for each rift (b). We calculated the misorientation for 599 chasmata lineaments, which were then used to compute the average misorientation of each of the 39 mapped rifts.

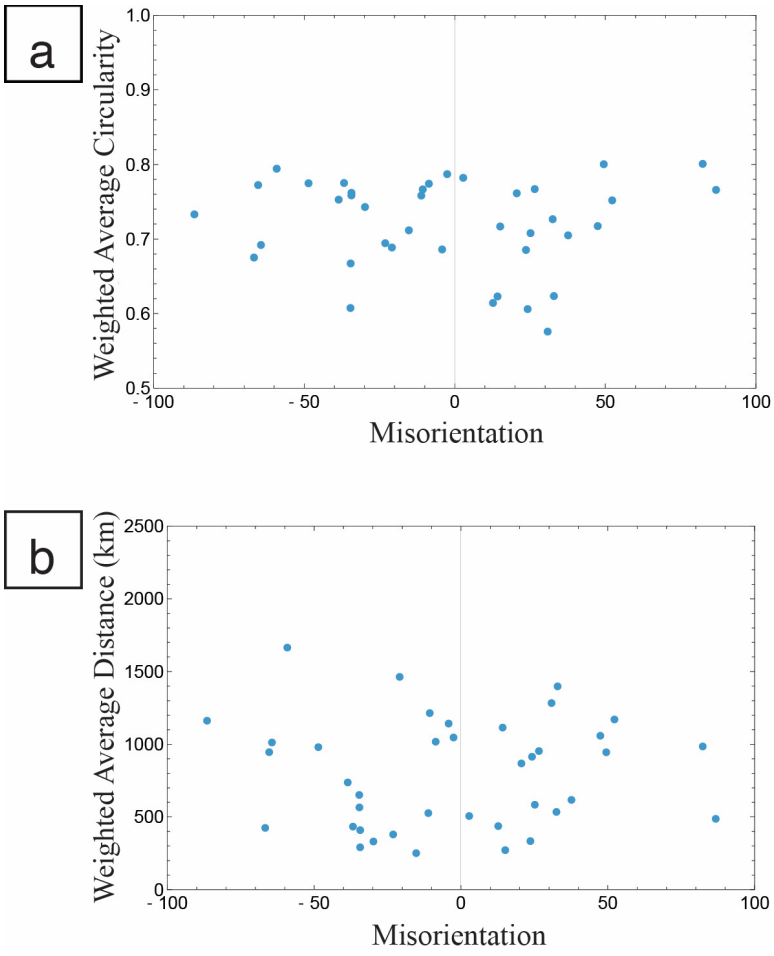


Figure 3-10: (a) weighted average corona circularity and (b) weighted average corona distance versus rift misorientation. Each point represents one of the 39 rifts we mapped.

We calculated a weighted circularity and distance between rifts and coronae using equations 3.18 and 3.19. In Figure 3.10, we compare these results to the misorientation of each rift. We find that rifts have lower misorientation values when coronae have a weighted circularity of 0.65 or lower (Figure 3.10a). Six rifts meet these criteria: Kokomikeis Chasma, Kuanja Chasma, Vir-ava Chasma, Ralk-Umgu Chasma, Jana Chasma, and Britomartis Chasma. All of these rifts are located in the

western portion of Aphrodite Terra. Figure 3.10b hints at the presence of a critical distance below which misorientation is low. When coronae are less than 600 km away from rifts, the misorientation range is restricted to ±35. Two rifts contrast with this observation: Reitia Chasma and Rona Chasma. Reitia Chasma is located south of Aphrodite Terra, while Rona Chasma is located between Beta and Themis Regio. Rona Chasma and Reitia Chasma have misorientation values of 86.8 ° and- 66.7 °, respectively. Our results indicate that chasmata with numerous coronae located less than 600 km away and with low circularity are more likely to exhibit low misorientation values.

3.5 Discussion

We determined that the global coronae population exhibits a non-uniform orientation distribution, suggesting that a mechanism must regulate the orientation. Spatially, we do not observe any global orientation patterns, indicating that a global process may not govern the shape of coronae. Squyres et al. (1992) proposed that elongated coronae could form via a diapir moving laterally with respect to the lithosphere. Our results show too much spatial variability in our orientation data to support this explanation. Pronin and Stofan (1990a) reached a similar conclusion with a smaller dataset.

We tested how other morphological characteristics may influence the orientation of coronae. We found that the orientation of coronae is not dependent on area or circularity. Many proposed formation mechanisms for coronae rely on the principle that the size of the diapir (Janes et al., 1992; Magee Roberts & Head, 1993; Koch & Manga, 1996), the impinged plume (Smrekar & Stofan, 1997), or the

magmatic intrusion (Dombard et al., 2007) is approximately the same, or at least related to (Gülcher et al., 2020) the diameter of the coronae. Our results show that orientation is not dependent on size, implying that the stresses affecting the shape of coronae are consistent across all diameters. Small coronae with small diapirs, intrusions, or plumes will experience the same stresses as larger coronae. Our results do not indicate a threshold at which the area of a corona determines its orientation. This is similar to the findings of Glaze et al. (2002), which show that Type 1 and Type 2 coronae are indistinguishable by diameter and should thus be treated as one population. Our coronae orientation data should be considered a single population influenced by a singular process. We argue that the formation mechanism for coronae must be sensitive to regional stresses regardless of size.

When we repeated our analysis of chasmata, we found that chasma lineaments have regional orientations. We identified these three regions as the BAT, Aphrodite Terra, and the Plains. We further divided the BAT into three sections. The region with the most consistent orientation among chasmata was the southern portion of the BAT. In our spatial analysis of chasmata orientations, we found examples where lineaments had orientations influenced by the presence of a mons.

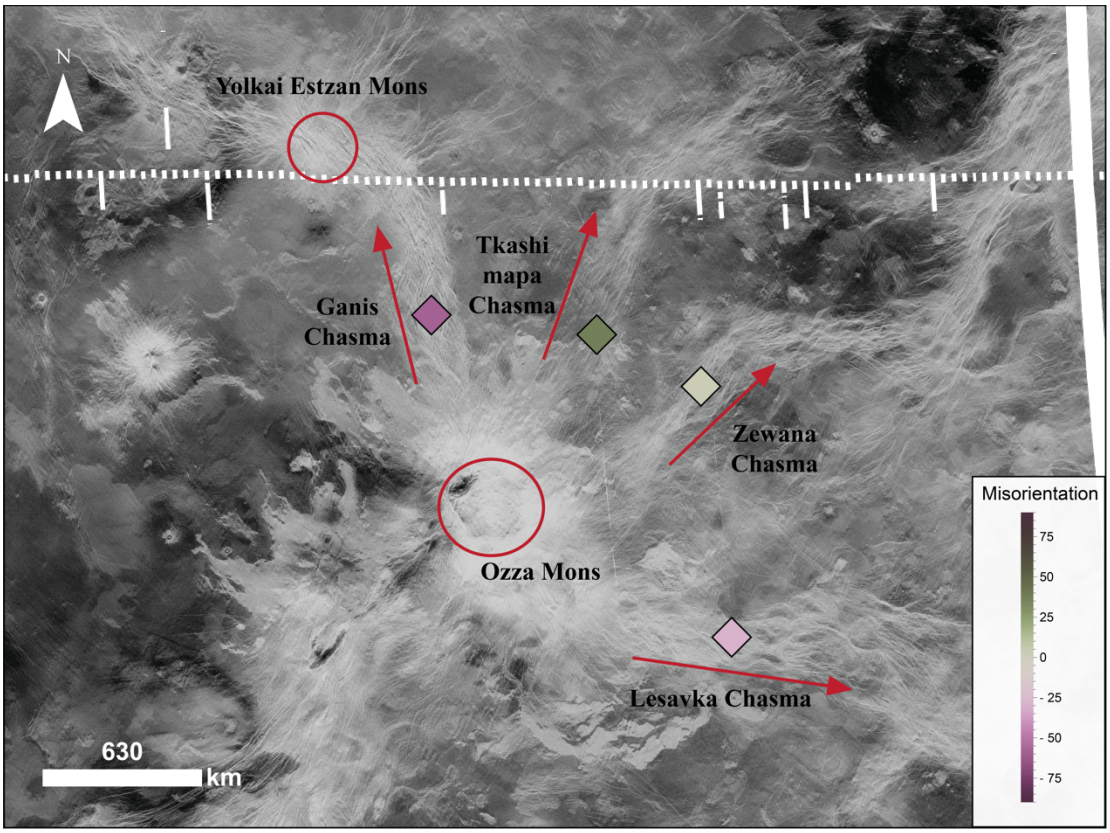


Figure 3-11: Radar mosaic of Ozza Mons and the rifts in its vicinity. Ozza Mons is part of the BAT near Alta Regio. Several rifts radiate from the Mons. Lesavka Chasma has a similar orientation to the chasmata located in the southern portion of the BAT, while the other chasma do not. The diamonds show the misorientation for each of the rifts.

The rifts located near Ozza Mons provide such an example. A close-up image of this region (Figure 3.11) shows that four chasmata radiate from Ozza Mons. Their orientation appears to curve further away from the center. These characteristics are similar to dikes, whose orientation changes depending on their proximity to their reservoir (Ernst et al., 1995). Stratigraphically, Senske et al. (1992) showed that rifting occurred contemporaneously with volcanism in the area, supporting the theory

that the orientation of rift lineaments can be affected by the emplacement of mons. Recent work has shown that this area of the BAT is a possible candidate for plume head stage, which could promote the creation of a local stress field that affects the surrounding features (El Bilali et al., 2023).

We used the orientation of the rift lineaments as an indicator of the regional stresses in which they formed. Following previous studies, we consider that chasmata are located in regions defined by extensional stresses (Campbell et al., 1984; Stofan et al., 1989; Hamilton & Stofan, 1996; Graff et al., 2018). Our results show that coronae are elongated in the same orientation as the strike of chasmata, which is the direction of maximum compressional horizontal stress. Coronae could become elongated because their emplacement process responds to stress, they follow lithospheric heterogeneities, or they are deformed after emplacement. The third hypothesis can be ruled out, as it would result in misorientation values close to ±90°. The other two hypotheses are harder to differentiate, as the tensile stress regime that may influence corona formation is also responsible for the development of structures at the base of the lithosphere and within it that could guide later corona development. However, previous studies have documented examples where chasmata and coronae developed simultaneously (Baer et al., 1994; Martin et al., 2007). While this does not rule out the importance of pre-existing features, given the possible long-lived character of rifts, it favors the hypothesis that coronae and chasmata are sensitive to the same stress regime. In other words, corona elongation is related to the regional stress field.

Of the three regions we identified as having preferred orientations, Aphrodite Terra contains the lowest misorientation range. This region is part of the equatorial

highlands, which include the BAT. Previous studies have characterized Aphrodite as having different stress zones: eastern Aphrodite contains little to no evidence for tensile horizontal tectonism (Hansen & Phillips, 1993), while western Aphrodite is dominated by extensional spreading (Head & Crumpler, 1987). If this were true, we would expect higher misorientation values for rifts located in eastern Aphrodite. However, our results show a consistent misorientation across all of Aphrodite. We conclude that Aphrodite Terra experienced a consistent tensile tectonic environment at the time of corona emplacement.

In the BAT, our misorientation values are low at rifts that are part of a more extensive system, such as the Alta-Themis section. This region has shown evidence of older and younger rifts following similar trends (Basilevsky & Head III, 2000). This illustrates that throughout the history of this region, features have formed in similar orientations. The highest misorientations occur in areas where the local stress fields are affected by the emplacement of Ozza Mons, as seen in Figure 3.11. In this case, rift lineaments are likely influenced by a local stress field linked to the mons, which can lead to significant differences from the regionally-controlled corona orientation.

No systematic misorientation pattern could be identified for chasmata located outside of the BAT and Aphrodite Terra regions. Plains on Venus are associated with thick effective elastic thicknesses (Jiménez-Díaz et al., 2015), an older relative age compared to chasmata (Ivanov & Head, 2011), compressional deformation (Bilotti & Suppe, 1999; McGill et al., 1981), and probably mantle downwellings at present (Bindschadler et al., 1992). The emplacement of coronae in the plains predates the development of wrinkle ridges (Basilevsky & Head, 1997; McGill, 2004).

Nevertheless, the few chasmata located in the plains exhibit low misorientation values. Both kinds of features formed early in the plains' history and may reveal the stress regime before the more recent compressive regime.

Dombard et al. (2007)'s model for coronae formation best fits our observations. This model begins as a mantle plume whose head impacts the base of the thermal lithosphere. Decompression forms the partial melt pocket responsible for the formation of the coronae. This melt ascends through the lithosphere and crust, generating the surface signatures of the coronae. During this process, the type of stresses on the crust is crucial to the shape of the coronae. According to our results, we argue that the partial melt would be injected in the direction of maximum compressional horizontal stress. This would create the coronae orientations we have observed. This would also explain why regions with high compressional stresses exhibit higher misorientation values.

3.6 Conclusion

From the initial images of Venus, coronae have long been characterized as ovoid or elongated shapes. This study systematically measured the circularity and orientation of coronae to determine which factors could impact their shape and used rifts as stress indicators for orientation comparisons. With the digitization of the Field datasets (International Astronomical Union Working Group for Planetary System Nomenclature, 2024; Stofan et al., 1992a), we gathered new morphological information about 523 coronae on Venus. We measured the orientation and circularity of each corona and statistically determined that they exhibit a nonuniform orientation distribution despite a circular variance of 0.89. Their orientation is not influenced by

factors such as locality, area, or circularity. Additionally, we find that their circularity is not spatially influenced.

We selected 39 rifts in the equatorial region of Venus, measured the strike of their lineaments, and compared them to the orientations of coronae. Unlike coronae, rifts exhibit preferred regional orientations. The three regions studied were the BAT, Aphrodite, and the plains. The BAT contained three orientation subsets, each with narrow orientation distributions. The plains rifts showed the largest range of lineament orientations, with similar circular variance values of 0.5. The Aphrodite Terra region contained many chasmata oriented W-E, with some exceptions such as Britomartis Chasma. We applied the same statistical tests for uniformity to the rift lineament data and found that rift orientation is not uniformly distributed.

Our analysis has shown that chasmata exhibit low misorientation when coronae are situated less than 600 km away from the rift and have a weighted circularity of less than 0.65. In that case, the misorientation range is limited to ±35. Chasmata in the Aphrodite Terra region have lower average misorientation values compared to rifts located in the BAT and plains regions. On a global scale, the average misorientation value is -4.1°. We conclude that coronae located less than 600 km from rifts are essentially parallel to the rift azimuth.

This correspondence highlights the influence of regional stresses or preexisting structures on corona elongation. This may indicate that a rising diapir intrudes into the lithosphere preferentially in the direction of maximum horizontal compressive stress, or that melt injected in that direction as dikes controls corona elongation. Future formation models of coronae should consider the roles of regional

and local stresses on diapiric rise and plume-lithosphere interaction. Future orientation analysis should consider the relative ages of rifts to determine if specific rift orientations serve as markers for any evolving stress field on Venus. Age differences might explain why we observe rifts with different orientations in similar locations, such as in Beta Regio. We hope our analysis of rift and corona orientations can enhance our understanding of Venus' internal dynamics.

Chapter 4. Calderas As Markers for Determining Magma Chamber Geometry

4.1 Abstract

The morphology of calderas on Earth is thought to be determined by the size, depth, and geometry of their magma chambers. In this study, we aim to investigate the emplacement of caldera magma chambers by developing a new caldera morphology database. We mapped 57 calderas and calculated their orientation and elongation using a projection-agnostic method. We compared the orientations of the most elongated calderas to the world stress data from Heidbach et al. (2018). We find that many calderas are elongated perpendicular to the maximum horizontal compressive stress. We also find examples of calderas that elongated in the direction of preexisting fault structures. Our results show that the shape of calderas can be explained by the deformation of magma chambers by local stress or by the preferential injection of magma along regional preexisting fault structures.

4.2 Intro

Calderas are features created by the removal of magma during an explosive or effusive eruption. These volcanic events cause a near-vertical subsidence of the caldera floor into the magma chamber, resulting in a topographic rim. Because magma chambers are essential to forming calderas, many studies have been conducted to understand their relationship.

Roche et al. (2000) found through experiments that the style of collapse of calderas can be related to the depth and width of a magma chamber. They found that

shallow and wide magma chambers create piston calderas, while deep and small magma chambers form funnel calderas. An analytical study using the Coulomb failure criterion was able to independently confirm these results (Kusumoto & Takemura, 2005). A different experimental study showed that elongated reservoirs could create elongated depressions, with a similar morphology to calderas (Marti et al., 1994). Kennedy et al. (2004) showed that the magma chamber's tilt and depth can control the symmetry and elongation of calderas. From these studies, it is proposedthat a magma chamber's width, depth, and geometry can control the morphology of calderas.

In this study, we developed a caldera database that includes new morphological measurements, like orientation and elongation. With the stress measurements from the World Stress Map by Heidbach et al. (2018), we directly compared the orientation of calderas to stress measurements. Our results show that calderas are perpendicular to the direction of maximum horizontal stress. To match the observed observations, the magma chamber beneath the caldera must be deformed by the local stresses. We also see evidence of the caldera's shape being determined by the orientation of regional preexisting features.

4.3 Methods

4.3.1 Calderas and Stress Measurements

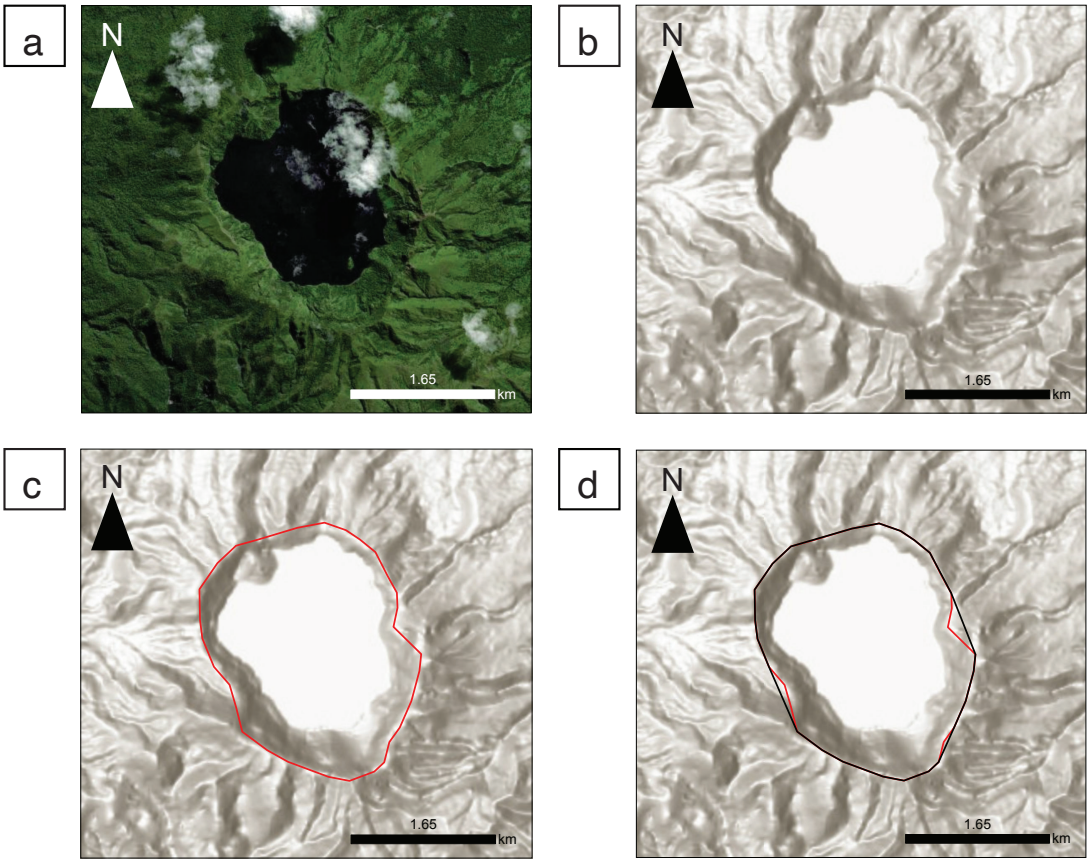


Figure 4-1: Mapping of Billy Mitchell Caldera in Papua New Guinea. Mapping was conducted using hill shape basemaps (b), as satellite imaging (a) made locating the rim challenging. The rim of the caldera was outlined (c), after which the minimum bounding tool was employed to determine the convex hull (d).

We selected calderas that were located in the Global Volcanism Program & Venzke (2024) Holocene and Pleistocene volcano databases. A total of 173 features are defined in these databases as having a volcano landform and a primary volcano type of caldera. We mapped the 57 calderas from this dataset that feature well-defined, topographically positive rims in a hill-shade basemap (Figure 4.1) that we

can have a reliable estimate of the caldera wall outline. Calderas were mapped at different scales depending on their diameter. The smallest and largest scales we used were 1:8,000 (Asoson Caldera) and 1:500,000 (Toba). Using our mapped outlines (Figure 4.1c) as inputs, we run the minimum bounding geometry tool in ArcGIS to find the convex hull for each caldera (Figure 4.1d).

Following the procedure described in Chapter 3, the convex hull shape files are analyzed through a MATLAB script to calculate all calderas' orientations, as well as their short and long axes, independent of projection. This script begins by calculating the distance between every pair of vertices that define the convex hull and identifies the pair of vertices separated by the longest distance, which defines the long axis. The azimuth of this axis serves as a proxy for the orientation of the entire caldera with respect to north. The distances from all other vertices to the axis are then used to define the length of the short axis (Chapter 3). Using these values, we define the circularity of the calderas as the ratio of the short to long axes. Elongation is traditionally defined as the inverse of this circularity, but circularity has the advantage of remaining bounded between 0 and 1. A highly elongated object has a circularity near 0, whereas a perfect circle has a circularity of 1.

Each stress measurement is taken from Heidbach et al. (2018). These stress measurements are ascribed a quality rating between A and F. We only retain values with a rating higher than C because anything lower is unreliable. Additionally, we only used stress measurements that were derived from the following sources: earthquake focal mechanism, borehole breakouts, and hydraulic fracturing. Additional stress orientation measurements in the database rely on geologic structures

such as geologic vent alignments. We ignore them as they may not be independent of the shape of the calderas examined here. Other stress sources, like strain recovery and shear wave splitting, have too low a quality to be reliable. The orientation reported for the stress measurements corresponds to the azimuth of the maximum horizontal compressive stress in degrees. We also filtered the data to ensure the orientation values ranged from 0 to 180° because there were some data that had an orientation of 999°. A total of 31,198 stress measurements were used in our analysis.

4.3.2 Circular Statistics

As defined in Chapter 3, misorientation is the angle between a measurement and a small circle parallel to a reference datum. In the application below, calderas serve as reference points. Therefore, we calculate the extent to which individual stress measurements are misaligned compared to the orientation of a given caldera. We cannot reverse this procedure and obtain a misorientation of caldera with respect to a given stress measurement because our database of calderas, which is limited to those that feature a well-defined topographic rim, comprises only 32.9% of the calderas in Global Volcanism Program & Venzke (2024) database. Misorientation is restricted to the range [-90°, 90°], where perfect alignment is at the center of this range. Since orientation is a non-directed axis, there is a 180° ambiguity associated with all orientation and misorientation measurements.

The average misorientation associated with a given caldera is obtained by averaging all the stress misorientation values referred to that caldera. This value indicates whether the caldera's orientation is comparable to that of the nearby stresses.

In order to emphasize the nearest stress measurements, the averaging uses a series of weights $W(P, P_i)$, where P indicates a given caldera and $\{P_i\}$ is the set of n stress measurements. The weights are modeled after a Fisher distribution, causing the weight to dissipate as a standard Gaussian function but on a sphere.

$$W(P, P_i) = \frac{\kappa}{4\,\pi \sinh \kappa}\, e^{\kappa(x x_i + y y_i + z z_i)} \tag{4.1}$$

Where κ is the concentration parameter, which determines how the weight falls off with distance. By analogy with the properties of a Gaussian distribution, we relate κ to a physical fall-off distance (see Chapter 4) that, on Earth, is given by

$$D_{\text{Earth}} = R_{\text{Earth}}\, \cos^{-1}\left(1 - \frac{1}{\kappa}\right) \tag{4.2}$$

where R_{Earth} is the radius of the Earth, 6378 km. For our analysis, we have chosen a $\kappa = 500$. This is equivalent to a distance on Earth of 403 km. This distance represents visually a length scale over which stress measurements are consistent. For this same reason, Heidbach et al. (2018) generated smoothed stress fields using a search radius of 500 km, comparable to our chose fall-off distance.

We use the weight function first to calculate the average distance between calderas and stress measurements:

$$\overline{D} = \frac{\sum_{i=1}^{n} D_i \times W(P, P_i)}{\sum_{i=1}^{n} W(P, P_i)} \tag{4.3}$$

Finally, we calculate the weighted misorientations at each caldera

$$\bar{\theta} = \frac{1}{2}\, \text{atan}\left(\frac{\sum_{i=1}^{n} \sin 2\theta_i \times W(P, P_i)}{\sum_{i=1}^{n} \cos 2\theta_i \times W(P, P_i)}\right) \tag{4.4}$$

The orientation averaging follows the calculation of a circular mean for non-directed axial data, with the addition of the weight $W(P, P_i)$. The orientation data is

doubled before averaging to remove the 180° ambiguity inherent to axial data, and the results divided by two for the same reason (Mardia & Jupp, 2000).

4.4 Results

4.4.1 Caldera Orientation and Circularity

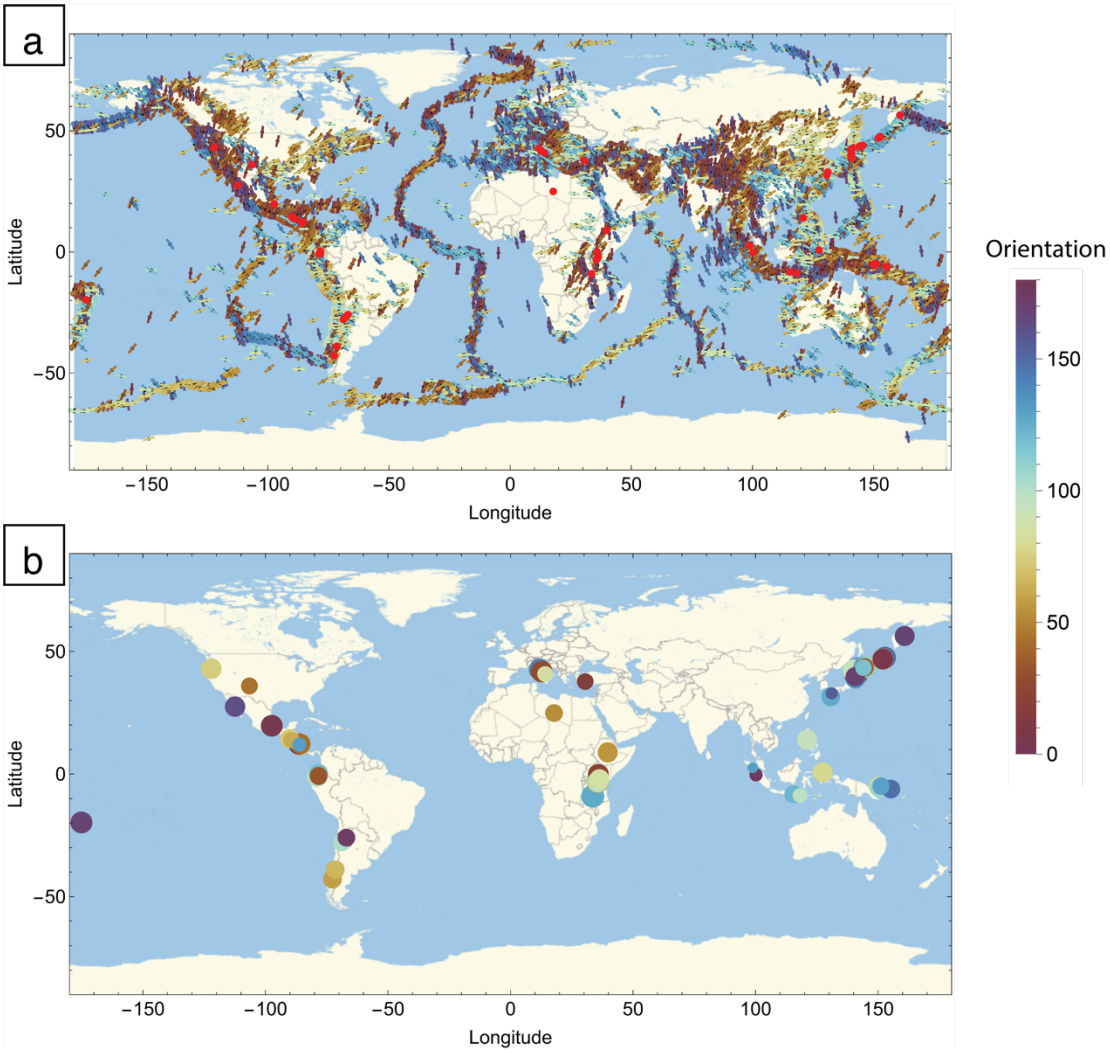


Figure 4-2: Stress (a) and caldera (b) orientations. In the stress map (a), the red dots represent the locations of the 57 mapped calderas. Most of the stress measurements on the map have a C quality (91.5% of all stress measurements). We only mapped the

calderas in the Global Volcanism Program & Venzke (2024) dataset that feature a well-defined rim (32.9% of the all calderas).

Our 57 mapped calderas are located in three types of tectonic settings: subduction zones, continental rifts, and intraplate. Most of these calderas (48) are located along subduction zones (Figure 4.2b), six are along the East African rift system, and the remaing three are intraplate: Los Humeros (Mexico), Waw an Namus (Libya), and Valles Caldera (United States). Most calderas were located in regions with a high number of stress measurements. Only one caldera Waw an Namus, is in a region without nearby stress measurements (Figure 4.2a). The average stress measurement distance for this caldera is 880.304 km (Table 4.2). As most stress estimates in the World Stress Maps are constrained by earthquake focal mechanism, the absence of nearby stress reflects how tectonically quiet this location is. The other two intraplate calderas are in regions with local stress values ($\overline{D}$ =394.9 km (Los Humeros) and 416.2 (Valles Caldera)).

Table 4.1 presents the results of our measurements. There does not appear to be global spatial variations of caldera orientations (Figure 4.2b). Along the East African rift system, the orientations of calderas range from 21 to 127°. All the regions we mapped feature a large range of misorientation values. At the Nazca and South American plate boundary, the range of orientations is 142°. There is not one region where calderas have a preferred orientation. Because we mapped so few calderas, we cannot confidently compare the various types of plate boundaries. However, of the calderas we mapped, those in an extensional tectonic regime have similar orientations

to those in a compressive tectonic regime. The circularity of calderas has the same result. No region on earth is more likely to have more circular or elongated calderas.

Table 4-1: Characteristics of the 57 mapped calderas, ordered by decreasing circularity. Plate boundaries abbreviation: PPA: Pacific and North American Plates, AFS: African and Somalian Plates, AE: African and Eurasian Plates, AP: Australian and Pacific Plate, CC: Cocos and Caribbean Plates, NS: Nazca and South American Plate, JNA: Juan De Fuca and North American Plates, CCNA: Coco and North American Plates, EPH: Eurasian and Philippine Plates, AUE: Australian and Eurasian Plates, and None: Intraplate. The area was calculated in ArcGIS using a conic equal-area projection and is in km^2. The latitude and longitude are in decimal degrees. The calderas below the line separating Cuicocha and Ayarza are calderas are considered highly elongated.

Name	Latitude	Longitude	Nearest Plate boundary	Area	Orientation	Circularity	Average misorientation	Average stress distance
Shikotsu	42.7	141.4	PPA	1.35	144.82	0.99	-36.4	373.8
Towada	40.5	140.9	PPA	107.36	30.12	0.99	80.2	325.9
Nigorikawa	42.1	140.4	PPA	5.62	93.52	0.98	14.0	386.4
Ngozi	-9.0	33.6	AFS	7.83	126.74	0.97	43.7	279.1
Olmoti	-3.0	35.6	AFS	33.24	64.16	0.96	-11.5	225.9
Kussharo	43.6	144.4	PPA	222.53	126.69	0.93	-12.6	366.9
Tofua	-19.8	-175.1	AP	24.43	169.08	0.92	-57.9	303.7
Ushishur	47.5	152.8	PPA	1.88	149.90	0.92	-30.1	223.6

Vulsini	42.6	11.9	AE	208.97	143.12	0.92	8.4	288.4
Los Humeros	19.7	-97.4	NONE	243.81	4.39	0.92	16.4	394.8
Tomariyama	43.9	145.5	PPA	17.03	110.03	0.91	6.5	372.9
Coli Albani	41.8	12.7	AE	4.82	26.59	0.91	-59.2	313.0
Apoyo	11.9	-86.0	CC	34.44	68.43	0.90	-42.6	279.3
Zavaritzki[2]	46.9	152.0	PPA	41.59	53.16	0.90	67.2	228.7
Apoyeque	12.2	-86.3	CC	5.96	174.16	0.89	30.7	282.3
Kilombe	-0.1	35.8	AFS	7.70	21.33	0.88	32.9	374.0
Quilotoa	-0.9	-78.9	NS	6.26	99.15	0.88	-16.1	311.0
Crater Lake	42.9	-122.1	JNA	66.03	74.49	0.87	-70.6	418.9
Ngorongoro	-3.2	35.6	AFS	318.50	77.86	0.87	-26.5	233.1
Embagai	-2.9	35.8	AFS	37.82	98.40	0.87	-44.7	217.7
Zavaritzki[1]	46.9	152.0	PPA	7.85	5.43	0.86	-65.0	229.0
La Reforma	27.5	-112.4	CCNA	102.24	162.51	0.86	14.4	290.7
Lajas, Las	12.3	-85.7	CC	30.07	42.78	0.85	-17.1	308.9
Taal	14.0	121.0	EPH	3.19	94.03	0.84	-7.0	368.0
Kone	8.8	39.7	AFS	25.49	55.66	0.84	87.9	439.2
Zarechny	56.4	160.8	PPA	13.66	168.05	0.84	-31.0	331.8
Telaga	0.7	127.4	EPH	3.38	77.99	0.84	27.0	267.7
Lenderut	-2.1	36.3	AFS	41.98	84.63	0.83	-27.1	253.8

Onikobe	38.8	140.7	PPA	61.78	132.57	0.83	-18.3	292.2
Tazawa	39.7	140.7	PPA	44.45	170.15	0.81	-58.3	316.6
Cuicocha	0.3	-78.4	NS	7.51	119.13	0.81	-39.8	350.5
Ayarza	14.4	-90.1	CC	28.20	72.81	0.80	-49.6	286.0
Dakataua	-5.1	150.1	AP	92.28	81.00	0.80	-35.1	266.6
Witori	-5.6	150.5	AP	32.03	106.90	0.80	-64.8	253.2
Chaiten	-42.8	-72.7	NS	6.88	58.68	0.79	22.7	430.5
Aira	31.6	130.7	EPH	0.41	126.49	0.79	-31.0	318.7
Sollipulli	-39.0	-71.5	NS	11.91	65.63	0.78	22.0	324.3
Billy Mitchell	-6.1	155.2	AP	5.28	148.64	0.78	70.3	245.5
Mashu	43.6	144.5	PPA	31.88	37.35	0.77	77.1	364.7
Cerro Blanco	-26.8	-67.7	NS	23.26	25.74	0.75	64.9	442.8
Batur	-8.2	115.4	AUE	101.40	121.83	0.75	32.8	354.8
Chalupas	-0.8	-78.3	NS	221.07	32.53	0.75	51.5	311.1
Incapillo	-27.9	-68.8	NS	21.42	102.12	0.75	-11.9	407.9
Waw an Namus	24.9	17.8	None	9.55	52.54	0.75	-73.2	880.3
Cerro Galan	-26.0	-67.0	NS	815.39	174.32	0.74	-83.7	465.0
Lolobau	-4.9	151.2	AP	0.68	129.49	0.73	-84.3	240.7
Valles Caldera	35.9	-106.5	None	447.58	44.39	0.71	-48.5	416.2

Golcuk	37.7	30.5	AE	12.35	16.10	0.70	-80.9	331.9
Akan	43.4	144.0	PPA	0.25	117.47	0.69	-4.2	358.2
Ilopango	13.7	-89.0	CC	68.41	58.08	0.67	-36.2	296.0
Campi Flegrei	40.8	14.1	AE	79.18	83.30	0.67	60.8	325.7
Coatepeque	13.9	-89.6	CC	56.78	61.59	0.67	-39.3	289.5
Tarowa	-8.7	118.2	AUE	17.14	96.90	0.63	68.1	266.0
Masaya	12.0	-86.2	CC	52.87	131.29	0.59	74.3	277.7
Maninjau	-0.3	100.2	AUE	223.99	176.50	0.56	41.8	316.5
Asosan	32.9	131.1	EPH	0.36	156.21	0.50	-62.9	335.9
Toba	2.6	98.8	AUE	2745.70	130.30	0.45	87.2	334.4

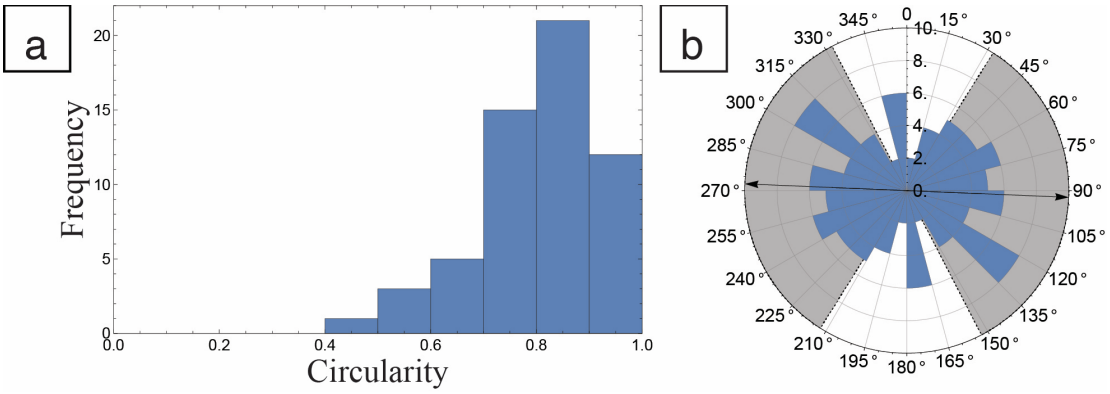


Figure 4-3: Distribution of circularity (a) and orientation (b) of the 57 mapped calderas. Orientation values are mirrored in the rose diagram (b) because the data has an ambiguity of 180°. The gray portions zones and arrow in (b) correspond to the data's standard deviation and mean orientation.

The distribution of our caldera circularity has a narrow peak around the mean circularity value of 0.81. The distribution is skewed towards circular calderas (Figure 4.3a). Due to a lack of systematic spatial variations, we created a rose diagram of caldera orientations (Figure 4.2b). Caldera orientation is rather broadly distributed around a circular mean of 92° and a peak in the 120-130° orientation bin. We used three statistical tests to determine if the distribution is non-uniform. The χ^2- goodness of fit, modified Kuiper, and Rayleigh tests each have a null hypothesis of uniformity (Mardia & Jupp, 2000). We cannot reject the null hypothesis in any of our three tests. Therefore. we conclude that the orientation distribution of our mapped calderas is uniformly distributed.

4.4.2 Misorientation

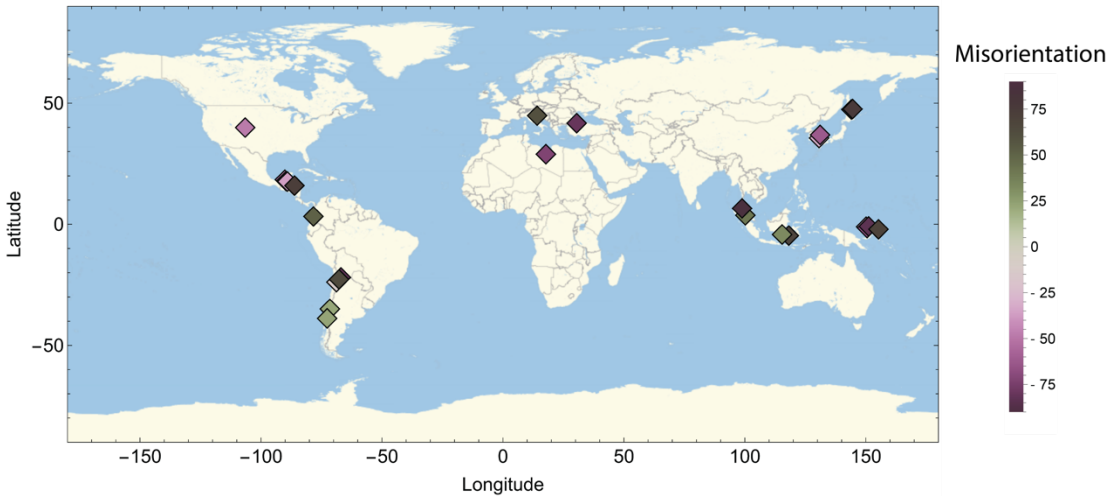


Figure 4-4: We calculate a weighted average of 31,198 misorientation values for below-average circularity calderas to determine a weighted average misorientation. These values are represented by the color of each diamond on the map.

We report misorientation only for calderas with below-average circularity. Due to their shape, more circular calderas would exhibit higher orientation uncertainty than their more elongated counterparts. The 26 calderas that meet this criterion can be found below the dividing line in Table 4.1. By excluding circular calderas, we eliminated all calderas located in the East African rift system. This leads to our misorientation becoming a comparative analysis of various subduction zones. We calculated the misorientation between individual calderas and all stress measurements. Therefore, each selected caldera serves as a reference for 31,198 globally distributed misorientation values, although the weighting scheme (Equation 4.4) indicates that only stress measurements obtained less than a few hundred kilometers from the caldera significantly contribute to the misorientation average.

Here again, we find no geographical pattern in the misorientation data, although we note that most calderas have a high misorientation (dark colors on Figure 4.4). The elongated calderas used in our analysis are in seven major subduction zones: the Middle America trench, the Chile-Peru trench, the Hellenic subduction zone, the Sunda subduction zone, the New Britain trench, the Nankai trench, and the Kuri Kamchatka trench. We do not see consistent or preferred misorientation in any of these zones. For example, in the Chile-Peru trench region, we observe calderas that are very close to each other but have differing misorientation values (Figure 4.4). It does not appear that subduction zones exhibit a preferred misorientation. We find that regionally, the misorientation of calderas with respect to local stress measurements is varied and not systematic.

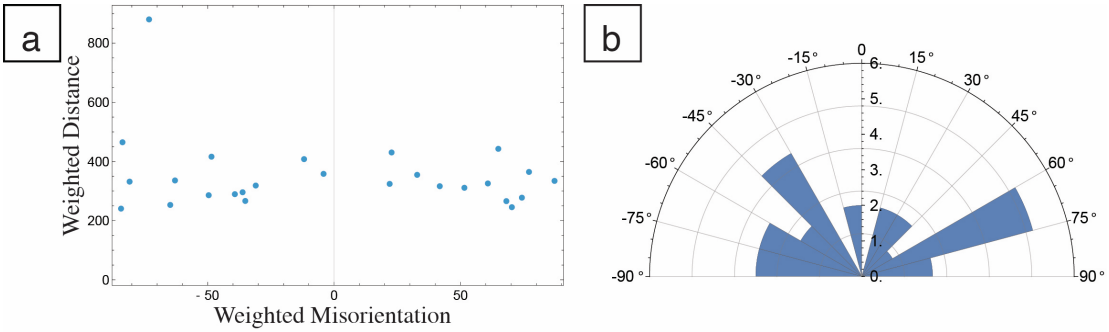


Figure 4-5: a) Relationship between distance-weighted average misorientation and distance-weighted average distance between calderas and the stress measurements (a). We used equation 4.3 to calculate the weighted average distance. b) Distribution of the distance-weighted average misorientation. These results consider only higher elongated calderas, which have a circularity less than 0.81.

We compared the weighted average misorientation to the weighted average distance between the caldera and the stress measurements. Figure 4.5a shows that

calderas closer to the stress measurements are more likely to be perpendicular to the stress value. We also observe in our misorientation distribution (Figure 4.5b) a dominant peak around 60 to 70° and a secondary peak at -45 to -30°. Few calderas have a misorientation close to 0°. We conclude that calderas are more likely to be perpendicular to the local maximum horizontal compressional stress.

4.5 Discussion

Our preliminary result that calderas are perpendicular to the maximum horizontal compressive stress agrees with many analog experiments (Acocella, 2007; Holohan et al., 2005)and an observational study (Bosworth et al., 2003). Bosworth et al. (2003) studied calderas in Iceland, Kenya, and Western America, none of which were in our study, yet our conclusions were the same.

This relationship between local stress and calderas may point to the deformation of magma chambers. Magma chambers can be treated as a soft inclusion when it is partially molten or solidified but still hot (Gudmundsson, 2012). This property may allow for the deformation of the chamber in a local stress environment. In a compressive stress regime, we expect deformation to occur perpendicular to the maximum horizontal compressional stress. Studies have shown that the shape of a magma chamber determines the shape of a caldera ((Kennedy et al., 2004; Kusumoto & Takemura, 2005; Marti et al., 1994; Roche et al., 2000)), therefore a magma chamber elongated perpendicular to the maximum horizontal compressive stress would create a caldera in the same direction.

Many calderas are nearly perpendicular to the maximum horizontal compressional stress, but many have a misorientation of -30 to -45° (Figure 4.5). We

want to go beyond the stress measurements to investigate how some aspects of the local geology could explain these orientation values. This section analyzes in more detail three regions: the Middle-America subduction zone in El Salvador, the South America trench in Northern Chile and Argentina, and the Sunda Trench at the island of Sumatra, which contain calderas with non-perpendicular misorientations, to understand what may cause the variability in caldera orientation.

4.5.1 Middle American Trench

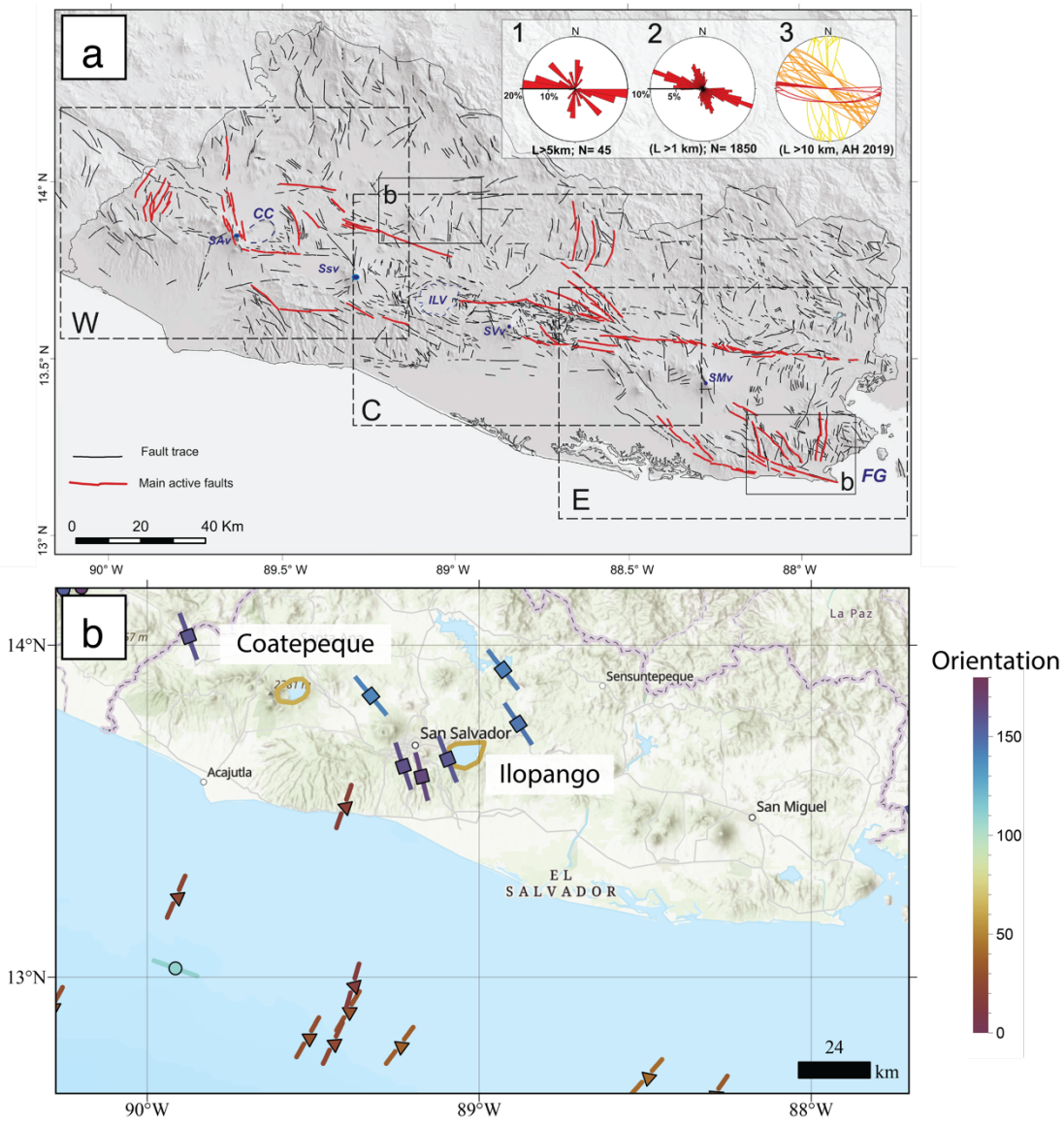


Figure 4-6: Fault map (a) and stress measurements (b) of El Salvador. Very few stress measurements are located in this area, and none are associated with the E-W strike-slip faults shown in (a). The calderas outlined in (b) are Coatepeque to the west and Ilopango to the east. The stress measurements and caldera outlines are colored according to their orientation. The circle, square, and triangle points correspond to normal, strike-slip, and thrust faulting regimes, respectively. The colors of the stress

measurements correspond to their orientation. Fault map taken from Martínez-Díaz et al. (2021).

Coatepeque Caldera and Ilopango Caldera are located in El Salvador, along the Middle-America subduction zone. They have similar misorientation of -39° and -36°, respectively. In Figure 4.6, most of the stress measurements in this region are offshore, at the subduction zone. These results do not provide a conclusive relationship between the stress field and the shape of the calderas, so we investigate the local tectonic regime. Coatepeque and Ilopango calderas are located along the El Salvador Fault system. This fault zone contains many strike-slip faults with ESE-WNW fault traces (Martínez-Díaz et al., 2021). Majority of the active faults, Figure 6a, surrounding the calderas are right-lateral strike faults. The fault regimes in this area were determined by the catalog of seismic events between 2016 and 2020 from the National Seismic Network of El Salvador (Martínez-Díaz et al., 2021). This can explain the low number of strike-slip measurements in this area from the Heidbach et al. (2018) dataset. Ilopango Caldera has an orientation of approximately 58° NE, while the surrounding faults have a strike of about 90°. The difference between the strike of the nearby faults and Ilopango is roughly 30 to 40°. This suggests that Ilopango is perpendicular to the maximum horizontal stress of the strike-slip faults, provided that the principal stress $\sigma_1$is 30 degrees from the fault trace. This indicates that the caldera is elongated in accordance with the strain from the strike-slip fault system. Coatepeque Caldera shares a similar orientation and could likewise be elongated by distributed strain in the region. The high misorientation is partly attributed to the averaging scheme that includes unrelated subduction-related stresses.

Saxby et al. (2016) found a negative density anomaly below Ilopango that is elongated perpendicular to the maximum horizontal stress of the faults in the region. This anomaly is also parallel to the caldera orientation. These authors have interpreted this anomaly as the magma chamber associated with the caldera. Studies have shown that magma chamber geometry controls the shape of calderas (Geshi et al., 2023; Gudmundsson, 2008). Thus, it follows that the shape of Ilopango is perpendicular to the direction of the maximum horizontal stress. This gravity analysis study supports our conclusion that the calderas in this region are shaped by the strain created by the strike faults in the Salvadoran Fault System, not the subduction zone..

4.5.2 Chile-Peru Trench

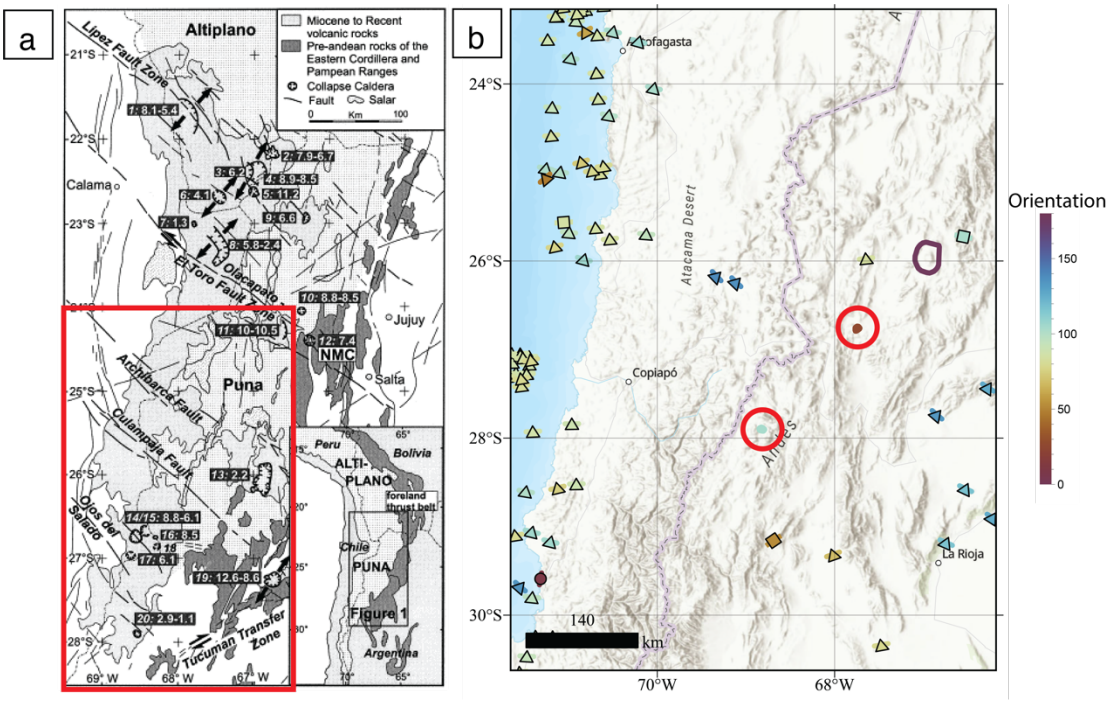


Figure 4-7: Calderas and faults in the central portion of the Nazca-South American subduction zone. a) Faults in the region. Note the system of faults with a NW-SE trace. The large red box indicates the area covered by b). b) Stress measurements,

color-coded according to their orientation, and the three calderas, from north to south, Cerro Gallan, Cerro Blanco, and Incapillo. The last two are marked by a red circle to make them easier to find. Most stress measurements are located along the Chile-Peru trench. Geological map from Riller et al. (2001).

Three calderas, Cerro Galán, Incapillo, and Cerro Blanco, are situated in the central part of the Nazca and South American subduction zone, along the northern border between Chile and Argentina. They are roughly 300 km apart, but their orientations vary significantly. The northernmost calderas, Cerro Galán and Cerro Blanco, exhibit a nearly north-south orientation of 174° and 25°, respectively, whereas Incapillo Caldera displays a near east-west orientation of 102°. This region is geologically complex and may not be accurately represented by the stress measurements in Figure 4.7.

Many of the measurements in this area are associated with thrust faulting due to the oblique subduction of the Nazca Plate beneath the South America Plate. One major fault system in this region is the Atacama fault system, which trends N-S along the coast of Chile. We do not expect the Atacama fault system to influence the shape of these calderas since they are located further east in Argentina, but other faults with similar orientations are present closer to the calderas.

Folkes et al. (2011) have shown that regional faults control the shape of Cerro Galán. These faults flank the caldera's eastern and western edges. Cerro Blanco is also located in a region with local north-south trending faults. These faults do not flank the caldera but are situated north and south of it. The World Stress Map

contains few stress measurements associated with these regional north-south striking faults.

Incapillo Caldera is surrounded by over 40 magmatic domes that formed before the caldera. Most of the domes are located to the west and east of the caldera. Goss et al. (2009) developed a model in which a common magma chamber serves as the source for both the domes and the caldera. The magma required to form the domes may have migrated along regional NW-SE trending faults. These NW-SE trending faults are part of a larger subparallel system interpreted to have a spatial relationship with other calderas (Riller et al., 2001). This could lead to a caldera aligning in the same orientation as the regional faults. Our calculated orientation value aligns with this observation. In this region, the orientation of preexisting faults may play a significant role in the shape of calderas.

4.5.3 Sunda Subduction Zone

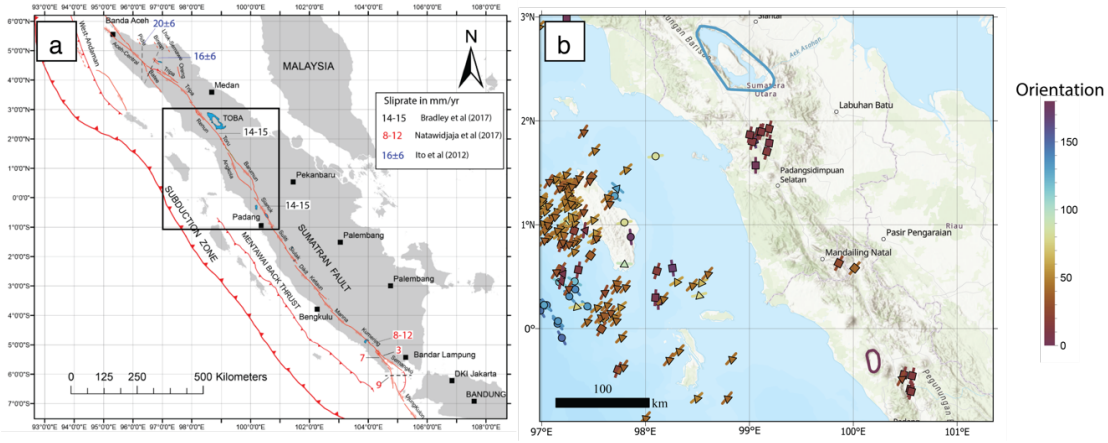


Figure 4-8: a) Fault map and b) stress measurements in Sumatra with the outlines of Toba Caldera (North) and Maninjau Caldera (South). The region shown in (b) corresponds to the black box in (a). The Sumatran fault has a consistent NW-SE

strike (a), with Toba exhibiting orientations of 130° and a misorientation of 87°, while Maninjau has an N-S orientation and a misorientation of 42°. The labels for the stress measurements follow the same scheme as in Figure 4.6. Fault map from Natawidjaja (2018)

We mapped the Toba and Maninjau calderas in Sumatra. Toba is by far the largest caldera mapped here. It is oriented along the Great Sumatran fault, with an elongation toward 130°. In contrast, the Maninjau Caldera is oriented nearly N-S. Only its northernmost portion intersects the fault trace. Most of the stress measurements in this area are in the Sunda Subduction Zone (Figure 4.8) and may be unrelated to the local stress field around the Sumatra fault.

From our misorientation calculation, the shape of Toba may be caused by the shear deformation created by the oblique subduction zone. Bellier & Sébrier (1994) proposed that the shape of Toba could be related to stepovers, similar to what is observed in the Ranau caldera in South Sumatra. A stepover would provide the mechanism for a potential magma chamber to become elongated in the direction of the fault trace. This does not apply to Maninjau Caldera because it does not follow the strike of the Great Sumatran fault. The closest stress measurements to Maninjau Caldera have an orientation of about 14 degrees, misoriented with the caldera by only about 20 degrees. Thus, we argue that Maninjau Caldera is elongated parallel to the maximum horizontal stress related to the fault trace. Deformation processes, like stepovers, shape calderas along the Great Sumatran Fault. However, those not along the fault trace are oriented along the fault's maximum horizontal compressional stress.

4.6 Conclusion

We have developed a new global map of elongated calderas on Earth. We calculated their orientation and elongation using a projection-agnostic method in MATLAB. Our findings reveal that calderas exhibit a uniformly distributed orientation and a normally distributed elongation that skews towards circular calderas.

To understand the shape of calderas, we compared their orientation to the maximum horizontal compressive stress orientations indicated by the World Stress Map (Heidbach et al., 2018). In our analysis, we only utilized calderas with below-average elongation because we have more confidence in the orientations of these calderas compared to more circular ones. Our results indicated no spatial dependence between the misorientation of calderas and the stresses. We found that calderas with the greatest misorientation (perpendicular to the maximum horizontal compressional stress) are located closer to the stress measurements. Based on our findings, local rather than regional stresses control the shape of calderas. We propose two methods for determining the orientation and elongation of calderas:

1. Deformation: We see evidence that calderas are perpendicular to the maximum horizontal compressive stress. This implies that the shape of the caldera results from a form of strain. For calderas to have the shape we observe, the magma chamber of the caldera is deformed and elongated by local stresses, similar to those seen in Ilopango.
2. Preexisting Structures: Toba and Cerro Galán may serve as examples of calderas whose shapes are influenced by local fault features. The eastern and western edges of Cerro Galán are bounded by N-S faults, giving Cerro Galán its N-S

orientation, while nearby calderas have different orientations. In Toba, stepovers created by the Sumatra fault may have established a transtensional environment where magma could have preferentially migrated along the fault trace. This might explain why Toba exhibits an orientation similar to that of the Sumatra fault. Various studies have also proposed a similar reactivation for controlling the shape of calderas (Acocella et al., 2003, 2004; Cole et al., 2005; Folch & Martí, 2004) . In these calderas, the preexisting structures create zones of preferential magma chamber elongation, resulting in elongated calderas.

Future studies should refine the relationship between local faults and the shape of calderas. These studies can explore the age relationship between calderas and local fault systems to determine the influence of faults on calderas. This work offers new insights into the role of local and regional lithospheric stresses on the geometry of magma chambers beneath calderas.

Chapter 5. Conclusion & Future Work

5.1 Conclusions

5.1.1 Europa

We calculated the orientation and elongation of 1,035 microfeatures using new projection-independent methods. We find that the orientation distribution of these features is not uniformly distributed. When we analyze our data by feature type, hybrids and chaos showed multimodal to uniform distributions, while pits and domes had the narrowest distributions. We found no dependence on the orientation of features and their latitude.

We conclude that microfeatures on Europa formed episodically and under various stresses. We support microchaos formation models that show an evolution of features from pits and domes to hybrids and chaos. We categorize chaos and hybrids as having long-lived formation, which can record various stress orientations, while pits and domes are short-lived. We argue that future models of microchaos formation must consider the elongated shape of microfeatures and the role of local and regional stresses. Our observations are most compatible with a diapir or liquid water body model.

5.1.2 Venus

We created a new digital map of 525 coronae. Our database contained new morphological measurements like orientation and elongation. Through circular statistical tests, we find that coronae have a non-uniform orientation distribution. We determined that the orientation of coronae is not dependent on area or circularity. We

compared the orientation of coronae to Chasmata using a spherical definition of misorientation. Our results show that coronae are oriented parallel to the strike of Chasmata. Using Chasmata as stress indicators, coronae are elongated in the same direction as the maximum horizontal compressional stress.

We find that regional stress fields play a significant role in determining the shape of coronae. Our results indicate that coronae formation may utilize preexisting faults or lithospheric weak zones associated with Chasmata. These results support models of coronae formation that have melt preferentially injected in the direction of maximum compressive stress or a rising plume that pools along an elongated step in lithospheric thickness.

5.1.3 Earth

Using a preexisting caldera database (Global Volcanism Program & Venzke, 2024), we mapped 57 calderas and determined their orientation and elongation. We found that calderas have a circularity distribution that skews towards circular calderas and that their orientation distribution is uniformly distributed. We compared the orientations of below-average elongated calderas to stress measurements (Heidbach et al., 2018). We find that calderas are elongated perpendicular to the direction of maximum horizontal compressive stress, particularly when calderas are proximal to the stress measurements.

We determined that local rather than regional stresses determine the shape of calderas. We advocate for two methods for how calderas have an orientation and elongation: deformation and pre-existing structures. We argue that a caldera's magma chamber is deformed by local stress, resulting in the observed shape of calderas.

Additionally, we found evidence of calderas being elongated parallel to preexisting structures (in Sumatra and Argentina), implying that magma may be preferentially injected along preexisting fault structures. Our results provide insight into the importance of local and preexisting structures on the shape of magma chambers beneath calderas.

5.2 Future Work

5.2.1 Expansion to Venus Research

To expand on the Venusian results, I am interested in comparing the orientation of coronae to other structural features. In particular, I am interested in comparing the orientation of coronae to wrinkle ridges. Wrinkle ridges are sinuous ridges that are topographically positive and are predominantly located in the plains regions of Venus. It is proposed that they are formed by folding and /or thrust faulting (Bethell et al., 2022; Dragoni & Piombo, 2003; McGill, 1993; Plescaa & Golombek, 1986; Watters, 1988). Compared to Chasmata, we expect the maximum horizontal compressional stress to be perpendicular to the strike of wrinkle ridges. Bilotti & Suppe (1999) developed a map of 65,00 wrinkle ridges. I want to compare the orientation of wrinkle ridges to coronae with this dataset. This comparison aims to understand the orientation of coronae that are not located within a 600 km radius of Chasmata. Coronae located in the plains region had the largest variability in misorientation. I am interested in determining the role wrinkle ridges have on the shape of these coronae. The goal is to have a comparative analysis of how the shape of coronae is determined by the various stress regimes on Venus: tensile and compressive. This work can further our understanding of how different regions on Venus interact with diapiric rises.

I am interested in comparing additional morphological markers to the coronae's orientation. Our results showed that coronae's orientation is independent of area or circularity. I want to expand this analysis to the different types of coronae: concentric, concentric-double ring, radial, asymmetric, and multiple (Stofan et al., 1992). I am interested in comparing the orientation distributions of coronae among these groups. This work could challenge our current understanding of how coronae form. I am interested in investigating popular coronae formation conclusions, such as coronae having an evolutionary scheme and all coronae being a part of the same population.

5.2.2 Expansion to Earth Research

Small sample sizes are a significant limitation to statistical analysis. I am interested in increasing the caldera database on Earth. Geyer & Martí (2008) developed a database of 280 calderas. Since then, this database has grown to include 477 calderas (Geyer et al., 2024). Neither database contains ArcGIS files describing the shape of each caldera, nor is it easily accessible. Methods described in Chapter 4 can be repeated with the Geyer et al. (2024) database. I want to include new morphological measurements, like topography, in the database. The goal is to have a more representative sample of calderas on Earth. This extensive mapping effort aims to improve our understanding of the morphology of calderas globally and further the modeling of their formation.

I am also interested in investigating the role of caldera morphology in caldera elongation and orientation. The Geyer et al. (2024) database provides data on the composition of some calderas. I want to compare the orientation and composition of

calderas to investigate the role magma composition may have on caldera elongation. With the increase in data, I want to further compare calderas within different tectonic regions. In particular, I am interested in studying calderas in tensile environments. The goal is to understand how different morphological markers may impact the shape of calderas on Earth.

Bibliography

Acocella, V. (2007). Understanding caldera structure and development: An overview of analogue models compared to natural calderas. Earth-Science Reviews, 85(3), 125–160. https://doi.org/10.1016/j.earscirev.2007.08.004

Acocella, V., Funiciello, R., Marotta, E., Orsi, G., & de Vita, S. (2004). The role of extensional structures on experimental calderas and resurgence. Journal of Volcanology and Geothermal Research, 129(1), 199–217. https://doi.org/10.1016/S0377-0273(03)00240-3

Acocella, V., Korme, T., Salvini, F., & Funiciello, R. (2003). Elliptic calderas in the Ethiopian Rift: Control of pre-existing structures. Journal of Volcanology and Geothermal Research, 119(1), 189–203. https://doi.org/10.1016/S0377-0273(02)00342-6

Adams, A. C., Stegman, D. R., Mohammadzadeh, H., Smrekar, S. E., & Tackley, P. J. (2023). Plume-Induced Delamination Initiated at Rift Zones on Venus. Journal of Geophysical Research: Planets, 128(10), e2023JE007879. https://doi.org/10.1029/2023JE007879

Allu Peddinti, D., & McNamara, A. K. (2019). Dynamical investigation of a thickening ice-shell: Implications for the icy moon Europa. Icarus, 329, 251–269, doi: 10.1016/j.icarus.2019.03.037

Annen, C., Blundy, J. D., & Sparks, R. S. J. (2006). The Genesis of Intermediate and Silicic Magmas in Deep Crustal Hot Zones. Journal of Petrology, 47(3), 505–539. https://doi.org/10.1093/petrology/egi084

Baer, G., Schubert, G., Bindschadler, D. L., & Stofan, E. R. (1994). Spatial and temporal relations between coronae and extensional belts, northern Lada Terra, Venus. Journal of Geophysical Research: Planets, 99(E4), 8355–8369. https://doi.org/10.1029/93JE03092

Basilevsky, A. T., & Head III, J. W. (2000). Rifts and large volcanoes on Venus: Global assessment of their age relations with regional plains. Journal of Geophysical Research: Planets, 105(E10), 24583–24611. https://doi.org/10.1029/2000JE001260

Basilevsky, A. T., & Head, J. W. (1997). Onset Time and Duration of Corona Activity on Venus: Stratigraphy and History from Photogeologic Study of Stereo Images. Earth, Moon, and Planets, 76(1), 67–115. https://doi.org/10.1023/A:1006009531826

Bellier, O., & Sébrier, M. (1994). Relationship between tectonism and volcanism along the Great Sumatran Fault Zone deduced by spot image analyses. Tectonophysics, 233(3), 215–231. https://doi.org/10.1016/0040-1951(94)90242-9

Bethell, E. M., Ernst, R. E., & Samson, C. (2022). Analysis of Venusian Wrinkle Ridge Morphometry Using Stereo-Derived Topography: A Case Study From Southern Eistla Regio. Journal of Geophysical Research: Planets, 127(5), e2021JE006879. https://doi.org/10.1029/2021JE006879

Bilotti, F., & Suppe, J. (1999). The Global Distribution of Wrinkle Ridges on Venus. Icarus, 139(1), 137–157. https://doi.org/10.1006/icar.1999.6092

Bindschadler, D. L., Schubert, G., & Kaula, W. M. (1992). Coldspots and hotspots: Global tectonics and mantle dynamics of Venus. Journal of Geophysical Research: Planets, 97(E8), 13495–13532. https://doi.org/10.1029/92JE01165

Bland, M. T., Weller, L. A., Archinal, B. A., Smith, E., & Wheeler, B. H. (2021). Improving the Usability of Galileo and Voyager Images of Jupiter's Moon Europa. Earth and Space Science, 8(12), e2021EA001935, doi: 10.1029/2021EA001935

Bosworth, W., Burke, K., & Strecker, M. (2003). Effect of stress fields on magma chamber stability and the formation of collapse calderas. Tectonics, 22(4). https://doi.org/10.1029/2002TC001369

Branney, M., & Acocella, V. (2015). Chapter 16—Calderas. In H. Sigurdsson (Ed.), The Encyclopedia of Volcanoes (Second Edition) (pp. 299–315). Academic Press. https://doi.org/10.1016/B978-0-12-385938-9.00016-X

Brown, C. D., & Grimm, R. E. (1995). Tectonics of Artemis Chasma: A Venusian "Plate" Boundary. Icarus, 117(2), 219–249. https://doi.org/10.1006/icar.1995.1155

Campbell, D. B., Head, J. W., Harmon, J. K., & Hine, A. A. (1984). Venus: Volcanism and Rift Formation in Beta Regio. Science, 226(4671), 167–170.

Carr, M. H., Belton, M. J. S., Chapman, C. R., Davies, M. E., Geissler, P., Greenberg, R., McEwen, A. S., Tufts, B. R., Greeley, R., Sullivan, R., Head, J. W., Pappalardo, R. T., Klaasen, K. P., Johnson, T. V., Kaufman, J., Senske, D., Moore, J., Neukum, G., Schubert, G., … Veverka, J. (1998). Evidence for a subsurface ocean on Europa. Nature, 391(6665), 363–365. https://doi.org/10.1038/34857

Cassen, P., Peale, S. J., & Reynolds, R. T. (1980). Tidal dissipation in Europa: A correction. Geophysical Research Letters, 7(11), 987–988. https://doi.org/10.1029/GL007i011p00987

Cole, J. W., Milner, D. M., & Spinks, K. D. (2005). Calderas and caldera structures: A review. Earth-Science Reviews, 69(1), 1–26. https://doi.org/10.1016/j.earscirev.2004.06.004

Collins, G. C., Head III, J. W., Pappalardo, R. T., & Spaun, N. A. (2000). Evaluation of models for the formation of chaotic terrain on Europa. Journal of Geophysical Research: Planets, 105(E1), 1709–1716. https://doi.org/10.1029/1999JE001143

Collins, G. C., Patterson, G. W., Detelich, C. E., Prockter, L. M., Kattexnhorn, S. A., Cooper, C. M., Rhoden, A. R., Cutler, B. B., Oldrid, S. R., Perkins, R. P., & Rezza, C. A. (2022). Episodic Plate Tectonics on Europa: Evidence for Widespread Patches of Mobile-Lid Behavior in the Antijovian Hemisphere. Journal of Geophysical Research: Planets, 127(11), e2022JE007492, doi: 10.1029/2022JE007492

Collins, G., & Nimmo, F. (2009). Chaotic Terrain on Europa. In Europa, Eds. R. Pappalardo, W.B. McKinnon, & K.K. Khurana, University of Arizona Press, pp. 259–281, doi: 10.2307/j.ctt1xp3wdw.17

Cordeiro, G. M., & de Paula Ferrari, S. L. (1991). A Modified Score Test Statistic Having Chi-Squared Distribution to Order n-1. Biometrika. 78(3), 573-582, doi: 10.2307/2337026

Crameri, F. (2021). Scientific colour maps (7.0.1). Zenodo, doi: 10.5281/zenodo.5501399
Crawford, G. D., & Stevenson, D. J. (1988). Gas-driven water volcanism and the resurfacing of Europa. Icarus, 73(1), 66–79. https://doi.org/10.1016/0019-1035(88)90085-1
Culha, C., & Manga, M. (2016). Geometry and spatial distribution of lenticulae on Europa. Icarus, 271, 49–56. https://doi.org/10.1016/j.icarus.2015.12.052
Doggett, T., Greeley, R., Figueredo, P., and Tanaka, K. (2009), Geologic stratigraphy and evolution of Europa's surface, In Europa, Eds. R. Pappalardo, W.B. McKinnon, & K.K. Khurana, University of Arizona Press, pp. 137–160, doi: 10.2307/j.ctt1xp3wdw.12
Dombard, A. J., Johnson, C. L., Richards, M. A., & Solomon, S. C. (2007). A magmatic loading model for coronae on Venus. Journal of Geophysical Research: Planets, 112(E4). https://doi.org/10.1029/2006JE002731
Dragoni, M., & Piombo, A. (2003). A model for the formation of wrinkle ridges in volcanic plains on Venus. Physics of the Earth and Planetary Interiors, 135(2), 161–171. https://doi.org/10.1016/S0031-9201(02)00205-4
El Bilali, H., Ernst, R. E., Buchan, K. L., & Head, J. W. (2023). Dyke swarms record the plume stage evolution of the Atla Regio superplume on Venus. Communications Earth & Environment, 4(1), 1–10. https://doi.org/10.1038/s43247-023-00901-7
Ernst, R. E., & Desnoyers, D. W. (2004). Lessons from Venus for understanding mantle plumes on Earth. Physics of the Earth and Planetary Interiors, 146(1), 195–229. https://doi.org/10.1016/j.pepi.2003.10.012
Ernst, R. E., Head, J. W., Parfitt, E., Grosfils, E., & Wilson, L. (1995). Giant radiating dyke swarms on Earth and Venus. Earth-Science Reviews, 39(1–2), 1–58. https://doi.org/10.1016/0012-8252(95)00017-5
Fagents, S. A. (2003). Considerations for effusive cryovolcanism on Europa: The post-Galileo perspective. Journal of Geophysical Research: Planets, 108(E12). https://doi.org/10.1029/2003JE002128
Figueredo, P. H., & Greeley, R. (2000). Geologic mapping of the northern leading hemisphere of Europa from Galileo solid-state imaging data. Journal of Geophysical Research: Planets, 105(E9), 22629–22646, doi: 10.1029/1999JE001107
Figueredo, P. H., & Greeley, R. (2004). Resurfacing history of Europa from pole-to-pole geological mapping. Icarus, 167(2), 287–312, doi: 10.1016/j.icarus.2003.09.016
Figueredo, P. H., Chuang, F. C., Rathbun, J., Kirk, R. L., & Greeley, R. (2002). Geology and origin of Europa's "Mitten" feature (Murias Chaos). Journal of Geophysical Research: Planets, 107(E5), 2-1-2–13. https://doi.org/10.1029/2001JE001591
Fisher, N. I. (1993). Statistical Analysis of Circular Data. Cambridge University Press, doi: 10.1017/cbo9780511564345
Fisher, N. I., Lewis, T., & Embleton, B. J. J. (1987). Statistical Analysis of Spherical Data. Cambridge University Press. https://doi.org/10.1017/CBO9780511623059

Fluegel, B., Tivey, M., Biasi, J., Chadwick Jr., W. W., & Nooner, S. L. (2022). The Magnetization of an Underwater Caldera: A Time-Lapse Magnetic Anomaly Study of Axial Seamount. Geophysical Research Letters, 49(17), e2022GL100008. https://doi.org/10.1029/2022GL100008

Folch, A., & Martí, J. (2004). Geometrical and mechanical constraints on the formation of ring-fault calderas. Earth and Planetary Science Letters, 221(1), 215–225. https://doi.org/10.1016/S0012-821X(04)00101-3

Folkes, C. B., Wright, H. M., Cas, R. A. F., de Silva, S. L., Lesti, C., & Viramonte, J. G. (2011). A re-appraisal of the stratigraphy and volcanology of the Cerro Galán volcanic system, NW Argentina. Bulletin of Volcanology, 73(10), 1427–1454. https://doi.org/10.1007/s00445-011-0459-y

Geissler, P., Greenberg, R., Hoppa, G., Helfenstein, P., McEwen, A., Pappalardo, R., Tufts, R., Ockert-Bell, M., Sullivan, R., Greeley, R., & others. (1998). Evidence for non-synchronous rotation of Europa. Nature, 391(6665), 368–370, doi: 10.1038/34869

Geshi, N., Miyagi, I., Saito, G., & Conway, C. E. (2023). Caldera collapse thresholds correlate with magma chamber dimensions. Scientific Reports, 13(1), 7463. https://doi.org/10.1038/s41598-023-34411-5

Geyer, A., & Martí, J. (2008). The new worldwide collapse caldera database (CCDB): A tool for studying and understanding caldera processes. Journal of Volcanology and Geothermal Research, 175(3), 334–354. https://doi.org/10.1016/j.jvolgeores.2008.03.017

Geyer, A., Marti, J., & Pedrazzi, D. (2024). CCDB: The collapse caldera worldwide database (version 4.0, 2019) [Dataset]. Zenodo. https://doi.org/10.5281/zenodo.10636011

Glaze, L. S., Stofan, E. R., Smrekar, S. E., & Baloga, S. M. (2002). Insights into corona formation through statistical analyses. Journal of Geophysical Research: Planets, 107(E12), 18-1-18–12. https://doi.org/10.1029/2002JE001904

Global Volcanism Program, & Venzke, E. (2024). Volcanoes of the World, v.5.2.0 [Dataset]. Global Volcanism Program.

Goodman, J. C., Collins, G. C. Marshall, J., and Pierrehumbert, R. T. (2004), Hydrothermal plume dynamics on Europa: Implications for chaos formation, Journal of Geophysical Research: Planets, 109(E3), E03008, doi: 10.1029/2003JE002073.

Goss, A. R., Kay, S. M., Mpodozis, C., & Singer, B. S. (2009). The Incapillo Caldera and Dome Complex (∼ 28° S, Central Andes): A stranded magma chamber over a dying arc. Journal of Volcanology and Geothermal Research, 184(3), 389–404. https://doi.org/10.1016/j.jvolgeores.2009.05.005

Gottsmann, J., Berrino, G., Rymer, H., & Williams-Jones, G. (2003). Hazard assessment during caldera unrest at the Campi Flegrei, Italy: A contribution from gravity–height gradients. Earth and Planetary Science Letters, 211(3), 295–309. https://doi.org/10.1016/S0012-821X(03)00225-5

Graff, J. R., Ernst, R. E., & Samson, C. (2018). Evidence for triple-junction rifting focussed on local magmatic centres along Parga Chasma, Venus. Icarus, 306, 122–138. https://doi.org/10.1016/j.icarus.2018.02.010

Greeley, R., Figueredo, P. H., Williams, D. A., Chuang, F. C., Klemaszewski, J. E., Kadel, S. D., Prockter, L. M., Pappalardo, R. T., Head III, J. W., Collins, G. C., Spaun, N. A., Sullivan, R. J., Moore, J. M., Senske, D. A., Tufts, B. R., Johnson, T. V., Belton, M. J. S., & Tanaka, K. L. (2000). Geologic mapping of Europa. Journal of Geophysical Research: Planets, 105(E9), 22559–22578, doi: 10.1029/1999JE001173

Greeley, R., Sullivan, R., Klemaszewski, J., Homan, K., Head, J. W., Pappalardo, R. T., Veverka, J., Clark, B. E., Johnson, T. V., Klaasen, K. P., Belton, M., Moore, J., Asphaug, E., Carr, M. H., Neukum, G., Denk, T., Chapman, C. R., Pilcher, C. B., Geissler, P. E., … Tufts, R. (1998). Europa: Initial Galileo Geological Observations. Icarus, 135(1), 4–24. https://doi.org/10.1006/icar.1998.5969

Greenberg, R. (2015). Lenticula. In: Encyclopedia of Planetary Landforms, Hargitai, H., Kereszturi, Á. (eds). Springer, New York, NY, doi: 10.1007/978-1-4614-3134-3_217

Greenberg, R., Hoppa, G. V., Tufts, B. R., Geissler, P., Riley, J., & Kadel, S. (1999). Chaos on Europa. Icarus, 141(2), 263–286. https://doi.org/10.1006/icar.1999.6187

Greenberg, R., Leake, M. A., Hoppa, G. V., & Tufts, B. R. (2003). Pits and uplifts on Europa. Icarus, 161(1), 102–126, doi: 10.1016/S0019-1035(02)00013-1

Gudmundsson, A. (2008). Chapter 8 Magma-Chamber Geometry, Fluid Transport, Local Stresses and Rock Behaviour During Collapse Caldera Formation. In J. Gottsmann & J. Martí (Eds.), Developments in Volcanology (Vol. 10, pp. 313–349). Elsevier. https://doi.org/10.1016/S1871-644X(07)00008-3

Gudmundsson, A. (2012). Magma chambers: Formation, local stresses, excess pressures, and compartments. Journal of Volcanology and Geothermal Research, 237–238, 19–41. https://doi.org/10.1016/j.jvolgeores.2012.05.015

Guest, J. E., & Stofan, E. R. (1999). A New View of the Stratigraphic History of Venus. Icarus, 139(1), 55–66. https://doi.org/10.1006/icar.1999.6091

Gülcher, A. J. P., Gerya, T. V., Montési, L. G. J., & Munch, J. (2020). Corona structures driven by plume–lithosphere interactions and evidence for ongoing plume activity on Venus. Nature Geoscience, 13(8), Article 8. https://doi.org/10.1038/s41561-020-0606-1

Gülcher, A. J. P., Yu, T.-Y., & Gerya, T. V. (2023). Tectono-Magmatic Evolution of Asymmetric Coronae on Venus: Topographic Classification and 3D Thermo-Mechanical Modeling. Journal of Geophysical Research: Planets, 128(11), e2023JE007978. https://doi.org/10.1029/2023JE007978

Guseva, E. N. (2016). Classification of the rift zones of venus: Rift valleys and graben belts. Solar System Research, 50(3), 184–196. https://doi.org/10.1134/S0038094616030023

Hamilton, V. E., & Stofan, E. R. (1996). The Geomorphology and Evolution of Hecate Chasma, Venus. Icarus, 121(1), 171–194. https://doi.org/10.1006/icar.1996.0077

Han, L., & Showman, A. P. (2011). Coupled convection and tidal dissipation in Europa's ice shell using non-Newtonian grain-size-sensitive (GSS) creep rheology. Icarus, 212(1), 262–267. https://doi.org/10.1016/j.icarus.2010.11.034

Hansen, V. L. (2002). Artemis: Surface expression of a deep mantle plume on Venus. GSA Bulletin, 114(7), 839–848. https://doi.org/10.1130/0016-7606(2002)114<0839:ASEOAD>2.0.CO;2

Hansen, V. L., & Olive, A. (2010). Artemis, Venus: The largest tectonomagmatic feature in the solar system? Geology, 38(5), 467–470. https://doi.org/10.1130/G30643.1

Hansen, V. L., & Phillips, R. J. (1993). Tectonics and Volcanism of Eastern Aphrodite Terra, Venus: No Subduction, No Spreading. Science, 260(5107), 526–530.

Harris, L. B., & Bédard, J. H. (2015). Interactions between continent-like 'drift', rifting and mantle flow on Venus: Gravity interpretations and Earth analogues. In T. Platz, M. Massironi, P. K. Byrne, & H. Hiesinger (Eds.), Volcanism and Tectonism Across the Inner Solar System (Vol. 401, p. 0). Geological Society of London. https://doi.org/10.1144/SP401.9

Head, J. W., & Crumpler, L. S. (1987). Evidence for Divergent Plate-Boundary Characteristics and Crustal Spreading on Venus. Science, 238(4832), 1380–1385.

Head, J. W., & Pappalardo, R. T. (1999). Brine mobilization during lithospheric heating on Europa: Implications for formation of chaos terrain, lenticula texture, and color variations. Journal of Geophysical Research: Planets, 104(E11), 27143–27155. https://doi.org/10.1029/1999JE001062

Head, J. W., Crumpler, L. S., Aubele, J. C., Guest, J. E., & Saunders, R. S. (1992). Venus volcanism: Classification of volcanic features and structures, associations, and global distribution from Magellan data. Journal of Geophysical Research: Planets, 97(E8), 13153–13197. https://doi.org/10.1029/92JE01273

Heidbach, O., Rajabi, M., Cui, X., Fuchs, K., Müller, B., Reinecker, J., Reiter, K., Tingay, M., Wenzel, F., Xie, F., Ziegler, M. O., Zoback, M.-L., & Zoback, M. (2018). The World Stress Map database release 2016: Crustal stress pattern across scales. Tectonophysics, 744, 484–498. https://doi.org/10.1016/j.tecto.2018.07.007

Herrick, R. R., & Hensley, S. (2023). Surface changes observed on a Venusian volcano during the Magellan mission. Science, 379(6638), 1205–1208. https://doi.org/10.1126/science.abm7735

Holohan, E. P., Troll, V. R., Walter, T. R., Münn, S., McDonnell, S., & Shipton, Z. K. (2005). Elliptical calderas in active tectonic settings: An experimental approach. Journal of Volcanology and Geothermal Research, 144(1), 119–136. https://doi.org/10.1016/j.jvolgeores.2004.11.020

Hoppa, G. V. (1999). Formation of Cycloidal Features on Europa. Science, 285(5435), 1899–1902, doi: 10.1126/science.285.5435.1899

Howell, S. M., & Pappalardo, R. T. (2018). Band Formation and Ocean-Surface Interaction on Europa and Ganymede. Geophysical Research Letters, 45(10), 4701–4709, doi: 10.1029/2018GL077594

International Astronomical Union Working Group for Planetary System Nomenclature. (2024). Gazetteer of Planetary Nomenclature [Dataset]. http://planetarynames.wr.usgs.gov/.

Ivanov, M. A., & Head, J. W. (2011). Global geological map of Venus. Planetary and Space Science, 59(13), 1559–1600. https://doi.org/10.1016/j.pss.2011.07.008
Ivanov, M. A., & Head, J. W. (2013). The history of volcanism on Venus. Planetary and Space Science, 84, 66–92. https://doi.org/10.1016/j.pss.2013.04.018
Janes, D. M., Squyres, S. W., Bindschadler, D. L., Baer, G., Schubert, G., Sharpton, V. L., & Stofan, E. R. (1992). Geophysical models for the formation and evolution of coronae on Venus. Journal of Geophysical Research: Planets, 97(E10), 16055–16067. https://doi.org/10.1029/92JE01689
Jia, X., Kivelson, M. G., Khurana, K. K., & Kurth, W. S. (2018). Evidence of a plume on Europa from Galileo magnetic and plasma wave signatures. Nature Astronomy, 2(6), 459–464. https://doi.org/10.1038/s41550-018-0450-z
Jiménez-Díaz, A., Ruiz, J., Kirby, J. F., Romeo, I., Tejero, R., & Capote, R. (2015). Lithospheric structure of Venus from gravity and topography. Icarus, 260, 215–231. https://doi.org/10.1016/j.icarus.2015.07.020
Kalousová, K., Souček, O., Tobie, G., Choblet, G., & Čadek, O. (2014). Ice melting and downward transport of meltwater by two-phase flow in Europa's ice shell. Journal of Geophysical Research: Planets, 119(3), 532–549, doi: 10.1002/2013JE004563
Kang, W. (2022). Different Ice-shell Geometries on Europa and Enceladus due to Their Different Sizes: Impacts of Ocean Heat Transport. The Astrophysical Journal, 934(2), 116), doi: 10.3847/1538-4357/ac779c
Kennedy, B., Stix, J., Vallance, J. W., Lavallée, Y., & Longpré, M.-A. (2004). Controls on caldera structure: Results from analogue sandbox modeling. GSA Bulletin, 116(5–6), 515–524. https://doi.org/10.1130/B25228.1
Kereszturi, A., & Keszthelyi, Z. (2013). Astrobiological implications of chaos terrains on Europa to help targeting future missions. Planetary and Space Science, 77, 74–90, doi: 10.1016/j.pss.2012.08.028
Khurana, K. K., Kivelson, M. G., Stevenson, D. J., Schubert, G., Russell, C. T., Walker, R. J., & Polanskey, C. (1998). Induced magnetic fields as evidence for subsurface oceans in Europa and Callisto. Nature, 395(6704), 777–780. https://doi.org/10.1038/27394
Kiefer, W. S., & Peterson, K. (2003). Mantle and crustal structure in Phoebe Regio and Devana Chasma, Venus. Geophysical Research Letters, 30(1), 5-1-5–4. https://doi.org/10.1029/2002GL015762
Kiefer, W. S., & Swafford, L. C. (2006). Topographic analysis of Devana Chasma, Venus: Implications for rift system segmentation and propagation. Journal of Structural Geology, 28(12), 2144–2155. https://doi.org/10.1016/j.jsg.2005.12.002
Kivelson, M. G., Khurana, K. K., Russell, C. T., Volwerk, M., Walker, R. J., & Zimmer, C. (2000). Galileo Magnetometer Measurements: A Stronger Case for a Subsurface Ocean at Europa. Science, 289(5483), 1340–1343. https://doi.org/10.1126/science.289.5483.1340
Koch, D. M., & Manga, M. (1996). Neutrally buoyant diapirs: A model for Venus coronae. Geophysical Research Letters, 23(3), 225–228. https://doi.org/10.1029/95GL03776

Krassilnikov, A. S., Kostama, V.-P., Aittola, M., Guseva, E. N., & Cherkashina, O. S. (2012). Relationship of coronae, regional plains and rift zones on Venus. Planetary and Space Science, 68(1), 56–75. https://doi.org/10.1016/j.pss.2011.11.017

Kuiper, N. H. (1960). Tests concerning random points on a circle. Nederl. Akad. Wetensch. Proc. Ser. A, 63(1), 38–47, doi: 10.1016/s1385-7258(60)50006-0

Kusumoto, S., & Takemura, K. (2005). Caldera geometry determined by the depth of the magma chamber. Earth, Planets and Space, 57(11), e17–e20. https://doi.org/10.1186/BF03351879

Kvorka, J., & Čadek, O. (2024). The role of subsurface ocean dynamics and phase transitions in forming the topography of icy moons. Icarus, 412, 115985, doi: 10.1016/j.icarus.2024.115985

Lees, J. M. (2007). Seismic tomography of magmatic systems. Journal of Volcanology and Geothermal Research, 167(1), 37–56. https://doi.org/10.1016/j.jvolgeores.2007.06.008

Leonard, E. J., Alex Patthoff, D., & Senske, D. A. (2024). Global geologic map of Europa. Scientific Investigations Map. US Geological Survey, doi: 10.3133/sim3513

Leonard, E.J., Pappalardo, R. T., & Yin, A. (2018). Analysis of very-high-resolution Galileo images and implications for resurfacing mechanisms on Europa. Icarus, 312, 100-120, doi: 10.1016/j.icarus.2018.04.016

Lipman, P. W. (1997). Subsidence of ash-flow calderas: Relation to caldera size and magma-chamber geometry. Bulletin of Volcanology, 59(3), 198–218. https://doi.org/10.1007/s004450050186

Lucchitta, B.K., & Soderblom, L.A., 1982, The geology of Europa, In Satellites of Jupiter, Eds. D. Morrison, D., University of Arizona Press, p. 521-555

Magee Roberts, K., & Head, J. W. (1993). Large-scale volcanism associated with coronae on Venus: Implications for formation and evolution. Geophysical Research Letters, 20(12), 1111–1114. https://doi.org/10.1029/93GL01484

Magee, K. P., & Head, J. W. (1995). The role of rifting in the generation of melt: Implications for the origin and evolution of the Lada Terra-Lavinia Planitia region of Venus. Journal of Geophysical Research: Planets, 100(E1), 1527–1552. https://doi.org/10.1029/94JE02334

Manga, M., & Michaut, C. (2017). Formation of lenticulae on Europa by saucer-shaped sills. Icarus, 286, 261–269. https://doi.org/10.1016/j.icarus.2016.10.009

Manga, M., & Wang, C.-Y. (2007). Pressurized oceans and the eruption of liquid water on Europa and Enceladus. Geophysical Research Letters, 34(7). https://doi.org/10.1029/2007GL029297

Mardia, K., & Jupp, P. (1999). Directional Statistics. In Wiley Series in Probability and Statistics. Wiley, doi: 10.1002/9780470316979

Mardia, K., & Jupp, P. (2000). Directional Statistics. https://doi.org/10.1002/9780470316979.ch11

Mardia, K.V. (1972) Statistics of Directional Data. Academic Press, London, sec. 26.5, p. 617

Marti, J., Ablay, G. J., Redshaw, L. T., & Sparks, R. S. J. (1994). Experimental studies of collapse calderas. Journal of the Geological Society, 151(6), 919–929. https://doi.org/10.1144/gsjgs.151.6.0919

Martin, P., Stofan, E. R., Glaze, L. S., & Smrekar, S. (2007). Coronae of Parga Chasma, Venus. Journal of Geophysical Research: Planets, 112(E4). https://doi.org/10.1029/2006JE002758

Martínez-Díaz, J. J., Álvarez-Gómez, J. A., Staller, A., Alonso-Henar, J., Canora, C., Insúa-Arévalo, J. M., Tsige, M., Villamor, P., Herrero-Barbero, P., Hernández-Moreno, C., Hernández, W., Hernández, D., Marroquín, G., & Mixco, L. (2021). Active faults of El Salvador. Journal of South American Earth Sciences, 105, 103038. https://doi.org/10.1016/j.jsames.2020.103038

McGill, G. E. (1993). Wrinkle ridges, stress domains, and kinematics of Venusian plains. Geophysical Research Letters, 20(21), 2407–2410. https://doi.org/10.1029/93GL02635

McGill, G. E. (2004). Tectonic and stratigraphic implications of the relative ages of venusian plains and wrinkle ridges. Icarus, 172(2), 603–612. https://doi.org/10.1016/j.icarus.2004.07.008

McGill, G. E., Steenstrup, S. J., Barton, C., & Ford, P. G. (1981). Continental rifting and the origin of Beta Regio, Venus. Geophysical Research Letters, 8(7), 737–740. https://doi.org/10.1029/GL008i007p00737

McKillup, S., & Dyar, M. D. (2010). Geostatistics Explained: An Introductory Guide for Earth Scientists (1st edition). Cambridge University Press, doi: 10.1017/CBO9780511807558

Mével, L., & Mercier, E. (2007). Large-scale doming on Europa: A model of formation of Thera Macula. Planetary and Space Science, 55(7), 915–927. https://doi.org/10.1016/j.pss.2006.12.001

Michaut, C., & Manga, M. (2014), Domes, pits, and small chaos on Europa produced by water sills, Journal of Geophysical Research: Planets, 119, 550–573, doi: 10.1002/2013JE004558.

Mitri, G., & Showman, A. P. (2005). Convective–conductive transitions and sensitivity of a convecting ice shell to perturbations in heat flux and tidal-heating rate: Implications for Europa. Icarus 177(2), 447–460, doi: 10.1016/j.icarus.2005.03.019.

Miyamoto, H., Mitri, G., Showman, A. P., & Dohm, J. M. (2005). Putative ice flows on Europa: Geometric patterns and relation to topography collectively constrain material properties and effusion rates, Icarus, 177(2), 413-424, doi: 10.1016/j.icarus.2005.03.014

Natawidjaja, D. H. (2018). Updating active fault maps and sliprates along the Sumatran Fault Zone, Indonesia. IOP Conference Series: Earth and Environmental Science, 118(1), 012001. https://doi.org/10.1088/1755-1315/118/1/012001

Noviello, J. . L., Torrano, Z. A., Singer, K. N. & Rhoden, A. R. (2019b). Data for: Mapping Europa's microfeatures in regional mosaics: new constraints on formation models [Dataset]. Mendeley, doi: 10.17632/FZNNBFTT8X.1

Noviello, J. L., & Rhoden, A. R. (2021). Quantifying misidentification rates of Europa's microfeatures in low-resolution Galileo imaging, Icarus, 365, 114495, doi: 10.1016/j.icarus.2021.114495
Noviello, J. L., Torrano, Z. A., Rhoden, A. R., & Singer, K. N. (2019). Mapping Europa's microfeatures in regional mosaics: New constraints on formation models. Icarus, 329, 101–123. https://doi.org/10.1016/j.icarus.2019.02.038
Noviello, J. L., Torrano, Z. A., Rhoden, A. R., & Singer, K. N. (2019a). Mapping Europa's microfeatures in regional mosaics: New constraints on formation models. Icarus, 329, 101–123, doi: 10.1016/j.icarus.2019.02.038
Nuñez, K. A., & Montesi, L. (2025). Orientation of Microfeatures on Europa. Retrieved from osf.io/fx6jy
O'Brien, D. P., Geissler, P., & Greenberg, R. (2002). A Melt-through Model for Chaos Formation on Europa. Icarus, 156(1), 152–161. https://doi.org/10.1006/icar.2001.6777
Ojakangas, G. W., & Stevenson, D. J. (1989). Thermal state of an ice shell on Europa. Icarus, 81(2), 220–241. https://doi.org/10.1016/0019-1035(89)90052-3
Pappalardo, R. T. (2000) Upwarped domes on Europa: Constraints on mottled terrain formation, Lunar and Planetary Science, XXXI, 1719
Pappalardo, R. T. & Head, J. W. (2001) The thick-shell model of Europa's geology: Implications for crustal processes, Lunar and Planetary Science, XXXII, 1866
Pappalardo, R. T., & Barr, A. C. (2004). The origin of domes on Europa: The role of thermally induced compositional diapirism. Geophysical Research Letters, 31(1). https://doi.org/10.1029/2003GL019202
Pappalardo, R. T., & Barr, A. C. (2004). The origin of domes on Europa: The role of thermally induced compositional diapirism. Geophysical Research Letters, 31(1), doi: 10.1029/2003GL019202
Pappalardo, R. T., Belton, M. J. S., Breneman, H. H., Carr, M. H., Chapman, C. R., Collins, G. C., Denk, T., Fagents, S., Geissler, P. E., Giese, B., Greeley, R., Greenberg, R., Head, J. W., Helfenstein, P., Hoppa, G., Kadel, S. D., Klaasen, K. P., Klemaszewski, J. E., Magee, K., … Williams, K. K. (1999). Does Europa have a subsurface ocean? Evaluation of the geological evidence. Journal of Geophysical Research: Planets, 104(E10), 24015–24055. https://doi.org/10.1029/1998JE000628
Pappalardo, R. T., Head, J. W., Greeley, R., Sullivan, R. J., Pilcher, C., Schubert, G., Moore, W. B., Carr, M. H., Moore, J. M., Belton, M. J., & Goldsby, D. L. (1998). Geological evidence for solid-state convection in Europa's ice shell. Nature, 391(6665), 365–368, doi: 10.1038/34862
Parro, L. M., Ruiz, J., & Pappalardo, R. T. (2016). Timing of chaotic terrain formation in Argadnel Regio, Europa, and implications for geological history. Planetary and Space Science, 130, 24–29, doi: 10.1016/j.pss.2016.02.002
Phillips, R. J., & Hansen, V. L. (1998). Geological Evolution of Venus: Rises, Plains, Plumes, and Plateaus. Science, 279(5356), 1492–1497. https://doi.org/10.1126/science.279.5356.1492
Piskorz, D., Elkins-Tanton, L. T., & Smrekar, S. E. (2014). Coronae formation on Venus via extension and lithospheric instability. Journal of Geophysical Research: Planets, 119(12), 2568–2582. https://doi.org/10.1002/2014JE004636

Plescaa, J. B., & Golombek, M. P. (1986). Origin of planetary wrinkle ridges based on the study of terrestrial analogs. GSA Bulletin, 97(11), 1289–1299. https://doi.org/10.1130/0016-7606(1986)97<1289:OOPWRB>2.0.CO;2

Prockter, L. M., Antman, A. M., Pappalardo, R. T., Head, J. W., & Collins, G. C. (1999). Europa: Stratigraphy and geological history of the anti-Jovian region from Galileo E14 solid-state imaging data. Journal of Geophysical Research: Planets, 104(E7), 16531–, doi: 10.1029/1998JE001015

Prockter, L., and Patterson, G.W., 2009, Morphology and evolution of Europa's ridges and bands, In Europa, Eds. R. Pappalardo, W.B. McKinnon, & K.K. Khurana, University of Arizona Press, pp. 237-258, doi: 10.2307/ j.ctt1xp3wdw.16

Pronin, A. A., & Stofan, E. R. (1990). Coronae on Venus: Morphology, classification, and distribution. Icarus, 87(2), 452–474. https://doi.org/10.1016/0019-1035(90)90148-3

Quick, L. C., Fagents, S. A., Núñez, K. A., Wilk, K. A., Beyer, R. A., Beddingfield, C. B., Martin, E. S., Prockter, L. M., & Hurford, T. A. (2022). Cryolava Dome growth resulting from active eruptions on Jupiter's moon Europa. Icarus, 387, 115185. https://doi.org/10.1016/j.icarus.2022.115185

Quick, L. C., Glaze, L. S., & Baloga, S. M. (2017). Cryovolcanic emplacement of domes on Europa. Icarus, 284, 477–488. https://doi.org/10.1016/j.icarus.2016.06.029

Rathbun, J. A., Musser, G. S., & Squyres, S. W. (1998). Ice diapirs on Europa: Implications for liquid water. Geophysical Research Letters, 25(22), 4157–4160. https://doi.org/10.1029/1998GL900135

Reese, C. C., Solomatov, V. S., & Moresi, L.-N. (1999). Non-Newtonian Stagnant Lid Convection and Magmatic Resur facing on Venus. Icarus, 139(1), 67–80. https://doi.org/10.1006/icar.1999.6088

Regorda, A., Thieulot, C., van Zelst, I., Erdős, Z., Maia, J., & Buiter, S. (2023). Rifting Venus: Insights From Numerical Modeling. Journal of Geophysical Research: Planets, 128(3), e2022JE007588. https://doi.org/10.1029/2022JE007588

Rhoden, A. R., & Hurford, T. A. (2013). Lineament azimuths on Europa: Implications for obliquity and non-synchronous rotation. Icarus, 226(1), 841–859, doi: 10.1016/j.icarus.2013.06.029

Rhoden, A. R., Hurford, T. A., & Manga, M. (2011). Strike-slip fault patterns on Europa: Obliquity or polar wander? Icarus, 211(1), 636–647, doi: 10.1016/j.icarus.2010.11.002

Rhoden, A. R., Mohr, K. J., Hurford, T. A., Henning, W., Sajous, S., Patthoff, D. A., & Dubois, D. (2021). Obliquity, Precession, and Fracture Mechanics: Implications of Europa's Global Cycloid Population. Journal of Geophysical Research: Planets, 126(3), e2020JE006710, doi: 10.1029/2020JE006710

Riley, J., Hoppa, G. V., Greenberg, R., Tufts, B. R., & Geissler, P. (2000). Distribution of chaotic terrain on Europa. Journal of Geophysical Research: Planets, 105(E9), 22599–22615, doi: 10.1029/1999JE001164

Riller, U., Petrinovic, I., Ramelow, J., Strecker, M., & Oncken, O. (2001). Late Cenozoic tectonism, collapse caldera and plateau formation in the central

Andes. Earth and Planetary Science Letters, 188(3), 299–311. https://doi.org/10.1016/S0012-821X(01)00333-8
Roche, O., Druitt, T. H., & Merle, O. (2000). Experimental study of caldera formation. Journal of Geophysical Research: Solid Earth, 105(B1), 395–416. https://doi.org/10.1029/1999JB900298
Ross, M. N., & Schubert, G. (1987). Tidal heating in an internal ocean model of Europa. Nature, 325(6100), 133–134. https://doi.org/10.1038/325133a0
Roth, L., Saur, J., Retherford, K. D., Strobel, D. F., Feldman, P. D., McGrath, M. A., & Nimmo, F. (2014). Transient Water Vapor at Europa's South Pole. Science, 343(6167), 171–174. https://doi.org/10.1126/science.1247051
Sabbeth, L., Carrington, M. A., & Smrekar, S. E. (2024). Constraints on corona formation from an analysis of topographic rims and fracture annuli. Earth and Planetary Science Letters, 633, 118568. https://doi.org/10.1016/j.epsl.2024.118568
Sarid, A. R., Greenberg, R., & Hurford, T. A. (2006). Crack azimuths on Europa: Sequencing of the northern leading hemisphere. Journal of Geophysical Research: Planets, 111(E8) , E08004, doi: 10.1029/2005JE002524
Sarid, A. R., Greenberg, R., Hoppa, G. V., Geissler, P., & Preblich, B. (2004). Crack azimuths on Europa: time sequence in the southern leading face. Icarus, 168(1), 144-157, doi: 10.1016/j.icarus.2003.11.021
Saxby, J., Gottsmann, J., Cashman, K., & Gutiérrez, E. (2016). Magma storage in a strike-slip caldera. Nature Communications, 7(1), 12295. https://doi.org/10.1038/ncomms12295
Schenk, P., Matsuyama, I., & Nimmo, F. (2008). True polar wander on Europa from global-scale small-circle depressions. Nature, 453(7193), 368–371, doi: 10.1038/nature06911
Schmidt, B. E., Blankenship, D. D., Patterson, G. W., & Schenk, P. M. (2011). Active formation of 'chaos terrain' over shallow subsurface water on Europa. Nature, 479, 502-505, doi: 10.1038/nature10608
Schools, J., & Smrekar, S. E. (2024). Formation of coronae topography and fractures via plume buoyancy and melting. Earth and Planetary Science Letters, 633, 118643. https://doi.org/10.1016/j.epsl.2024.118643
Senske, D. A., Schaber, G. G., & Stofan, E. R. (1992). Regional topographic rises on Venus: Geology of Western Eistla Regio and comparison to Beta Regio and Atla Regio. Journal of Geophysical Research: Planets, 97(E8), 13395–13420. https://doi.org/10.1029/92JE01167
Shalygin, E. V., Markiewicz, W. J., Basilevsky, A. T., Titov, D. V., Ignatiev, N. I., & Head, J. W. (2015). Active volcanism on Venus in the Ganiki Chasma rift zone. Geophysical Research Letters, 42(12), 4762–4769. https://doi.org/10.1002/2015GL064088
Showman, A. P., & Han, L. (2004). Numerical simulations of convection in Europa's ice shell: Implications for surface features. Journal of Geophysical Research: Planets, 109(E1). doi: 10.1029/2003JE002103
Singer, K. N., McKinnon, W. B., & Schenk, P. M. (2021). Pits, uplifts and small chaos features on Europa: Morphologic and morphometric evidence for

intrusive upwelling and lower limits to ice shell thickness. Icarus, 364, 114465. , doi: 10.1016/j.icarus.2021.114465
Smrekar, S. E., & Stofan, E. R. (1997). Corona Formation and Heat Loss on Venus by Coupled Upwelling and Delamination. Science, 277(5330), 1289–1294. https://doi.org/10.1126/science.277.5330.1289
Smrekar, S. E., Davaille, A., & Sotin, C. (2018). Venus Interior Structure and Dynamics. Space Science Reviews, 214(5), 88. https://doi.org/10.1007/s11214-018-0518-1
Solomon, S. C., Smrekar, S. E., Bindschadler, D. L., Grimm, R. E., Kaula, W. M., McGill, G. E., Phillips, R. J., Saunders, R. S., Schubert, G., Squyres, S. W., & Stofan, E. R. (1992). Venus tectonics: An overview of Magellan observations. Journal of Geophysical Research: Planets, 97(E8), 13199–13255. https://doi.org/10.1029/92JE01418
Sparks, W. B., Schmidt, B. E., McGrath, M. A., Hand, K. P., Spencer, J. R., Cracraft, M., & Deustua, S. E. (2017). Active Cryovolcanism on Europa? The Astrophysical Journal, 839(2), L18, doi: 10.3847/2041-8213/aa67f8
Spaun, N. A., Prockter, L. M., Pappalardo, R. T., Head, J. W., Collins, G. C., Antman, A., Greeley, R., & Galileo SSI Team. (1999). Spatial Distribution of Lenticulae and Chaos on Europa, Lunar and Planetary Science, XXX, 1847.
Squyres, S. W., Janes, D. M., Baer, G., Bindschadler, D. L., Schubert, G., Sharpton, V. L., & Stofan, E. R. (1992). The morphology and evolution of coronae on Venus. Journal of Geophysical Research: Planets, 97(E8), 13611–13634. https://doi.org/10.1029/92JE01213
Squyres, S. W., Janes, D. M., Schubert, G., Bindschadler, D. L., Moersch, J. E., Turcotte, D. L., & Stofan, E. R. (1993). The spatial distribution of coronae and related features on Venus. Geophysical Research Letters, 20(24), 2965–2968. https://doi.org/10.1029/93GL00866
Stefanick, M., & Jurdy, D. M. (1996). Venus coronae, craters, and chasmata. Journal of Geophysical Research: Planets, 101(E2), 4637–4643. https://doi.org/10.1029/95JE02709
Steinbrügge, G., Voigt, J. R. C., Wolfenbarger, N. S., Hamilton, C. W., Soderlund, K. M., Young, D. A., Blankenship, D. D., Vance, S. D., & Schroeder, D. M. (2020). Brine Migration and Impact-Induced Cryovolcanism on Europa. Geophysical Research Letters, 47(21), e2020GL090797. https://doi.org/10.1029/2020GL090797
Stephens, M. A. (1970). Use of the Kolmogorov–Smirnov, Cramer–Von Mises and related statistics without extensive tables. Journal of the Royal Statistical Society: Series B (Methodological), 32(1), 115–122, doi: 10.1111/j.2517-6161.1970.tb00821.x
Stofan, E. R., Bindschadler, D. L., Head, J. W., & Parmentier, E. M. (1991). Corona structures on Venus: Models of origin. Journal of Geophysical Research: Planets, 96(E4), 20933–20946. https://doi.org/10.1029/91JE02218
Stofan, E. R., Head, J. W., Campbell, D. B., Zisk, S. H., Bogomolov, A. F., Rzhiga, O. N., Basilevsky, A. T., & Armand, N. (1989). Geology of a rift zone on Venus: Beta Regio and Devana Chasma. GSA Bulletin, 101(1), 143–156. https://doi.org/10.1130/0016-7606(1989)101<0143:GOARZO>2.3.CO;2

Stofan, E. R., Sharpton, V. L., Schubert, G., Baer, G., Bindschadler, D. L., Janes, D. M., & Squyres, S. W. (1992). Global distribution and characteristics of coronae and related features on Venus: Implications for origin and relation to mantle processes. Journal of Geophysical Research: Planets, 97(E8), 13347–13378. https://doi.org/10.1029/92JE01314
Stofan, E. R., Sharpton, V. L., Schubert, G., Baer, G., Bindschadler, D. L., Janes, D. M., & Squyres, S. W. (1992). Global distribution and characteristics of coronae and related features on Venus: Implications for origin and relation to mantle processes. Journal of Geophysical Research: Planets, 97(E8), 13347–13378. https://doi.org/10.1029/92JE01314
Stofan, E. R., Smrekar, S. E., Tapper, S. W., Guest, J. E., & Grindrod, P. M. (2001). Preliminary analysis of an expanded corona database for Venus. Geophysical Research Letters, 28(22), 4267–4270. https://doi.org/10.1029/2001GL013307

Strom, R. G., Schaber, G. G., & Dawson, D. D. (1994). The global resurfacing of Venus. Journal of Geophysical Research: Planets, 99(E5), 10899–10926. https://doi.org/10.1029/94JE00388

Thomson, R. E., & Delaney, J. R. (2001). Evidence for a weakly stratified Europan ocean sustained by seafloor heat flux. Journal of Geophysical Research: Planets, 106(E6), 12355–12365. https://doi.org/10.1029/2000JE001332

USGS Astrogeology Science Center (n.d.), Categories (Themes) for Naming Features on Planets and Satellites, Planetary names. Available from: https://planetarynames.wr.usgs.gov/Page/Categories (Accessed 3 February 2025)

Watters, T. R. (1988). Wrinkle ridge assemblages on the terrestrial planets. Journal of Geophysical Research: Solid Earth, 93(B9), 10236–10254. https://doi.org/10.1029/JB093iB09p10236